MONITORING LARGE-SCALE ROCK SLOPES FOR THE DETECTION OF ROCKFALLS USING STRUCTURE-FROM-MOTION PHOTOGRAMMETRY AT DEBEQUE CANYON, COLORADO

by

Mohamed Elbahnasawy

A thesis submitted to the Faculty and the Board of Trustees of the Colorado School of Mines in partial fulfillment of the requirements for the degree of Master of Science (Geological Engineering).

Golden, Colorado

Date _____

Signed: _____

Mohamed Elbahnasawy

Signed: _____

Dr. Gabriel Walton

Thesis Advisor

Golden, Colorado

Date _____

Signed: _____

Dr. Wendy Bohrson

Professor and Department Head

Geology and Geological Engineering

ABSTRACT

This research investigates the frequent rockfall events in DeBeque Canyon along I-70. It uses the multi-epoch photogrammetric monitoring datasets collected by the Colorado Department of Transportation between 2014 and 2021. The study aims to assess the effectiveness of the direct geo-referencing approach in creating large-scale photogrammetric models without ground control points (GCPs). It also aims to develop a workflow for creating a regional-scale rockfall inventory and characterize the spatial variability of rockfall characteristics. Furthermore, the research seeks to evaluate the impact of pre-existing rockmass structures on rockfall frequencies, sizes, and shapes.

Comparison of the developed photogrammetric point clouds created using a direct geo-referencing approach to lidar surveys revealed a good matching precision. The precision was as good as 0.059 m in terms of root-mean-squared (RMS) difference metric. For efficient handling of large-scale, multi-epoch models, the study implemented construction of photogrammetric models for only the first and last acquisition. The corresponding image datasets for intermediate acquisitions were manually reviewed. This approach enabled rapid identification of the temporal occurrence of each rockfall. Segmenting photogrammetric models into smaller segments minimized "bowl-effect" distortion and reduced processing time.

The study revealed that rockfall activity vary along DeBeque Canyon corresponding to changes in lithologies, rockmass conditions, and the presence of oversteepened areas. Increased rockfall activity can be attributed to factors such as prevalence of weaker rockmasses, increased degree of fracturing, human interference, and presence of steeper slopes. The temporal rockfall rates increase in years with a higher number of days with snow thickness exceeding 1 inch. The study found that pre-existing rockmass structures influenced rockfall failure mechanisms, shapes, and scaling exponent of the power-law equation. The scaling exponents of the magnitude-cumulative-frequency (MCF) curves were found to be impacted mainly by variations in lithology and degree of fracturing. The expected range of block volumes obtained based on structural mapping was larger than the actual rockfall volumes. This discrepancy occurred due to model resolution limitations for structural mapping. It also resulted from the occurrence of smaller rockfalls due to intact rock failure between mapped joints and rockfalls not bounded by joint sets.

TABLE OF CONTENTS

LIST OF FIGURES

LIST OF TABLES

ACKNOWLEDGMENTS

I would like to express my heartfelt gratitude to my advisor, Dr. Gabriel Walton, for his consistent support and invaluable mentorship throughout the past two years, which greatly contributed to the completion of this thesis. I am deeply grateful to the U.S. Agency for International Development (USAID) and their Graduate Scholarships for Professionals (GSP) program for granting me the exceptional opportunity to pursue my studies at the Colorado School of Mines. Additionally, I would like to thank the Colorado Department of Transportation (CDOT) for providing the data that facilitated the exploration of my research questions.

I am sincerely appreciative to my friends and fellow students, whose encouragement, support, and fellowship have been crucial to this endeavor. I would like to give special thanks to Dr. Luke Weidner for his assistance during the course of my thesis work and to Dr. Isabella West for her dedicated efforts in reviewing my work. Lastly, I am forever grateful to my father, my wife, and my family for their unwavering belief in me and their endless love and support.

CHAPTER 1 INTRODUCTION

In recent decades, the world has experienced a rapid increase in population from 2.5 billion in 1950 to an estimated 8 billion in 2022 (United Nations' World Population Prospects, 2022). To accommodate this enormous growth, more people have moved and settled in remote mountainous areas (Porter & Orombelli, 1981). However, this proximity to mountainous areas has made transportation corridors and infrastructures such as highways, railways, bridges, and buildings vulnerable to the danger posed by rockfalls (Bunce et al., 1997; Brawner & Wyllie, 1976; Budetta & Santo, 1994). Rockfalls threaten human lives, cause delays in critical services, and disrupt travel. Therefore, conducting research on rockfalls is essential for understanding the characteristics and causes of this phenomenon, enabling the development of adequate mitigation measures to reduce the associated risk.

A *rockfall* is defined as a detached individual rock block or cluster of blocks that travel rapidly downslope by free fall, bouncing, or rolling (Varnes, 1978; Cruden & Varnes, 1996). Detachment occurs when a block loses contact with bedrock and releases or fails by sliding or toppling failure (Hantz et al., 2021). Small-scale rockfalls are the most frequent mass-wasting events in high-density urban areas, characterized by unpredictable occurrence and extremely high velocity of movement downslope (Hungr et al., 2005). Rockfalls can be triggered by many factors, such as volcanic eruptions, earthquakes, and meteorological factors such as precipitation and freeze-thaw cycles (Keefer, 1984; Hale et al., 2009; Allen & Huggel, 2013; Delonca et al., 2014).

The detailed investigation of rockfalls requires collecting detailed information on their rates, spatial distribution, and geomorphological characteristics. Various monitoring techniques have been employed for this purpose in the last few decades. The aim of this thesis is to highlight the importance of the photogrammetry Structure-from-Motion (SfM) technique in identifying and analyzing rockfalls in large-scale rock slopes. To achieve this objective, Unmanned Aerial Vehicles (UAVs) were employed to collect high-resolution aerial datasets of rockfall events, and an optimized workflow for processing these datasets was developed. Several algorithms were utilized for automated processing and analysis of the collected rockfall datasets. The resulting inventory and developed algorithms will enable enhanced study of rockfall characteristics and patterns on a large scale. It will also contribute to understanding the geological contribution to

rockfall occurrences. Furthermore, the developed workflow in this thesis will contribute to improved ease of application of SfM in rockfall detection.

SfM is an effective technique for constructing three-dimensional (3D) models from two-dimensional (2D) images. Capturing images for the target scene from various viewpoints enables algorithms to calculate the 3D positions of the features detected in the images. SfM is cost-effective and has the advantage of covering large-scale outcrops efficiently, producing high-resolution models comparable in accuracy to lidar. Moreover, the availability of numerous software packages, such as Metashape and Pix4d, which automate most of the SfM process make it an accessible approach for handling large datasets. Thanks to its wide range of applications, high precision, and affordability, SfM has become a widely accepted tool in geoscience.

The application of UAVs has become increasingly common for studying rockfall hazards, particularly in areas with high, inaccessible, and steep slopes. In these locations, conducting traditional field surveys and mapping can be hazardous (Wang et al., 2022; Nesbit et al., 2022). The ability of UAVs to fly at different elevations and imaging ranges provides several advantages over terrestrial photogrammetry. These include capturing different perspectives of the scene and reducing occlusion of objects. The cost-effectiveness, increased safety, and ease of application of UAVs allow for repeated surveying of large-scale, steep slopes to be conducted over short periods.

The thesis focuses on rockfalls that regularly occur at the rock slopes of DeBeque Canyon along Interstate Highway 70 (I-70) in western Colorado, USA. The I-70 highway is a critical transportation route connecting Grand Junction's urban areas to the Denver area (Figure 1.1). Due to the high traffic volumes and high speeds on the road, cars in this area are vulnerable to rockfalls, which can result in injuries and fatalities. In response, the Colorado Department of Transportation (CDOT) has conducted a multi-epoch photogrammetric monitoring campaign to cover the area of DeBeque Canyon using UAVs. The monitoring campaign was carried out from 2014 to 2021, aiming to develop a rockfall database to understand the rockfall behaviors, processes, and frequencies along the Canyon. A large-scale rockfall inventory developed from long-term monitoring datasets is essential for understanding the spatial variability of rockfall characteristics. It also helps in understanding how slopes deteriorate over time along this critical

highway section. This information is crucial for evaluating the expected rockfall volumes and developing mitigation measures.

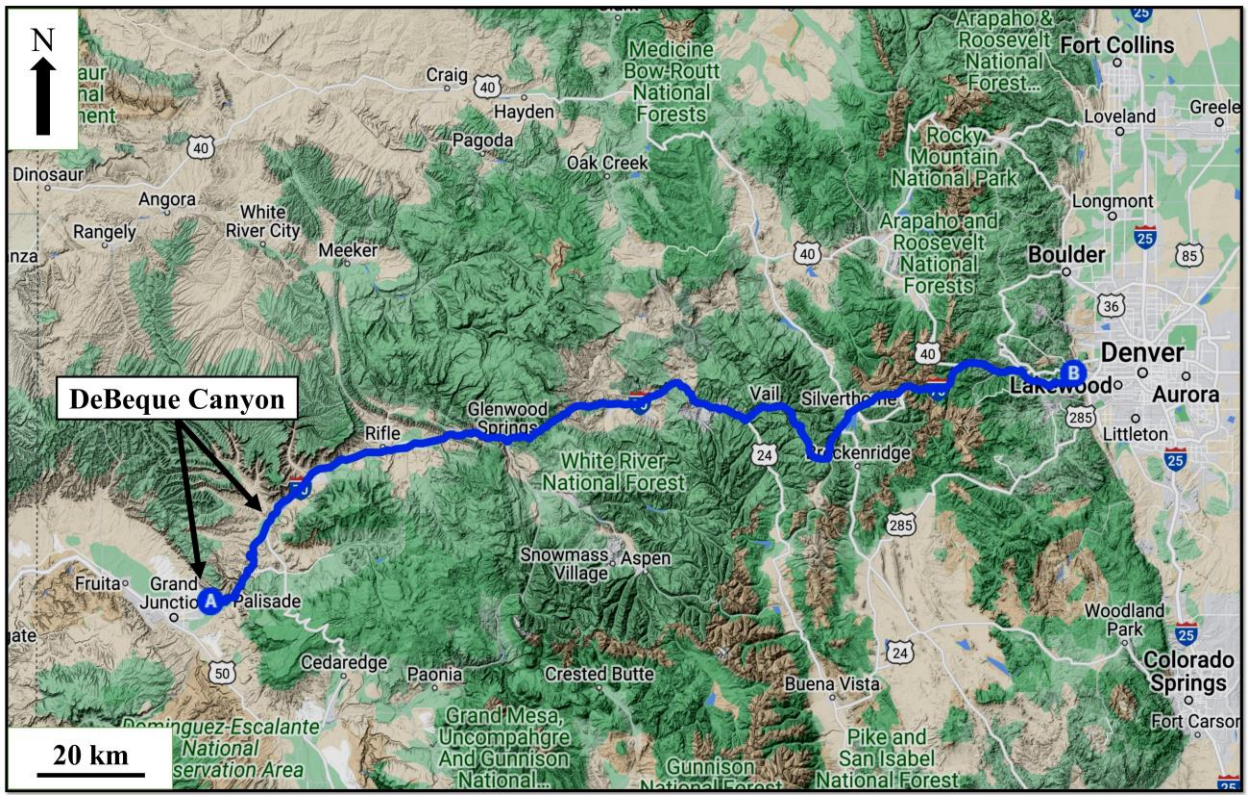

Figure 1.1 Location map for the I-70 Highway section from Grand Junction to the Denver metropolitan area showing the study site at DeBeque Canyon.

1.1 Structure from Motion Photogrammetry

Photogrammetry is a remote sensing technology capable of building a 3D model of an object by processing photographs taken of the object at different angles and ranges (Schenk, 2005). The perception of human eyes for depths depends on binocular vision, where each eye captures a separate image for an object. The brain then converges these images into a single 3D view. Based on that, the stereoscope device was used to create a depth illusion for eyes by presenting two different images to each eye separately. This gives each eye (left and right) a different view of the same object in two images, within overlapping portions, creating a 3D effect with a sense of depth. This analog photogrammetry was applied for decades to gather information from pairs of overlapping vertical aerial photos. Several measurements were obtained from the 3D view,

including distances, elevations, and scales. However, this manual method becomes more time-consuming when applied to larger scales and more images.

In the 1980s, digital photogrammetry was introduced. With digital photogrammetry, measurements can be made on many images quickly and with less effort. This advancement allowed for Digital Elevation Models (DEMs) to be produced for the imaged surfaces based on the calculated elevations. However, manual input was still needed for the image location, camera orientation, and manual registration of image pixels using Ground Control Points (GCPs) before establishing any measurements.

As technology progressed, digital photogrammetry took advantage of increased computer power and the development of sophisticated algorithms leading to the emergence of Structure-from-Motion (SfM) photogrammetry. SfM detects the camera position and orientation without needing GCPs of known coordinates (Westoby et al., 2012). The general process of SfM (Figure 1.2), typically starts with detecting and matching features in multiple images and obtaining camera positions. Subsequent steps involve generating a tie point cloud, geo-referencing, building densified point clouds, and mesh generation. (Westoby et al., 2012; Rodgers et al., 2022). This technique enables more automated acquisition of 3D data than traditional photogrammetry techniques.

SfM depends on computer vision techniques to build 3D models from digital images. The SfM process begins by identifying distinctive features in each photo, such as points or lines, and matching these features between all images (Snavely et al., 2008). The match is determined by comparing the surrounding elements around that feature in all images until finding enough correspondence. These correspondences are then used to calculate the camera positions and orientations by solving the relative positions of the camera (Hartley & Zisserman, 2003). Adding more images to the process will improve the matching and accuracy of camera positions and orientations. Once camera positions and orientations are obtained, the tie point cloud can be created, which represents the primary 3D model of the scene. Finally, the Multi-view Stereo algorithm (MVS) is employed to densify the tie point clouds producing a more detailed point cloud or 3D mesh (Rose et al., 2015).

The SfM workflow consists of a set of progressively developed algorithms, as no single algorithm can do all these steps alone (Furukawa & Hernández, 2015). The detection and

extraction of distinctive features in images are accomplished using the Scale-Invariant Feature Transform (SIFT) algorithm introduced by Lowe (2004). SIFT is the most popular and applied algorithm for object recognition and description (Nguyen et al., 2014). The SIFT algorithm identifies characteristic key points, under variable scales, rotation, distortion, and illumination conditions (Lowe, 2004).

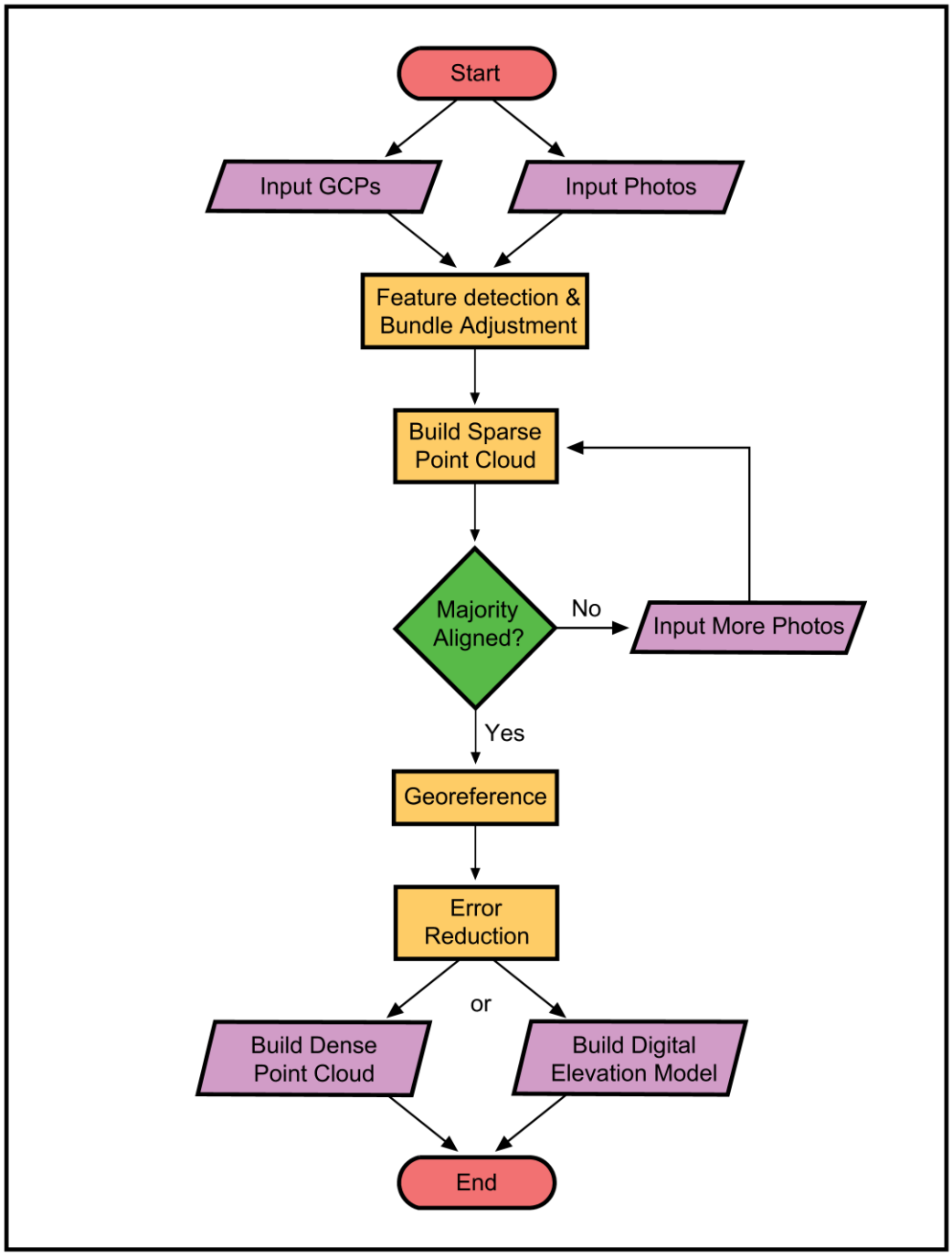

Figure 1.2 The general SfM workflow, adapted from Rodgers et al. (2022).

Once the key points in the images are detected and described, the feature descriptor vectors are compared to find the best match across images. This comparison and matching step can be performed using the approximate nearest neighbor matching algorithm (Arya et al., 1998; Brown & Lowe, 2005). The detected correspondences from this step provide an initial estimation for the camera position and orientation. This estimation is refined through iterative non-linear least-squares optimization algorithms to obtain more accurate camera poses (Westoby et al., 2012). The precision of the camera pose estimation directly affects the accuracy of the subsequent reconstruction of the 3D scene.

After identifying correspondences and camera pose, the 3D reconstruction of the scene can be accomplished. This process can be broken down into two main steps: triangulation and bundle adjustment. In the initial triangulation step, the 3D positions of the key points are calculated, and the initial 3D model is constructed (Wöhler, 2012). The bundle adjustment step follows, where the initial 3D positions are refined by iterative adjustments to reduce the reprojection error of the 3D points in the image plane (Zhang et al., 2006). The optimal outcome of the bundle adjustment is a tie/sparse point cloud (Figure 1.3B) that represents the fine-tuned 3D positions of the key points (Westoby et al., 2012).

After bundle adjustment, the MVS algorithm produces a densified point cloud for the 3D scene (Seitz et al., 2006). This generates depth maps for the images, with each pixel displaying a depth value relative to the distance from the camera (Fuhrmann et al., 2014). After filtering and removing outliers from the depth maps, they are used to generate high-quality 3D meshes, digital terrain models, and dense point clouds, as shown in Figure 1.3C (Vollgger et al., 2016).

The resulting SfM model is referenced to an arbitrary or local coordinate system without real-world scale. Therefore, geo-referencing brings the 3D model into a standard coordinate system, typically using GCPs. These markers can be identified in the photos, and their coordinates can be measured using surveying tools to provide real-world scale and orientation for the model (Sanz-Ablanedo et al., 2018). The accuracy of the resulting 3D models typically increases when an increased number of GCPs is used (Harwin et al., 2015; Eltner & Schneider, 2015; Hugenholtz et al., 2016; Agüera-Vega et al., 2017).

GCPs should be placed at the edges of the surveyed scene and distributed evenly across the entire area to achieve optimal geo-referencing. However, distributing GCPs along slopes can be

time-consuming, labor-intensive, and pose a high risk, especially in steep rock slopes. Therefore, a direct geo-referencing approach can be used, in which the coordinates of the camera recorded during photo-taking are used directly (Sanz-Ablanedo et al., 2018). This approach saves the effort and cost associated with installing and processing GCPs, reducing the processing time.

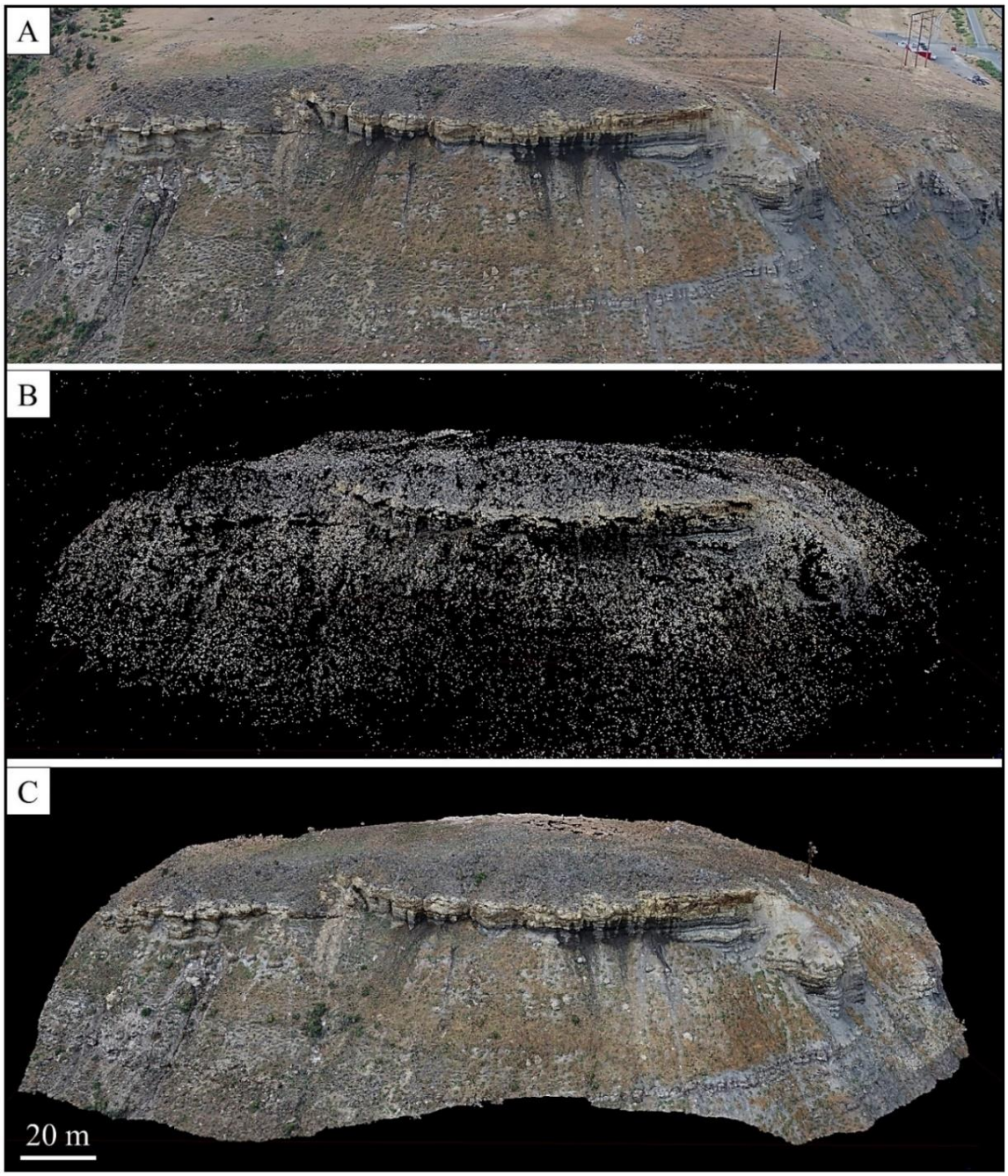

Figure 1.3 Example of the SfM process results for a rock slope in DeBeque Canyon along I-70. A) Photograph of the natural scene, B) The tie point cloud, and C) The final densified point cloud.

1.2 Literature Review and Research Needs

This section will present a literature review on the application of Structure from Motion in geoscience and the areas that require further research. Additionally, it will provide a literature review on the structural controls on rockfalls and the utilized methods for assessment.

1.2.1 Geoscience Applications of Structure from Motion

While the basic concept of SfM dates back to 1979, publications on its application in geosciences emerged in 2010 (Abellan et al., 2016). SfM has become increasingly valuable to geoscientists due to its capability to produce high-resolution and precise digital elevation models (DEMs). These models enable them to study changes in topographic and geological features with a higher level of accuracy (James & Robson, 2012; Fonstad et al., 2013). The availability of software capable of automating the SfM processes motivated researchers to collect and work on larger quantities of data and analyze earth processes over a more extended period (Nadal-Romero et al., 2015; Eltner et al., 2016). Furthermore, SfM can also be combined with other 3D data acquisition techniques, such as Terrestrial Laser Scanning (TLS) and Infrared Thermography to produce even more precise datasets (Warrick et al., 2019; Lim et al., 2005; Mineo et al., 2022).

Given the many strengths of SfM, it has been used in various areas of geoscience to investigate a wide range of research questions. For instance, SfM has been implemented to map erosion and sediment transportation (d'Oleire-Oltmanns et al., 2012; Pikelj et al., 2015), study volcanic areas (Kolzenburg et al., 2016), monitor glacial processes (Piermattei et al., 2016; Ryan et al., 2015), and track groundwater flow (Ikkala et al., 2022). It has also been applied to assess landslide movements (Peppa et al., 2019; Warrick et al., 2019), analyze rockmass behavior (Mineo et al., 2022), and monitor coastal erosion (James & Robson, 2012; Westoby et al., 2020).

Monitoring rock slopes for rockfall detection requires high-resolution databases that enable the detection of minor rockfalls (Dorren, 2003). Recent advances in data acquisition and monitoring techniques have enabled the collection of high spatial and temporal resolution datasets (Rosser & Massey, 2022). These techniques include ground-based interferometric synthetic-aperture radar (GB-InSAR) (e.g. Zhang et al., 2018), real-aperture radar (RAR) (e.g. Werner et al., 2008), Satellite InSAR (e.g. Rott et al., 2002), lidar (e.g. Weidner & Walton,

2021), robotic total station (e.g. Glueer et al., 2021), UAV-photogrammetry (e.g. Sarro et al., 2018; Graber & Santi, 2022a), and thermal imaging (e.g. Teza et al., 2015).

SfM-photogrammetry is effective for monitoring rock slopes and detecting rockfalls (Van Veen et al., 2017; Gigli et al., 2022). There has been a noticeable increase in published research using SfM-photogrammetry in slope monitoring in recent years (Guerin et al., 2020; Giacomini et al., 2020; Rossi et al., 2021). UAV-SfM photogrammetry relies on remote data acquisition, where the data collection is conducted using high-resolution cameras mounted on UAVs. SfM offers faster deployment, relatively lower cost, and better color representation compared to other techniques such as aerial and terrestrial laser scanning (Table 1.1). It can also monitor changes over large-scale areas with a high spatial resolution, similar to laser scanning (Lato et al., 2015).

The application of UAVs in rockfall investigation has been widely accepted for different aspects of the rockfall hazards assessment (Sarro et al., 2018; Saroglou et al., 2018). UAVs have been used to build 3D models for evaluating rockfall risk during emergencies (Giordan et al., 2015). This approach can be applied to study rockfall trajectories by capturing images of slopes from different altitudes. It helps in obtaining high-resolution topographic surveys and identifying rockfall source areas (Saroglou et al., 2018).

Change detection on point clouds from different epochs can help to identify the spatial and temporal occurrences of rockfalls and quantify their frequencies, sizes, and shapes. The precision of change detection for rockfall was improved by the development of the Multi-Scale Model-to-Model Cloud Comparison (M3C2) algorithm by Lague et al. (2013). The M3C2 algorithm has proven effective in identifying changes across complex terrains. The M3C2 algorithm was first applied for change detection along slopes by Stumpf et al. (2015). They endorsed its accuracy for change detection applications and volume estimation. It is currently the most widely applied approach for rockfall change detection (DiFrancesco et al., 2020; Weidner & Walton, 2021; Schovanec et al., 2021).

Table 1.1 Comparison between Photogrammetry and Aerial/Terrestrial laser scanning (ALS/TLS), adapted from Lato et al. (2015), with lower numbers indicating better performance. Highlighted cells indicate where photogrammetry performed better than or comparably to laser scanning.

Task	TLS	Photogrammetry	ALS
Remote site accessibility	3	2	1
Speed of deployment	2	1	2
Ability to map small-scale discrete changes	1	2	3
Ability to map large-scale discrete changes	1	1	1
Ease of data collection	1	2	3
Spatial resolution	1	1	2
Map small-scale discontinuity features	1	2	3
Map large-scale discontinuity features	1	1	1
Full-color 3D data	2	1	3
Georeferenced spatial accuracy	1	2	3
Individual point accuracy	1	2	3
Portability of equipment	2	1	3
Affordability (small spatial footprint)	2	1	3
Map vertical topographic features	1	1	2
Map horizontal topographic features	2	2	1

Owing to the great potential of SfM in slope monitoring applications, researchers have been working to provide practical workflows for the efficient employment of SfM. These workflows include the acquisition and processing of photo datasets and the 3D scene reconstruction through the detection of rockfall locations and volume calculation (Westoby et al., 2012; Kromer et al., 2019; Graber & Santi, 2022a). However, most of these workflows were designed for small-scale datasets and require further development and adjustments to enable their implementation on large-scale slopes.

The application of direct geo-referencing in photogrammetry has been introduced before. Efforts have been made to enhance its accuracy compared to using GCPs for traditional geo-referencing. One of the earliest attempts to apply direct geo-referencing in UAV photogrammetry was conducted by Gabrlik (2015). However, the accuracy was unsatisfactory due to inaccuracies in camera parameter calculations. These inaccuracies caused errors of several tens of centimeters horizontally and even larger errors vertically. Rabah et al. (2018) achieved

increased horizontal and vertical accuracy (by 0.034 m and 0.029 m, respectively) by using an RTK-GNSS receiver onboard the UAV for positioning the collected images.

Peppa et al. (2019) proposed a geo-referencing technique that eliminates the use of GCPs in multi-epoch datasets. They searched for fixed and stable features "pseudo-GCPs" between photos, which can be used as GCPs in geo-referencing the 3D model, given the overall stability of the site. Kromer et al. (2019) provided a SfM workflow for model development and change detection that does not require GCPs. They found that similar accuracy could be obtained if the internal camera parameters were fixed over time (when using a fixed camera system). Recently, different approaches were developed for utilizing direct geo-referencing in photogrammetry. These approaches depend on the recorded data from the GPS/GNSS receivers installed on the UAVs and the subsequent processing steps. Teppati et al. (2020) compared five different approaches for recording coordinates using GPS/GNSS and concluded that direct geo-referencing could obtain an accuracy of a few centimeters without using GCPs. Nesbit et al. (2022) found that the precision of photogrammetric models using direct geo-referencing increases by using different imaging angles. The obtained precision is similar to models utilizing GCPs.

SfM-photogrammetry has been utilized to monitor rock slopes and characterize rockfalls across various spatial scales and over variable time periods. The applications of SfM in small-scale rock slopes aim to quantify rockfall occurrences, study rockfall dynamics, evaluate rockfall hazards, and map rockmass discontinuities (Giacomini et al., 2020; Papathanassiou et al., 2020; Hayakawa & Obanawa, 2020; Gómez-Gutiérrez & Gonçalves, 2020; Gallo et al., 2021; Graber & Santi, 2022a). Most of the existing research on rockfall is focused on monitoring small-scale slopes. However, in many cases it is necessary to investigate rockfall occurrences over long distances such as highways and coastal cliffs.

Giacomini et al. (2020) utilized a system of two digital cameras to monitor a 70 m long, highly fractured, open pit slope in Australia for seven weeks. The study detected many rockfalls (up to 650 events) and small volumes (up to 10^{-4} m^3) with stable Magnitude-Cumulative-Frequency (MCF) relationships. The results helped to characterize rockfalls and evaluate the climatic and geological impact with high accuracy and precision. Graber & Santi (2022a) applied the UAV-SfM to study four small-scale, natural rock slopes ranging in area from approximately

4,500 m^2 to 17,000 m^2. The four slopes were imaged at approximately one-month intervals to detect changes resulting from rockfalls over one year of monitoring. Although there were few detected rockfalls, the photogrammetry for these small sections enabled the study of the rockfall frequencies and the detection of the triggering factors for rockfalls at the study sites.

Most large-scale photogrammetric studies are conducted for monitoring cliff erosion (Baily & Nowell, 1996; Costa et al., 2004; Moore & Griggs, 2002; Westoby et al., 2012). For example, Westoby et al. (2012) utilized MVS-SfM to monitor erosion rates along a one km coastal cliff. They used a 14.7 Megabyte digital camera from a distance range of 25-30 m. The study demonstrated the capability of the low-cost MVS-SfM monitoring technique to investigate cliff erosion and identify rockfall volumes as small as 7.0×10^{-2} m^3.

Other studies on regional-scale rock slope monitoring have been conducted using TLS. These studies have investigated the relationship between rockfall occurrences and slope angles. They have also studied the long-term behavior of rock slopes, identified potential rockfall sources, and observed changes in rockfall frequencies over time (Loye et al., 2009; Benjamin et al., 2020; Rossi et al., 2021). Benjamin et al. (2020) found that the magnitude-frequency relationship of rockfall occurrences depends on the scale of the monitored section. The study recommended monitoring a total of 2.5 km for large-scale slopes; although this length recommendation is likely not universal and may depend on site-specific factors, it is used as a basic benchmark for this study. This would help obtain a reliable estimate of the relative occurrence of large and small rockfall volumes.

Although numerous studies have investigated slope behavior over time, most of them were conducted on a local scale, and a few considered the regional scale context. Furthermore, existing processing techniques for regional-scale datasets require optimization to achieve better accuracy and efficiency when applied on a large scale.

1.2.2 Structural Controls of Rockfall

Many factors affect the initiation of rockfalls, including slope geometry, intact rock strength, weathering conditions, and prevailing rockmass structures. The resulting rockfalls can be differentiated into structure-driven rockfalls, associated with planar, wedge, or toppling failure, and non-structure-driven rockfalls, formed by weathering and raveling (Vandewater et al., 2005). In addition to other factors, pre-existing rockmass structures can play an important role in

determining slope susceptibility to rockfall. Structure characteristics such as orientation, spacing, roughness, and persistence can control the failure mechanism, frequency, size, and shape of resulting rockfalls.

Vandewater et al. (2005) suggested that variations in lithology and the number of joint sets are the main factors determining the type and size of resulting rockfalls. Their study indicates that increasing lithological variation has the potential to create large, non-structure driven rockfalls. Additionally, the existence of more than two sets of discontinuities creates structurally controlled rockfalls with varying sizes, depending on the spacing of the discontinuities. Slopes with a lower degree of lithological variation and more than two joint sets with spacing larger than 1 m are likely to produce large structurally controlled rockfalls.

Intact rock strength also plays an important role in determining the shapes and sizes of rockfalls through rock bridges. Rock bridges can add stability to rock blocks by holding them in place along weak surfaces. On the other side, gradual weathering of rock bridges over time might increase the risk of rockfalls by introducing weakened surfaces to the rockmass that can lead to intact rock failures. Evaluation of the impact of rock bridges on rockfalls has been conducted mostly on single cases of large rockfalls rather than large-scale datasets of large number of rockfalls (Paronuzzi and Serafini, 2009; Sturzenegger and Stead, 2012). Fewer studies have considered the large-scale context (de Vilder et al., 2017).

The structural controls of rockfall can be evaluated through field investigation, kinematic analysis, numerical modeling, rockfall simulation, and structural mapping from remote sensing surveys. The most practical discontinuity survey methods of rock exposures are scanline (Priest & Hudson, 1976), circular (Mauldon et al., 2001; Sturzenegger et al., 2011), and window mapping (Sturzenegger & Stead, 2009). Structure mapping of rock surfaces using the 3D models acquired from photogrammetry and TLS has been extensively investigated (Haneberg, 2008; Lato et al., 2009; Sturzenegger & Stead, 2009; Ferrero & Umili, 2011; Lambert et al., 2012). The accuracy of derived fracture networks and representative fracture characteristics relies heavily on the resolution of the 3D models (Sturzenegger et al., 2011).

Numerical modeling has increasing importance in incorporating rockmass structures and modeling rockfall failures. Both continuum and discontinuum models have been applied to simulate the behavior of rockmass structures and evaluate the impact of structures on the

rockmass stability (Stead & Coggan, 2012; Török et al., 2018). Discrete fracture networks (DFN) are increasingly applied in the simulation of rockmass fractures and to obtaining rockfall block shapes, sizes, and frequencies (Sturzenegger et al., 2011; Lambert et al., 2012). Lambert et al. (2012) conducted detailed window structure mapping on 3D photogrammetry models to assess the rockfall hazards using 3D discrete fracture network modeling (DFN). A statistical distribution of rockfall volumes was obtained using Monte Carlo simulation based on the mapped joint sets. The resulting size distribution was compared to observations from images to generate the best representative size distribution.

1.3 Research Objectives

To address the knowledge gaps identified in the literature review, the proposed thesis aims to investigate the following research objectives and related questions:

Objective 1**:** Implement a workflow for creating 3D photogrammetric models for regional-scale datasets and evaluate the accuracy of the direct geo-referencing on the scale of the models.

- How effective is the direct geo-referencing method for creating large-scale (i.e., regional) photogrammetric models without GCPs?

The accuracy of using the direct geo-referencing method is evaluated by comparing photogrammetric dense clouds to reference models obtained from lidar surveys. The statistical distribution of differences between the two models is used to assess the accuracy of the models and provide a quantitative measurement of their similarity. The findings of this comparison will help in identifying the potential of this method for producing reliable photogrammetric models. Additionally, it will aid in recognizing the enhancements needed to improve the model's accuracy.

- How can the time of occurrence of each rockfall through the multi-epoch acquisitions be identified without having to build several models?

Building photogrammetric models for multi-epoch acquisitions on a large scale requires extensive time and effort. Therefore, the current research focuses on building photogrammetric models for the first and last acquisitions. The identification of rockfall events in the intermediate

acquisitions is made by manually reviewing the image datasets. The accuracy and limitations of this approach are assessed by evaluating the frequencies and sizes of the detected rockfalls.

Objective 2**:** Create a regional scale rockfall inventory and characterize the spatial variability of rockfall characteristics along DeBeque Canyon.

- How do rockfall rates, magnitudes, frequencies, and shapes vary along the Canyon?

The obtained rockfall data are utilized to characterize the rockfall occurrences along the Canyon. Several comparisons are conducted between the studied sites to demonstrate the spatial variability of rockfalls across the Canyon. The rockfall rates, magnitudes, and frequencies in addition to volumes and shapes are compared to evaluate the differences within and between the study sites.

- What are the expected reasons for similarities/differences in rockfall characteristics between the studied sites?

The variability of rockfall characteristics along the Canyon is analyzed and compared to changes in geology, rockmass condition, slope aspect, and human activity. Geology varies across the Canyon, which can affect the sizes and shapes of rockfalls. Other factors, such as the variations in the slope angles and the presence of excavated and steep slopes are also assessed. The spatial variability of rockfall activities is compared to these factors to demonstrate which factor(s) may have the highest impact on rockfall occurrences across the Canyon.

Objective 3**:** Evaluate the structural impact on the rockfall occurrences in terms of intensity, sizes, and shapes.

- How do the pre-existing rockmass structures influence the rockfall mechanism(s) at each site?

Slope-scale mapping is conducted on the photogrammetric models to identify the orientation, persistence, and spacing of the joint sets at every site. These data are utilized to determine the failure mechanisms of the rockfall. The measured spacings of the joints are utilized to obtain the expected range of block volumes using Monte Carlo simulation. This range is then compared to the actual rockfall volumes obtained from photogrammetry.

CHAPTER 2 STUDY SITES

DeBeque Canyon is situated in Mesa County in western Colorado, USA. The Canyon has been shaped by the natural process of erosion of the Colorado River over several thousands of years. The Canyon cliffs consist of sandstone and shale that are susceptible to weathering and erosion, leading to rock instabilities and rockfall formation (Figure 2.1). The frequent rockfall events have a notable impact on the traffic along I-70 that runs parallel to the Colorado River. A photogrammetry monitoring campaign was conducted that covered the entire 22 miles (35.4 km) of the Canyon. Specific sites were chosen for this study based on the collected data, which were distributed along the entire length of the Canyon. This chapter provides an overview of the geology and topography of the Canyon and the selected study sites. It also describes the data collection conducted by CDOT.

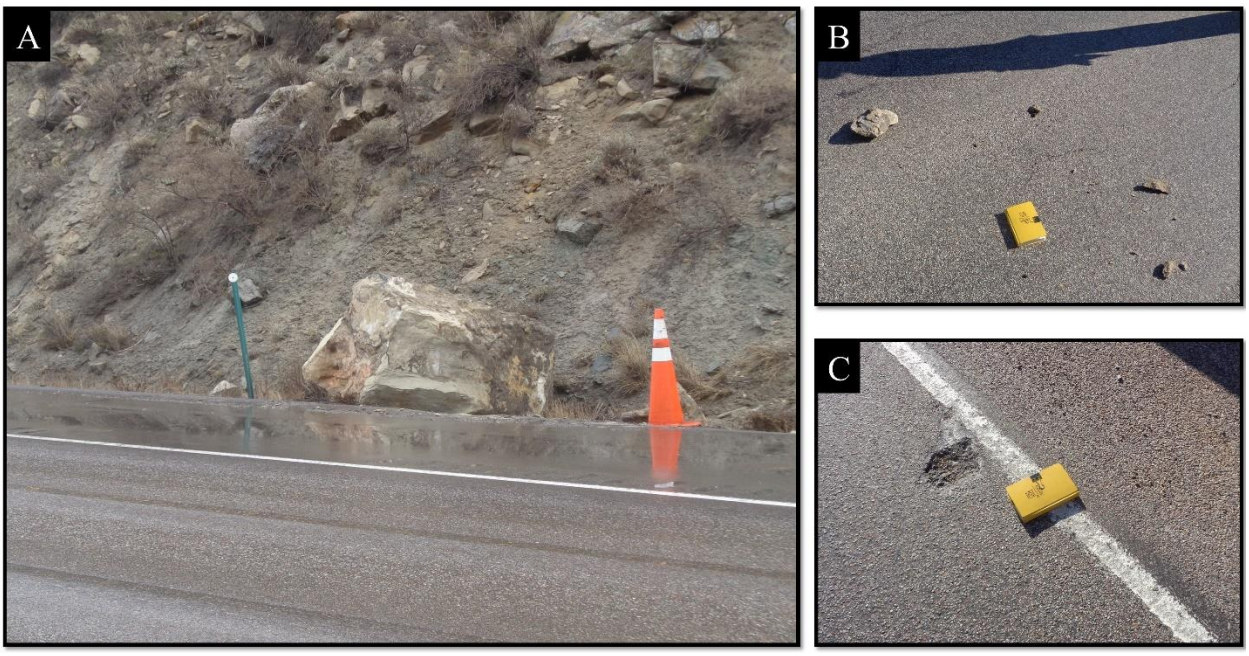

Figure 2.1 Examples of rockfalls at DeBeque Canyon. A) A large sandstone block detached from the top of the slope and fell into the ditch. B) Small rock fragments scattered on the road. C) Damage to the road from rockfalls. Photos courtesy CDOT.

2.1 DeBeque Canyon

DeBeque Canyon is located within the Colorado Plateau, southwest of the Piceance Creek Basin, and occupied by the sedimentary rocks of the Mesa Verde group (Erdmann, 1934). The exposed sedimentary rocks at the surface consist primarily of sandstone alternating with softer

shale, siltstone, and coal beds. The alternating, gently dipping sedimentary rocks form a topographic feature known as a Cuesta (Figure 2.2). This landform is characterized by a cliff face (the Book cliff) on one side and a long, gently dipping slope capped by hard rocks on the other side. The vegetation in the area includes sagebrush, greasewood, and Russian thistle.

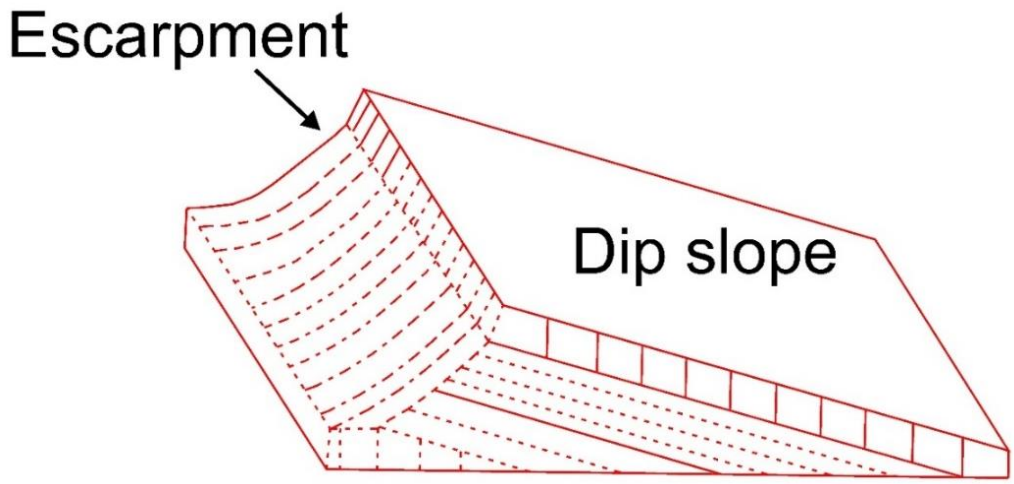

Figure 2.2 Diagram showing the Cuesta landform with a front steep slope or escarpment and gentle back dip slope, adapted from Radoane et al. (2020).

The study site is dominated by three sedimentary formations (Figure 2.3) of the Mesa Verde group of Late Cretaceous age: The lower Sego sandstone FM, overlain by the Mount Garfield FM and capped by the Hunter Canyon FM along most of the Canyon (Donnell, 1961; Cashion, 1973; Ellis & Gabaldo, 1989). The Sego Sandstone FM varies from massive to thinly bedded marine sandstone with variable thickness and exists at the base of southern slopes. The Mount Garfield FM occupies the southern section of the Canyon and consists of sandstone, shale, sandy shale, shaly sandstone, carboniferous shale, and coal beds. Most of the Canyon is covered by the Hunter Canyon FM, consisting mainly of massive, medium to coarse-grained sandstone, interbedded with gray shale and clay shale beds. The Hunter Canyon FM forms medium to high cliffs, varying from 375 to 1400 feet (Cashion, 1973). The site is part of a monocline fold that dips 6º to 27º towards the northeast, and the exposed rocks are mostly jointed and affected by several minor faults.

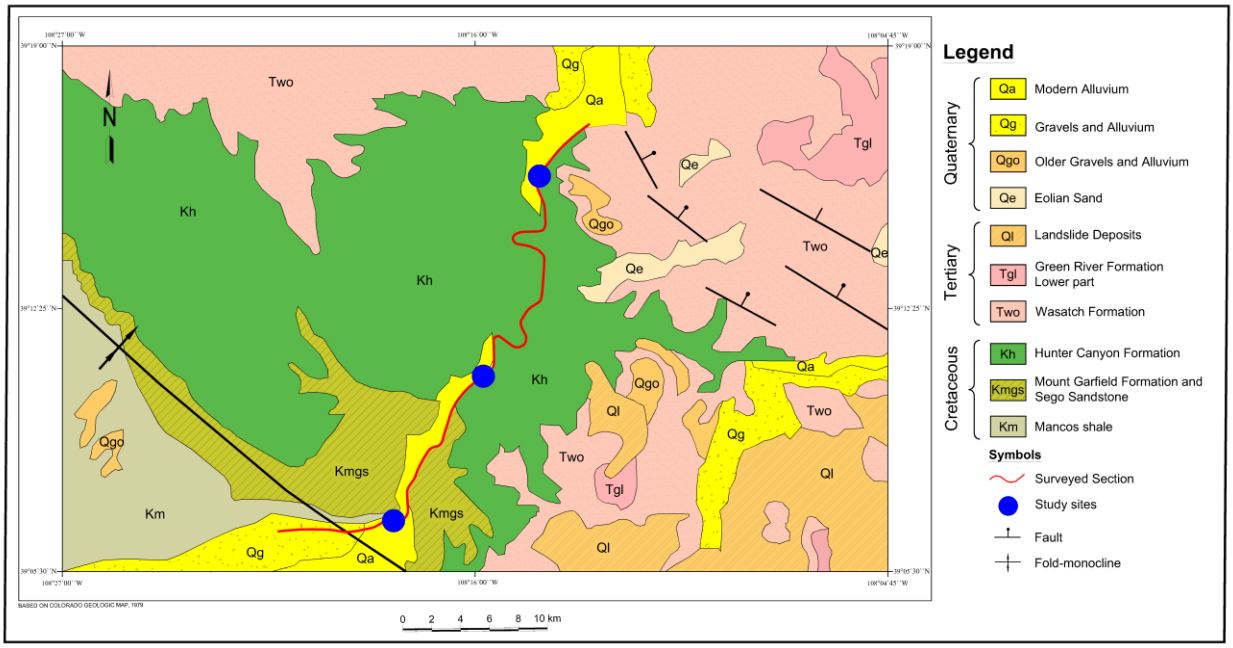

Figure 2.3 Geologic map of the area of DeBeque Canyon, modified after the Geologic Map of Colorado (Tweto, 1979).

2.2 Image Data Collection

The large extent of the monitored section and the presence of high, steep slopes in the Canyon required CDOT to use drone-based photo collection. This allowed them to capture images along the steep slopes for rock slope monitoring. The drones were utilized to capture high-resolution photographs with a high percentage of overlap between successive photos at different elevations. The increase in UAVs survey paths at different heights improves the density of photogrammetric models and the accuracy of the collected data while reducing occlusion. An example of the conducted photogrammetry at the Canyon is shown in Figure 2.4 with several survey paths at different elevations.

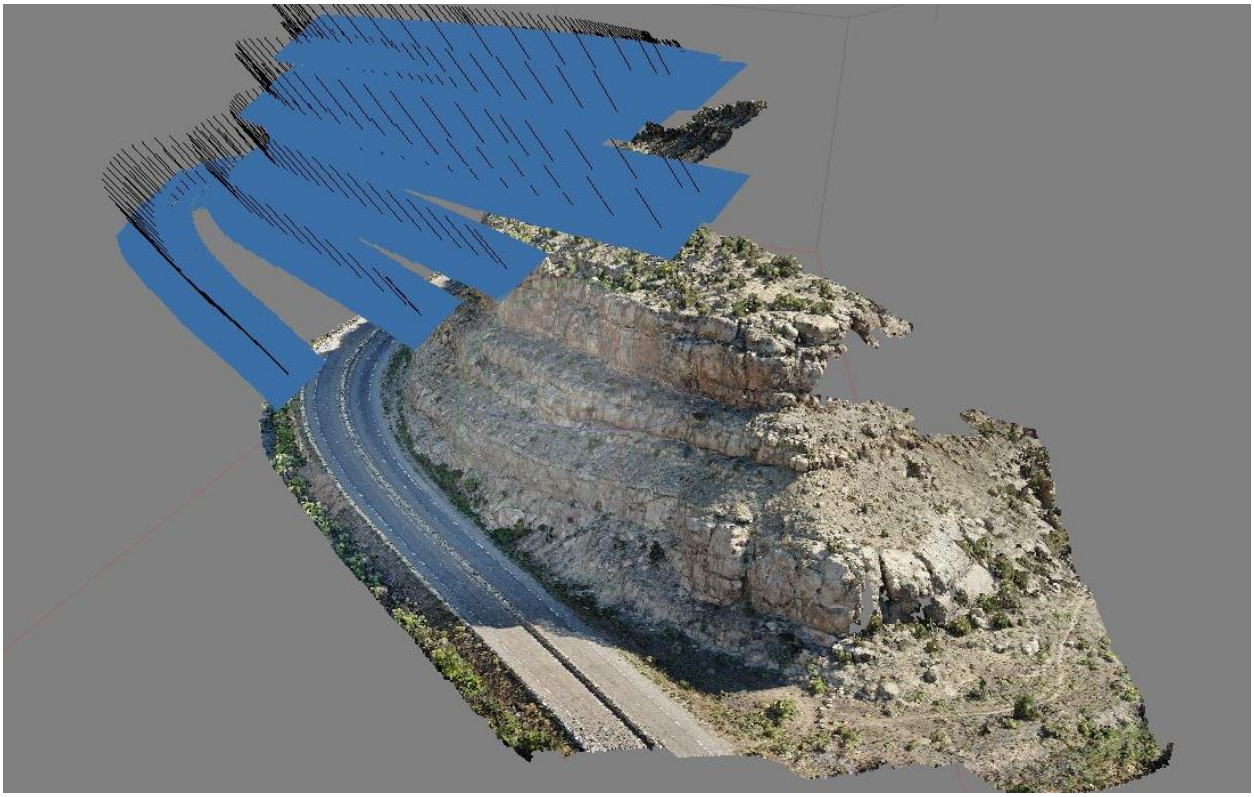

Figure 2.4 Example of the conducted UAV photogrammetry at DeBeque Canyon. Blue rectangles indicate photograph locations along the flight paths, while the black lines indicate the imaging direction.

Organizing the photogrammetric datasets provided by CDOT was a challenging task. After thorough inspection, it was found that 41 sites along I-70, from the mile point (MP) 036 to MP 058_10, were surveyed. The first three acquisitions were conducted from 2014 to 2016 and covered all the sites. However, the subsequent acquisitions were focused only on areas susceptible to rockfall hazards or were conducted in response to specific rockfall incidents. Therefore, the number of acquisitions varies across the different sites. For example, the MP 036_00 site was only surveyed in the first three acquisitions, and no further surveys were conducted after 2016. On the other hand, the MP 048_85 site was surveyed in five acquisitions from 2014 to 2021.

Preliminary data evaluation aimed to assess the coverage extent for each site and identify representative sites with the highest number of acquisitions along the Canyon. The selected sites are located at MP 042_80, MP 048_85, and MP 056_50, representing the southern, middle, and northern sections of the Canyon, respectively (Figure 2.5). The selection of these sites also

considered the variation in geology to assess the impact of lithology on the rockfall occurrences. The sites differ in topography and extent, where the southernmost site is 575 m long and 163 m high and the northernmost site is 1,220 m long and 79 m high. The pre-existing rockmass structures also vary within and between the study sites. These variations motivated the selection of these representative sites for investigating the variability of rockfall activity throughout the Canyon.

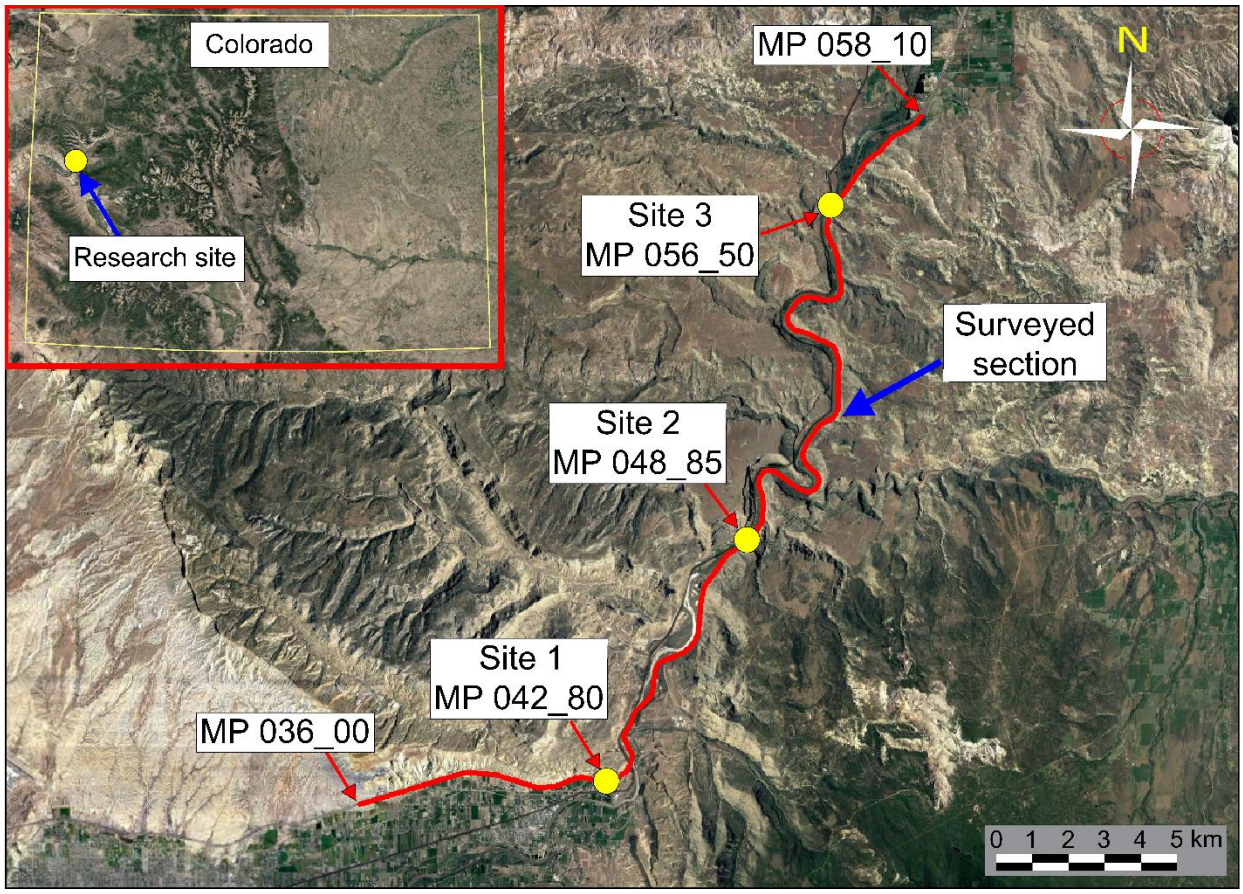

Figure 2.5 Location map for the DeBeque Canyon study area and the selected three sites.

Figure 2.6 summarizes the conducted photogrammetric data acquisitions at the three sites. The initial three acquisitions took place in 2014, 2015, and 2016, covering all three sites. Site 1 was monitored for 74 months through five acquisitions. The time intervals between acquisitions varied, and the longest gap was 39 months, between the fourth and last acquisition. Site 2 was monitored for 79 months, through five acquisitions. The largest gap between acquisitions was 34 months. At Site 3, monitoring spanned 79 months, with a maximum gap between acquisitions of 29 months.

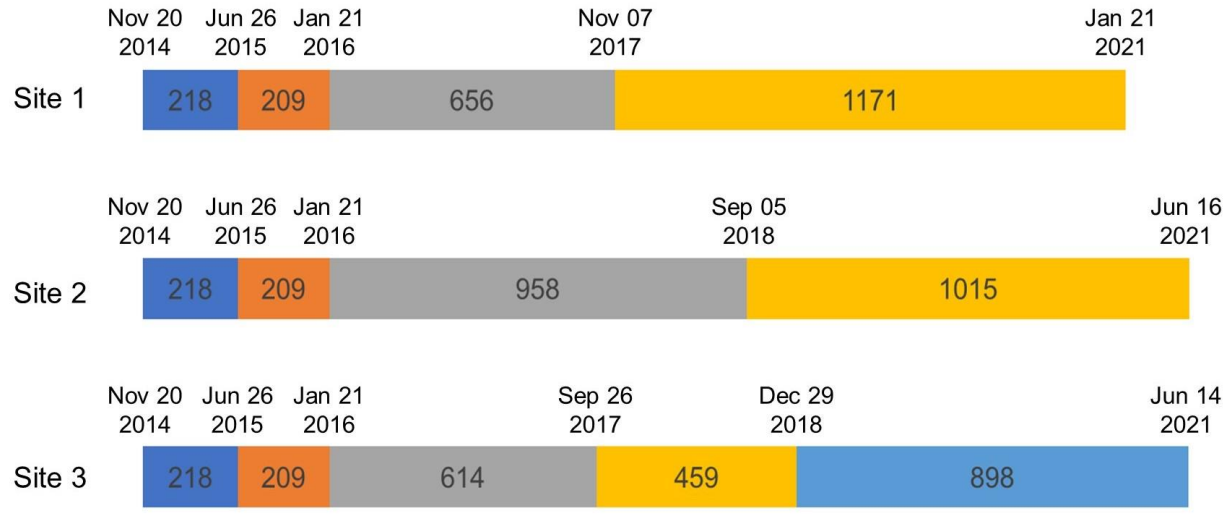

Figure 2.6 The conducted photogrammetric acquisitions at the three sites separated by the time intervals in days.

2.3 Site 1 (MP 042_80)

Site 1 is situated on the western bank of the Colorado River, north of I-70 at MP 042_80 (Figure 2.7). It is located at the eastern end of the Book Cliff, part of the northeastern, southward-facing escarpment of the Grand Valley at the southern entrance of DeBeque Canyon. The rock slope has an ESE-WNW orientation, following the alignment of I-70. The site has a maximum length of 575 m and a maximum height of 163 m, with a total surface area of 78,200 m^2. The site has varying slope angles, ranging from 51° in the lower shale section to almost 90° in the sandstone ledges, with an overall slope angle of 57°.

Alternating vertical sandstone ledges and shale-bearing strata characterize the rock face of this site (Figure 2.8). The exposed rock belongs to the Mount Garfield FM, and consists of brown, grayish-white, and buff-color sandstone interbedded with gray-color shale, carboniferous shale, and sandy shale. Some layers are carboniferous and exhibit solution cavities. The sandstone varies from massive, fresh, coarse-grained to thinly bedded and fine-grained beds. The thickness of sandstone layers at the site can reach up to 44 m. These layers are affected by different sets of joints, causing detachments of rockfalls that can be observed at the slope face. The shale beds at the lower part of the slope are weathered, reaching up to 24 m in thickness and interlayered with thin sandstone layers. Some lithological units are concealed due to the

accumulation of talus and rock fragments derived from erosion of the sandstone and loose debris of shale-bearing beds. Vegetation is sparse along the slope, with some isolated sagebrush.

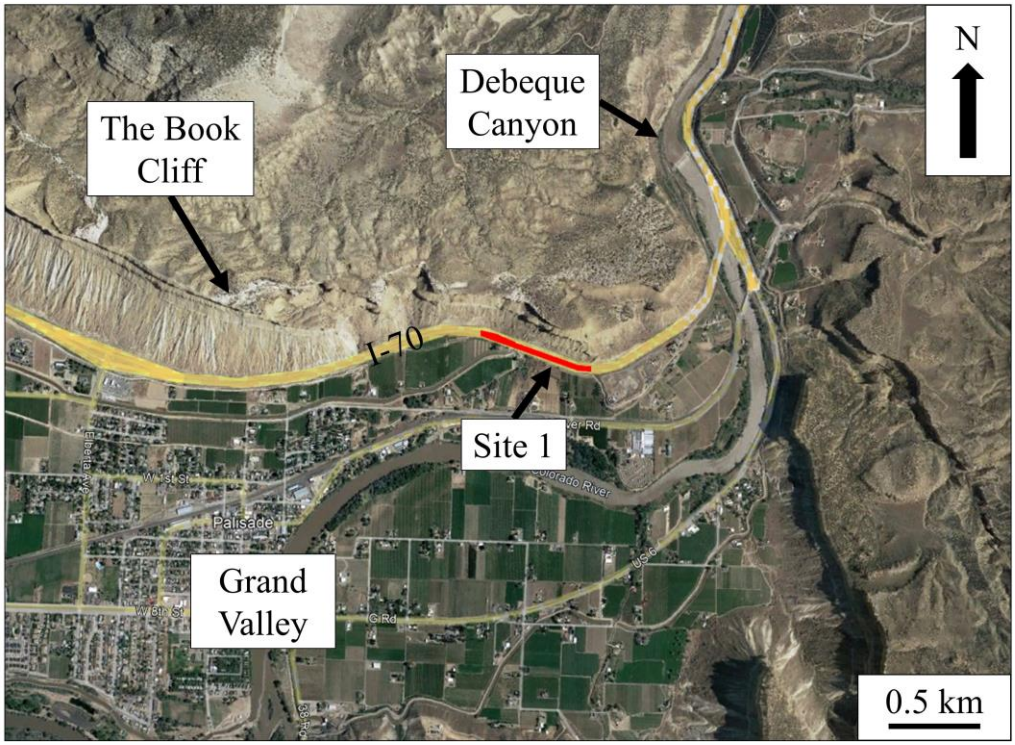

Figure 2.7 Location map of Site 1.

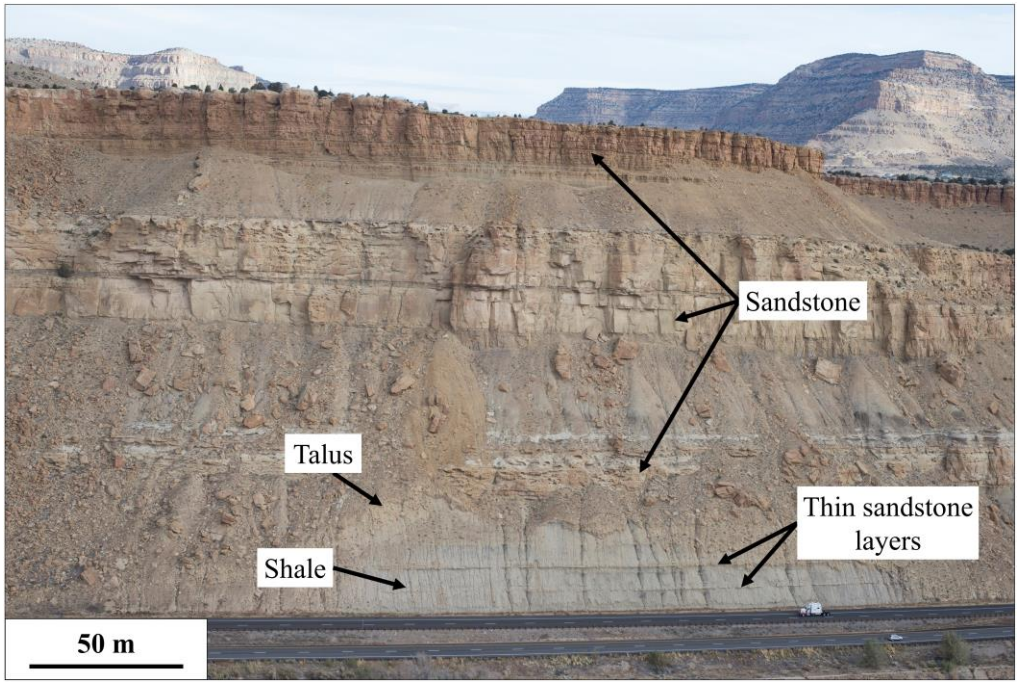

Figure 2.8 Site 1 at MP 042_80 along I-70 highway. Photo courtesy CDOT.

2.4 Site 2 (MP 048_85)

Site 2 is situated on the eastern bank of the Colorado River, in the middle section of DeBeque Canyon at MP 048_85. The site stretches from 1.5 km northeast of James M. Robb State Park to the south to the Plateau Creek tributary of the Colorado River, 0.7 km south of the Grand Valley Diversion Dam (Figure 2.9). It is a northwest-facing natural rock slope, oriented NE-SW. The photogrammetry data for this site covers 771 m of natural slope. This slope has a maximum height of 101 meters and a total surface area of 62,400 m^2. Vegetation appears along this slope in the form of sagebrush and Russian thistle plants.

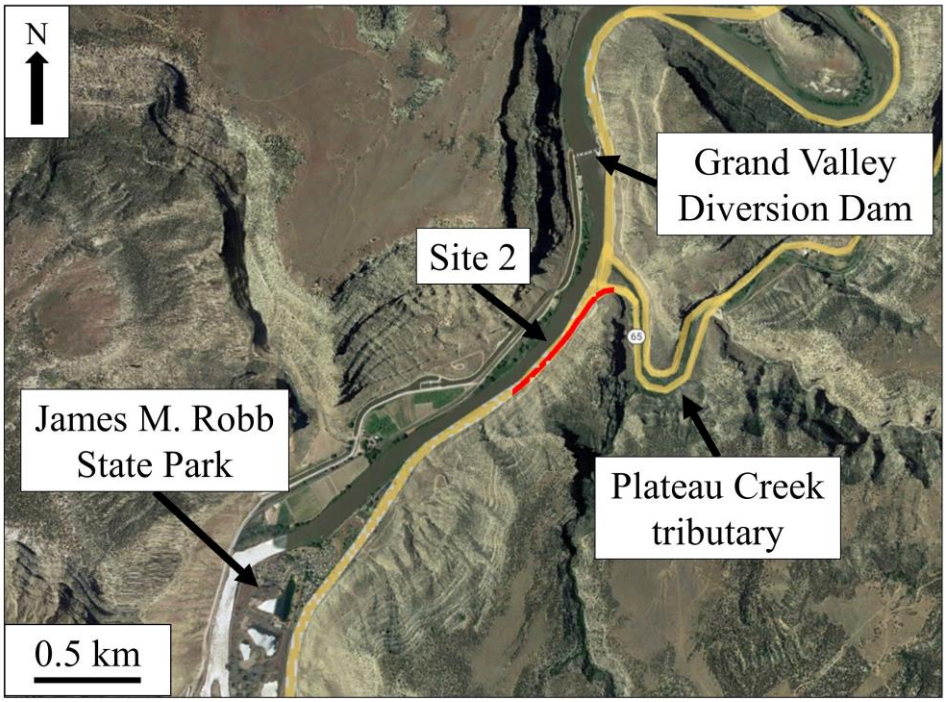

Figure 2.9 Location map of Site 2.

The geology of Site 2 shows less lithological variation than Site 1. The exposed rock at this site belongs to the Mount Garfield formation, which is capped by the Hunter Canyon FM. The shale layers have limited occurrences and smaller thicknesses compared to Site 1. The southern section of the site shows massive rock ledges of sandstone of the Mount Garfield formation (Figure 2.10). The height increases in the northern section of the site, characterized by buff-colored, massive, medium-grained sandstone beds interlayered with gray, thin-bedded shale from the Hunter Canyon FM. This area is also covered by thick talus material (Figure 2.11). The sedimentary layers at this site are sub-horizontal, dipping 4º - 5º towards the southwest. The

thickness of sandstone layers at the site can reach up to 45 m. These layers are primarily massive and are cut by one joint set that runs parallel to the vertical slope face, as well as horizontal bedding planes. A historical landslide can be observed in the northern section of the site. Variable thicknesses of vegetated colluvium deposits and talus materials are present, with an increased thickness toward the northern side.

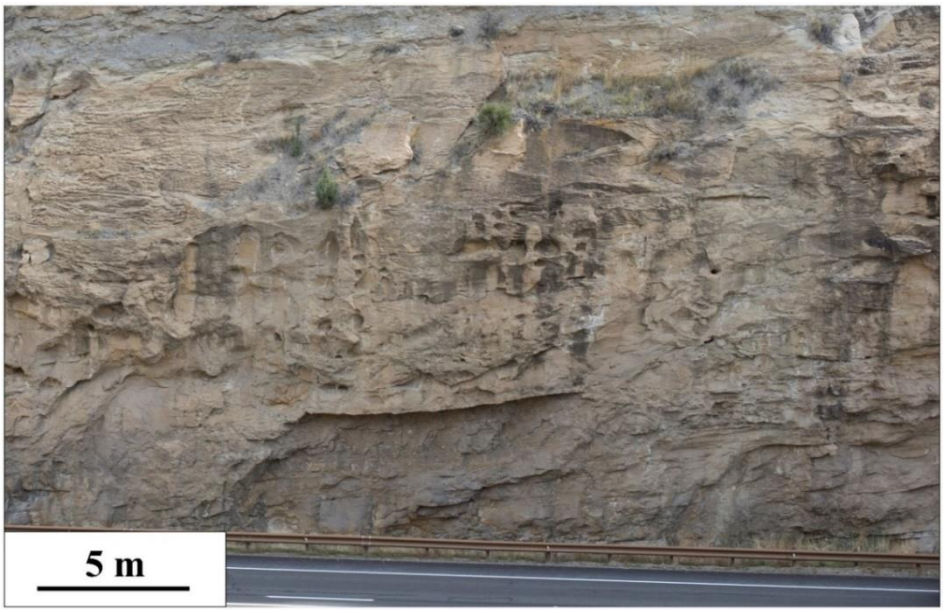

Figure 2.10 The exposed massive sandstone at the southern part of Site 2. Photo courtesy CDOT.

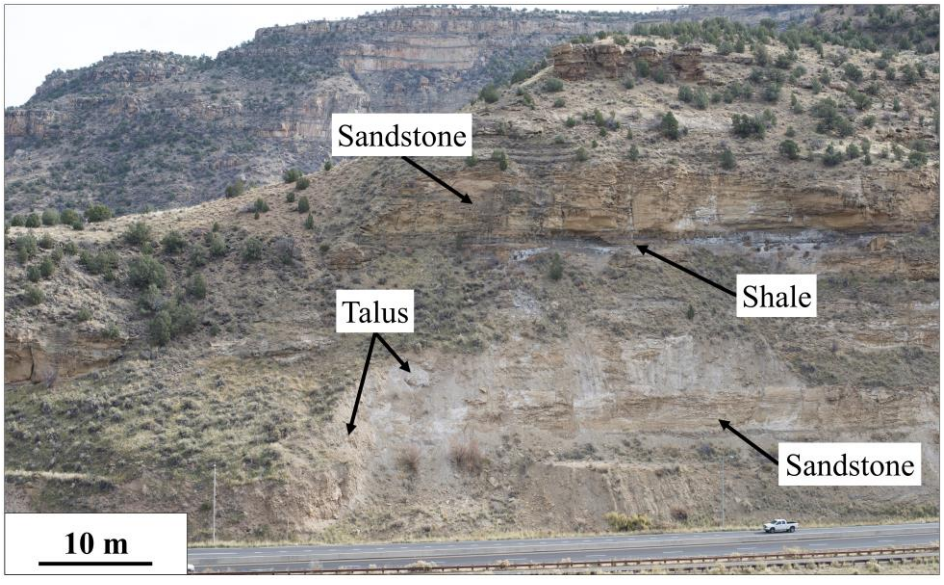

Figure 2.11 Exposed rocks at the northern side of Site 2 showing the historical landslide. Photo courtesy CDOT.

2.5 Site 3 (MP 056_50)

Site 3 is situated on the eastern bank of the Colorado River, at the northern entrance of DeBeque Canyon at MP 056_50, 8 km southwest of DeBeque city (Figure 2.12). It is a northwest-facing natural rock slope, oriented at NE-SW direction. The photogrammetry of this site covers 1,220 m length of the natural slope with a maximum height of 79 m and a total surface area of 89,600 m^2. Vegetation is also widespread along this slope with sagebrush and greasewood plants. The slope has varying slope angles, ranging from 38° in the northern section to nearly vertical in the southern section.

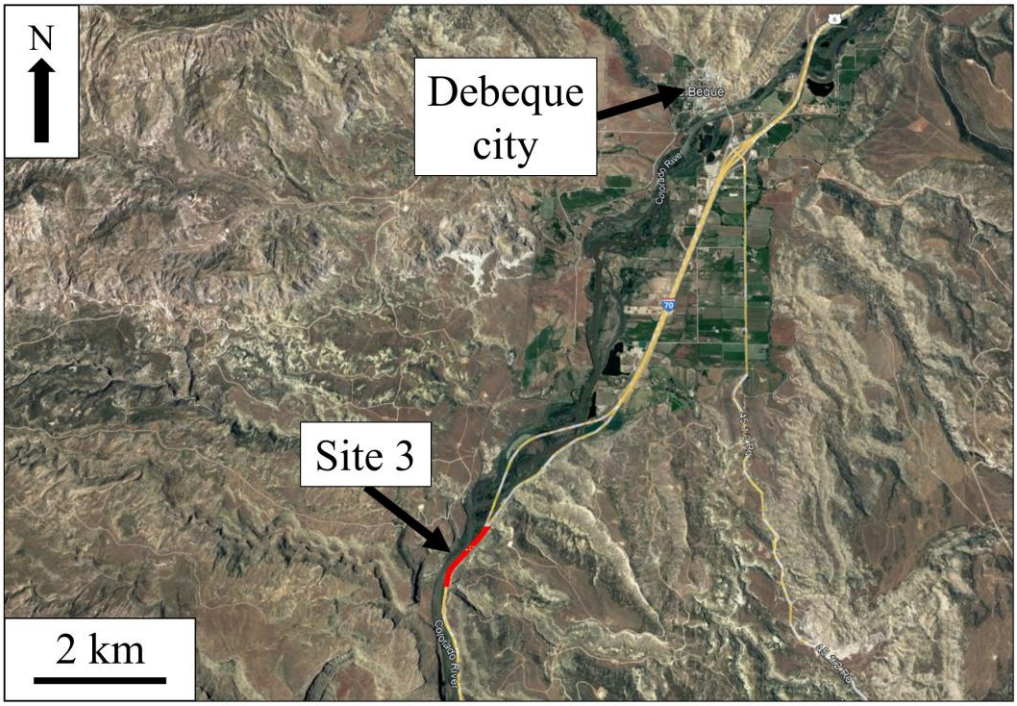

Figure 2.12 Location map of Site 3.

The exposed rock at the site belongs to the Mount Garfield formation that is capped by the Hunter Canyon FM. The Mount Garfield formation consists of fine-grained, grayish-white to gray sandstone interlayered with gray, thin-bedded shale. This formation is overlain by a buff-colored, massive, medium-grained sandstone of the Hunter Canyon FM. The sedimentary layers at this site are sub-horizontal, dipping 4º - 5º towards the southwest (Figure 2.13). A slight accumulation of colluvium is observed at the toe of the slope along the site. The outcropped sandstone beds are cut by multiple joint sets.

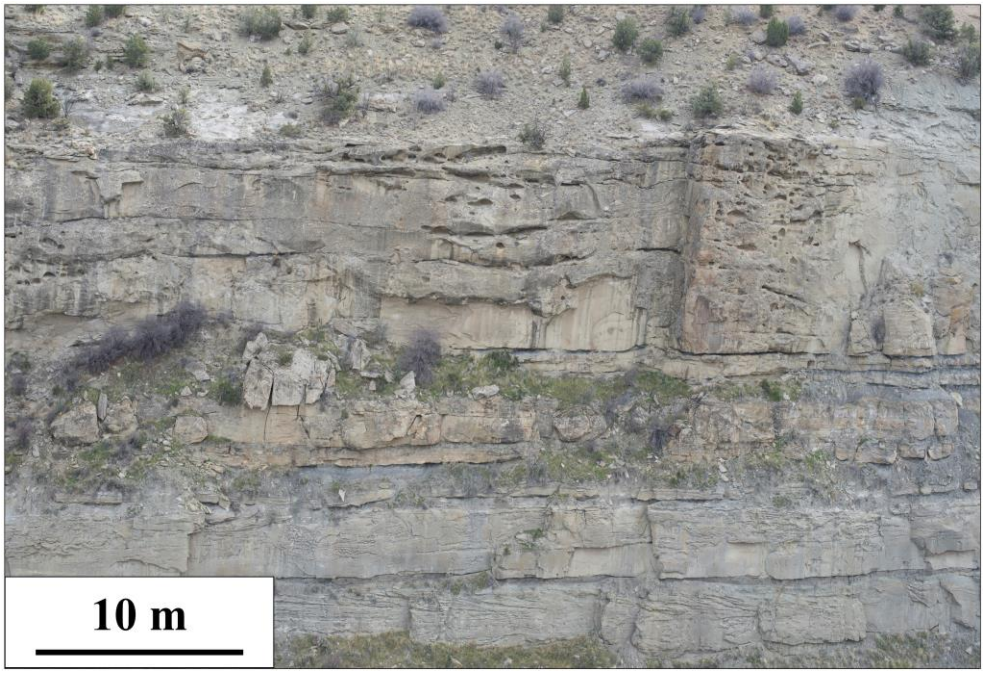

Figure 2.13 The exposed horizontal sandstone at Site 3. Photo courtesy CDOT.

CHAPTER 3 METHODS

This chapter details the applied workflows for creating photogrammetric models, conducting change detection analyses, and obtaining structural data. The applied methodology is based on the workflow described by Graber and Santi (2022a), with some modifications (Figure 3.1). The creation of photogrammetric models and data processing were limited to the first and last datasets (2014 and 2021). With this approach, the total number of rockfalls during the monitoring period was identified. Next, the photos of the intermediate image datasets (between 2014 and 2021) were manually evaluated to determine the time of occurrence of every rockfall.

The data processing starts with the creation of a high-resolution photogrammetric model from aerial photos collected by the UAVs. The Agisoft Metashape Professional software, version 1.6.1, was utilized for this purpose. The selection of parameters for model creation is based on the guidelines provided in the Metashape manual and related studies in the literature (Schwind, 2016; Brach et at., 2019; Graber and Santi, 2022a). The selected parameters were adjusted based on the dataset's quality and specific site requirements. Table 3.1 demonstrates the image datasets and photogrammetric model parameters for the three sites.

The assessment of the image datasets showed that the conducted photogrammetry acquisitions are inconsistent regarding the used camera model, UAVs flight plan, and acquisition timing. These inconsistencies resulted in varying data qualities and quantities. For example, Site 1 was imaged in 2014 using a NIKON D600 camera with a 50 mm focal lens. In 2021, it was imaged using a ZH20 camera with a 10.14 mm focal lens. The range of imaging also varied between acquisitions. In 2014, data collection at Site 1 was conducted through three flight lines of different ranges and elevations. In 2021, the acquisition was conducted through eight survey lines of the same imaging range but variable elevations. This is reflected in the resulting number of images, with 59 images collected in 2014 and 623 in 2021 at Site 1. Most acquisitions were conducted in clear weather, while some were conducted when snow covered most of the slope. It was also noted that geo-reference information was not recorded in all datasets, and only datasets from 2017 to 2021 are geotagged. These variations affect the quality of the resulting images, which needed extra processing before they could be used to build the photogrammetric models.

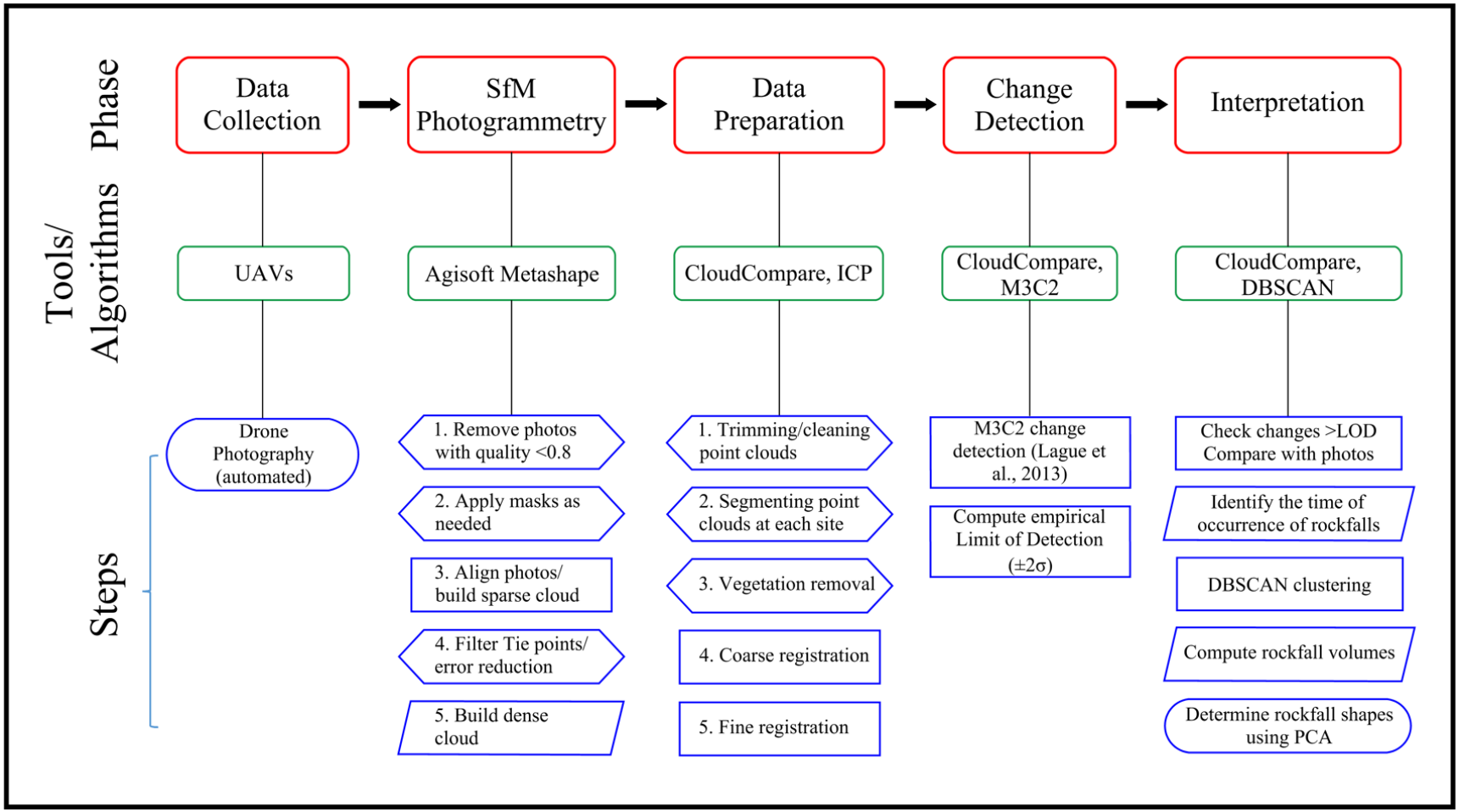

Figure 3.1 The implemented workflow for data acquisition and processing, adapted from Graber and Santi (2022a). Steps with numerical order should be executed sequentially.

Table 3.1 Image datasets and photogrammetric model parameters for the three sites.

Specs/ Parameters	Site 1		Site 2		Site 3	
	2014	2021	2014	2021	2014	2021
Number of images	59	623	136	381	194	839
Camera Model	NIKON D600	ZH20	NIKON D600	ZH20	NIKON D600	ZH20
Resolution	6016 x 4016	5184 x 3888	6016 x 4016	5184 x 3888	6016 x 4016	5184 x 3888
Focal Length	50 mm	10.14 mm	50 mm	10.14 mm	50 mm	10.14 mm
Pixel Size (μm)	5.97 x 5.97	1.44 x 1.44	5.97 x 5.97	1.44 x 1.44	5.97 x 5.97	1.44 x 1.44
Align Accuracy	High	High	High	High	High	High
Generic preselection	No	No	No	No	No	No
Reference preselection	Sequence	Source	Estimated	Source	Estimated	Source
Key point limit	40,000	40,000	40,000	40,000	40,000	40,000
Tie point limit	4,000	4,000	4,000	4,000	4,000	4,000
Dense Cloud quality	High	High	High	Medium	High	High
Filtering mode	Aggressive	Aggressive	Aggressive	Aggressive	Aggressive	Aggressive
Tie points	26,461	193,283	62,076	97,798	133,449	251,055

3.1 Photogrammetry Model Construction

The “Estimate Image Quality” tool in Metashape was used to filter out the blurry and low-contrast images, which could negatively affect the resolution of the models. A quality threshold of 80% was applied, removing lower-quality images. Masks were applied as needed to exclude any unwanted portions of the photos from being included in the final models. This helped to reduce the processing time by decreasing the number of pixels that to be analyzed for matching key points. For close-range image datasets, like 2021, most photos captured the slope face and did not require any masking. However, for the distant-range images, like in 2014, the sky was captured and had to be removed. If any noisy locations were retained, they were manually removed later from the tie or final dense cloud.

Having no basis to set pre-calibration parameters led to solving for the camera parameters by Metashape during model construction. As GCPs were not utilized in the photogrammetry, the

direct geo-referencing approach was used in the processing. The position information of the camera was obtained from the Exchangeable Image File Format (EXIF) metadata for referencing the key points to a global coordinate system. The models without recorded coordinates were created in a local coordinate system until being aligned to a geo-referenced model.

The “Align” step in Metashape was performed after the camera calibration had been set up. This step utilized SfM algorithms to obtain the tie/sparse point cloud. In Metashape, the identification and description of key features, feature matching, estimation of camera positions, triangulation, and bundle adjustment were all applied automatically as part of the 'Align' step. Metashape can optimize different accuracy ranges for the image datasets, from lowest to highest, depending on the purpose of the model. Producing models for accurately detecting rockfalls requires working with high-resolution images. According to the Metashape manual, using the “High” option maintains the original resolution of the images. In contrast, the “Medium” option reduces the resolution by a factor of four, and the “Low” option reduces it by a factor of 16. In this study, photos were aligned using the “High” option to achieve high accuracy while reducing the processing time compared to the “Highest” option.

In order to match image pairs with high accuracy and obtain a greater number of tie points, the “Generic preselection” option was not applied. This option typically accelerates the matching process by using lower accuracy settings first, which has the potential to return fewer number of tie points with lower accuracy. Instead, the “Reference preselection” option was chosen, in which different settings were used for construction of the 2021 and 2014 models. For the 2021 image datasets with recorded georeferenced information, the “Source” option was used. This option expedited the matching process by selecting image pairs based on the calculated camera positions. This option was appropriate to use for the 2021 models, where numerous images were captured and geotagged, allowing for highly accurate calculation for the camera positions. For the 2014 image datasets, lacking georeferenced information, two alternative options were used: “Sequence” and “Estimated.” The “Sequence” option relied on the camera order for selecting matched images taken sequentially, using the sequence number of images. The “Estimated” option was used when the camera positions were not precisely calculated but could be estimated from external information such as flight path.

The "Key point limit" and "Tie point limit" define the maximum number of key points to be detected and the maximum number of matching tie points in every image. Defining these

numbers depends on the desired quality and processing time. If both parameters are set to zero, an unlimited number of points will be detected and matched. This will significantly increase the processing time and might produce low-quality tie points that should be excluded from the model. The number of tie points affects the quality and resolution of the final dense point cloud. The constructed depth maps needed to densify the tie point cloud cannot be generated for images with fewer than 100 tie points (Metashape User Manual, 2023). In general, having more tie points leads to better depth map reconstruction and, consequently, a more accurate dense point cloud. However, the relationship between the number of tie points and model quality is not always linear. This is because other factors such as image quality and overlap also contribute to the overall quality of the model. As the Metashape manual recommends, the "Key point limit" was set to 40,000, and the "Tie point limit" was set to 4,000 points. The settings used ensure that the number of tie points is sufficient for creating a high-resolution dense point cloud without missing any sections.

Finally, the tie point clouds were created; these clouds had varying numbers of points, depending on the resolution of the image datasets and the selected processing parameters. Table 3.1 shows the different numbers of points in the tie point clouds for the three sites in 2014 and 2021. The number of tie points generated in 2021 is higher than 2014, which is consistent with the resolutions and number of images in each dataset.

The resulting tie point clouds were then filtered using iterative error reduction techniques based on the reconstruction uncertainty, projection accuracy, and re-projection error to eliminate poor-quality tie points. Removal of poor-quality tie points increases the accuracy of the estimated internal and external camera parameters. The error reduction process started by applying “Reconstruction uncertainty” to filter out points produced from a poor estimation of camera locations. This eliminates the poorly estimated points during triangulation and projection steps. Removing points with high reconstruction uncertainties reduces the occurrence of noisy locations in the model and keeps the accurate points for the subsequent filtering steps. The second step in the error reduction process was to exclude points with relatively low projection accuracy. The third applied step in error reduction was filtering by “Reprojection error” to eliminate points with low 3D projection accuracy onto the images. It represents the actual position of the constructed tie point relative to its location on the images.

Metashape creates depth maps that will be used along with the camera positions to obtain the densified point clouds. The software provides various options for creating depth maps depending on the details of the surveyed surface. The quality options for creating depth maps are identical to those for the aligning step. For this thesis, the dense clouds were built using the "High" quality option to ensure getting high-resolution models necessary for the change detection process. The "Depth filtering" options eliminate outliers from the point. The "Aggressive" depth-filtering mode was chosen, which is suitable for large-scale models to reduce the number of points and speed up processing time.

The length of the resulting high-resolution dense point cloud varied from 575 m on Site 1 to 1,220 m on Site 3. Processing the whole site at once created a doming effect in the point clouds. This is a common issue in photogrammetric models caused by systematic errors, such as inaccuracies in camera calibration and distortion in the images (James and Robson, 2014, Smith and Vericat, 2015). As the model size decreases, the overall elevation differences within the model decrease, making the distortion and doming effect less significant. In larger models, errors propagate across the models, increasing the doming effect. In smaller models, error propagation is confined within each segment, minimizing the overall impact of the doming effect. Therefore, to reduce the influence of the doming effect on change detection and the computational time for future analyses, the point cloud models were divided into several smaller parts. These smaller parts were 50-90 m wide each with minimal local distortion prior to further analysis. The number of segments for Sites 1, 2, and 3 are 9, 13, and 16, respectively. The subsequent processing procedures were conducted on a segment-to-segment basis.

In order to assess the accuracy of the direct geo-referencing method, the resulting photogrammetric point clouds were compared to lidar surveys for Sites 1 and 3. Site 2 did not have any lidar surveys available for comparison. For this evaluation, three segments each from Sites 1 and 3 (six total) were randomly selected. These segments had lengths ranging from 60 to 80 m and were distributed along the full extent of each site. The distances between the points were calculated to obtain the root-mean-squared (RMS) of the differences, which provided a quantitative evaluation of the accuracy of the created point clouds.

3.2 Change Detection

All processing steps related to change detection were conducted on the dense point clouds using CloudCompare (CloudCompare, 2021) software. The goal was to detect changes between

datasets from different epochs and extract the rockfall information such as locations, times of occurrence, and volumes. The basic workflow suggested by Tonini & Abellán (2014) and Van Veen et al. (2017) was optimized for the site-specific application. First, any visibly noisy or unwanted portions of the point clouds were trimmed. Additionally, for each site, the point clouds of 2014 and 2021 were trimmed to have the same extents.

The georeferenced models obtained in 2021 were used as a reference to align the 2014 models that do not have position information. The scale and orientation of the aligned models were adjusted to match the reference point cloud. The first step of alignment was conducted using coarse registration, in which manual point picking was used to match features between the two point clouds. The increased number of picked points improves the accuracy of the aligning process. A minimum of three points are required for this step. However, 20 to 45 points were selected in every segment, depending on the variations along the site and the length of segment (Figure 3.2). Although this step was time-consuming, the quality of the coarse alignment is critical, as it affects the accuracy of the subsequent steps.

A further fine alignment was conducted using the built-in Iterative Closest Point (ICP) algorithm (Besl & McKay, 1992) in CloudCompare. This algorithm compares the two point clouds by checking every point in the reference cloud and searching for the closest point in the aligned cloud. Upon detecting the closest point, the algorithm estimates the required translation and rotation to be applied to the aligned cloud to match these closest points. The algorithm also allows for adjusting the scale of the aligned point cloud to fit the reference one. These steps are repeated iteratively until the RMS distance between points falls below a target threshold.

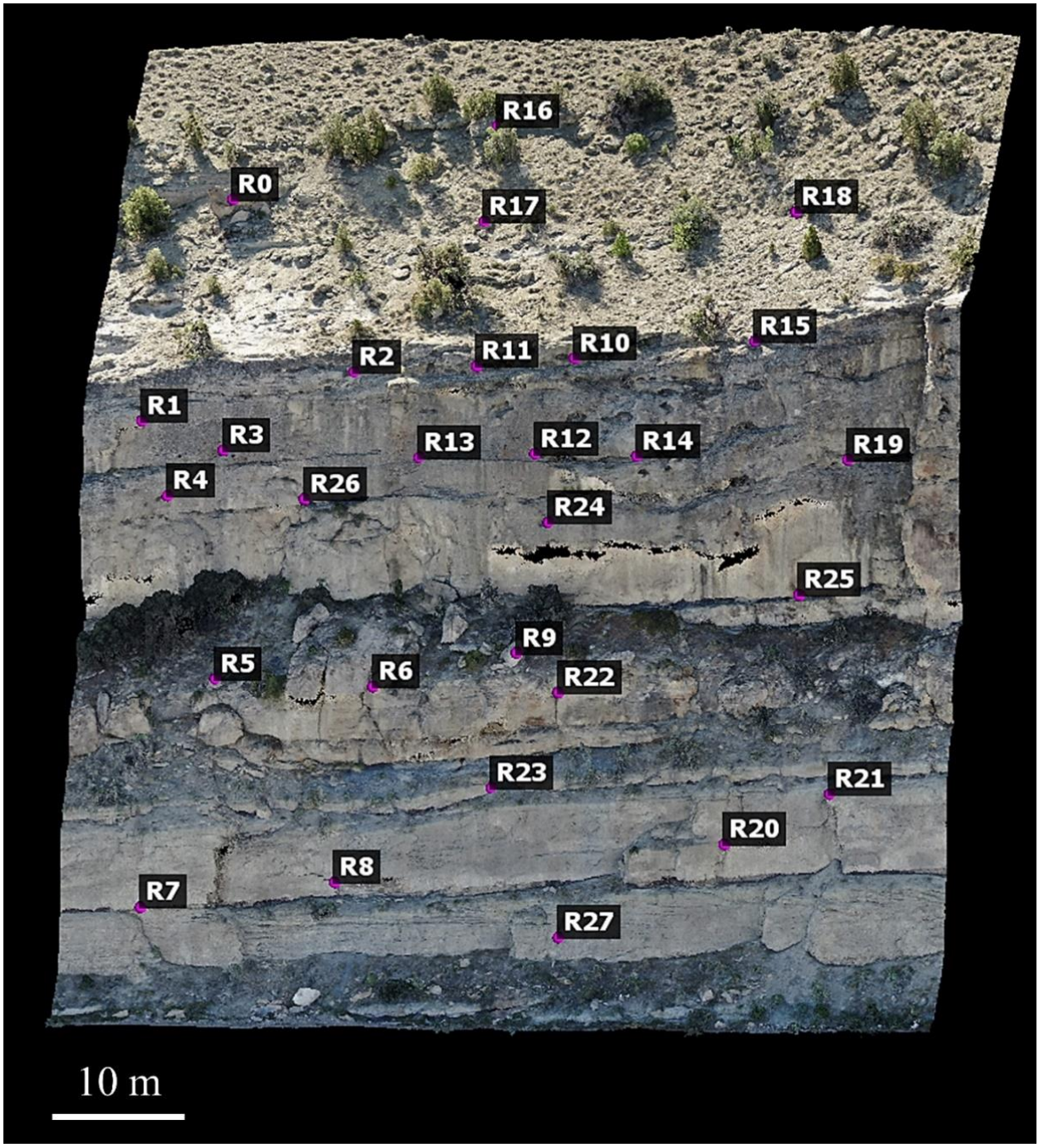

Figure 3.2 Example of the conducted coarse registration in CloudCompare.

The presence of vegetation along slopes can give a false positive or negative indication to rockfalls because of the change in density across seasons. Therefore, excluding vegetation from the point clouds is preferred before the calculation of change values. Removal of vegetation can be done in several ways, including manual segmentation or applying a classification algorithm. For this thesis, vegetation was manually cropped out and excluded from the point clouds.

The change detection was conducted between the 2014 and 2021 point clouds to identify changes over the entire monitoring period. The M3C2 algorithm (Lague et al., 2013) was used to compute the differences between the cleaned and aligned point clouds. The algorithm starts by defining a neighborhood scale (D) within cloud 1. It then identifies a change direction (N) perpendicular to the plane fitted to the points inside the diameter of the neighborhood scale, as shown in Figure 3.3 (DiFrancesco et al., 2020). Subsequently, the distance between the average point locations within a cylinder (diameter "d") projected along the change direction in both clouds is identified. This projection diameter is chosen based on many factors, such as the surface complexity, quality of the data, point spacing, and roughness of the clouds. Using a larger scale results in a smoother surface representation, whereas a smaller scale captures minor roughness details on the surface.

DiFrancesco et al. (2020) recommended a projection diameter of one to two times the point spacing for working with lidar data. However, preliminary testing showed that using projection diameters within this range for the photogrammetry point clouds led to increased levels of noise. This noise, in turn, resulted in overestimates of rockfall volumes. In this study, both projection diameter (d) and normal scale (D) were assigned values within the range of 0.20 to 0.25 m. This range corresponds to point spacing ranging from 0.065 to 0.09 m at the three sites. Using a diameter that is two to three times the point spacing achieved a balance between avoiding excessive smoothing of rockfall geometries and minimizing noise. All points in each point cloud were used as core points (no subsampling was used for the change calculation).

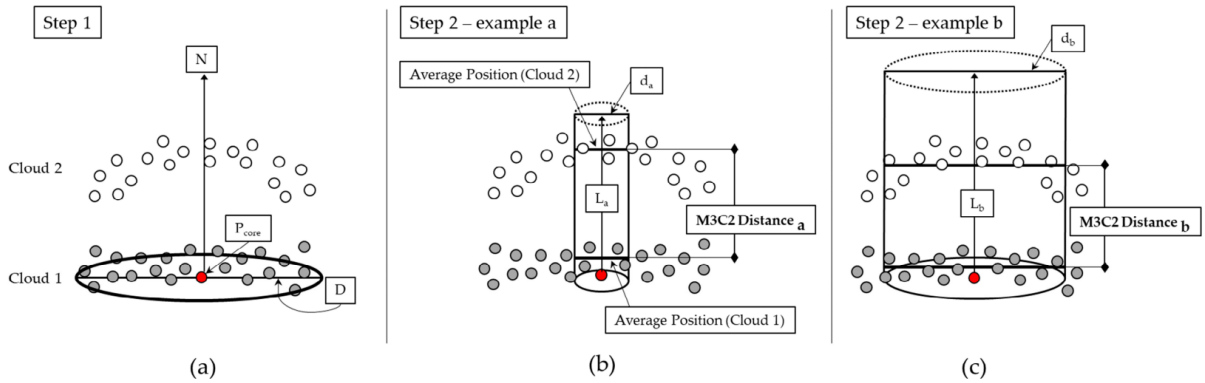

Figure 3.3 Steps of M3C2. a) The selection of the neighborhood scale (D); b) & c) show different projection diameters (d) (DiFrancesco et al., 2020).

The resulting change detection maps show the distance differences between the point clouds. The Limit of Detection (LOD) was obtained based on the normal distribution of these differences in areas without observed change. The LOD, equal to ±2 standard deviations of the mean of the curve, represents the threshold below which change is not considered significant. The geometric distortions in the segmented point clouds are reduced to a level substantially smaller than the LOD. This makes them negligible when only considering changes exceeding the LOD. As shown in Table 3.2, the standard deviation ranges from 0.08 to 0.11 m, and the corresponding LOD ranges from 0.16 to 0.22 m, accordingly.

Table 3.2 Identified LOD at the three sites.

Site #	Std. Dev. M3C2 distance (m)	Empirical limit of detection, ± 2σ (m)
1	0.08	0.16
2	0.11	0.22
3	0.11	0.22

The M3C2 change detection was conducted in both the forward and backward directions, where the former calculates changes from 2014 forward and the latter from 2021 backward. After change calculation, changes below the estimated limit of detection for each site were filtered out. Combining the remaining points for both change maps allowed for a single cloud with both the front and back faces of rockfalls to be developed. The corresponding change points were then clustered using the Density-Based Spatial Clustering of Applications with Noise (DBSCAN) algorithm (Ester et al., 1996). Prior to clustering, these points were filtered out based on the minimum number points and the maximum distance “epsilon” between two points. Preliminary testing determined a threshold of 100 points and an epsilon value of 0.5 for the points to be considered in each cluster. The resulting clusters were visually inspected to check whether these were actual rockfalls or caused by unfiltered vegetation or noise in the cloud. To confirm these rockfalls, the photo datasets from 2014 and 2021 were reviewed for each identified rockfall location. For cases where rockfall was detected at the edge between two segments, a new smaller segment from the original point cloud was created. This new segment included the entire rockfall (Figure 3.4). The change detection process was then repeated for these smaller segments.

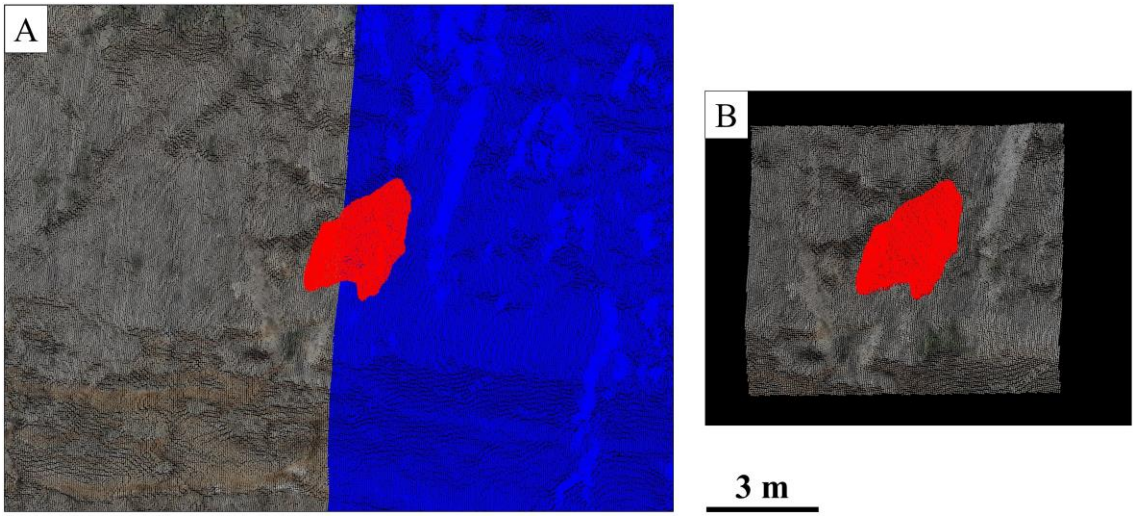

Figure 3.4 Example of a rockfall detected between two segments. A) The rockfall is situated between two segments (gray and blue colors). B) A new smaller segment was created that encompassed the whole rockfall.

The time of occurrence of each rockfall was determined by reviewing the photo datasets from 2015, 2016, 2017, and 2018. This helped to identify when the rockfall occurred without the need to build a separate photogrammetric model for each acquisition. Generally, the proposed approach for identifying the spatial and temporal occurrence of rockfalls from images proved effective and Figure 3.5 shows an example segment along the three sites.

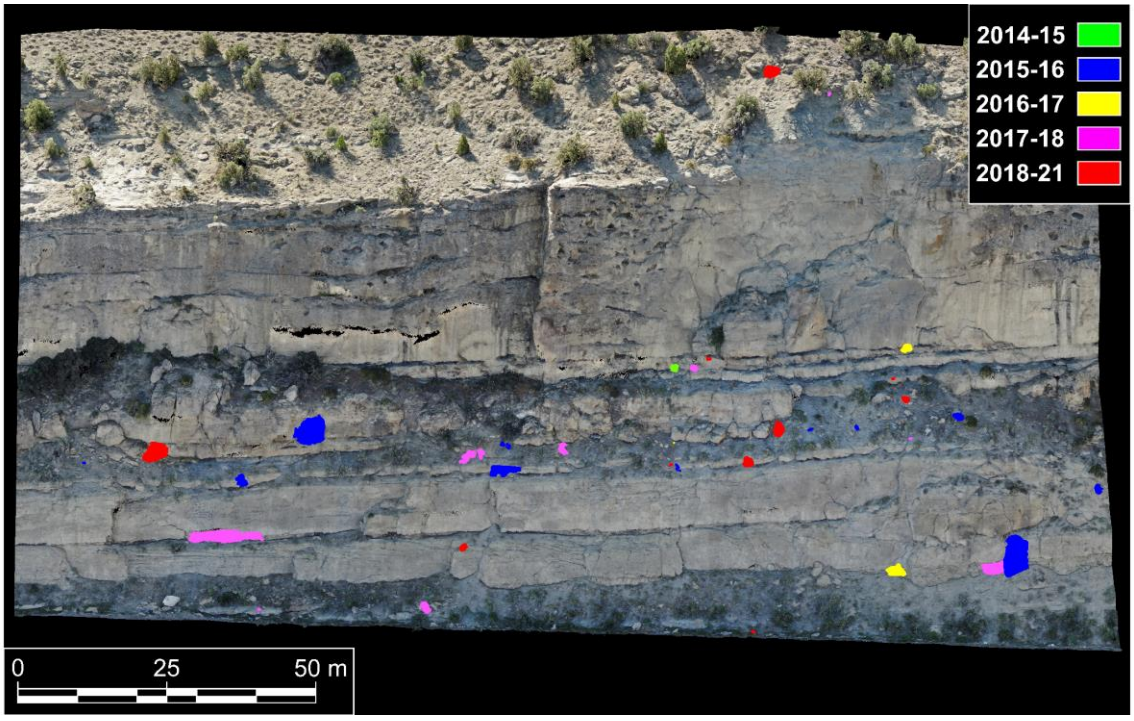

Figure 3.5 Example of the determined time of rockfall occurrences at Site 3.

Reviewing rockfall occurrences in photos also allowed for the segmentation of large rockfall clusters, which combined different rockfalls that occurred at different times. The rockfalls were manually segmented based on spatial extents estimated from the photos and assigned a corresponding time range of occurrence. Once the rockfalls were identified, the shape of each cluster was reconstructed, and the volume was estimated. The volume calculation was performed using the Alpha Solid algorithm (DiFrancesco et al., 2021), using a code developed in Matlab.

Four cases were observed at the three sites, as summarized in Table 3.3. Figure 3.6 illustrates case 3, where the calculated rockfall change region corresponded to two connected smaller rockfalls. The larger portion fell during the 2015-16 period, and the smaller portion fell later (between 2017 and 2018). The initially obtained total rockfall volume was 6.5 m^3. After segmentation and recalculating the volumes for the two segments, the resulting volumes were 7.0 x 10^{-1} m^3 and 5.7 m^3. The sum of individual rockfall volumes for the four cases after segmentation range from 98 to 100 % of the original volume. This demonstrates that the applied manual segmentation approach introduces minimal error into the rockfall volume estimation process.

Table 3.3 Cases for the manual segmentation at the three sites.

Case #	Site #	Volume before segmentation (m^3)	Sum of individual rockfall volumes after segmentation (m^3)	Difference (%)
1	1	4.0	3.9	2
2	2	1.9	1.9	0
3	3	6.5	6.4	2
4	3	6.6 x 10^{-1}	6.5 x 10^{-1}	2

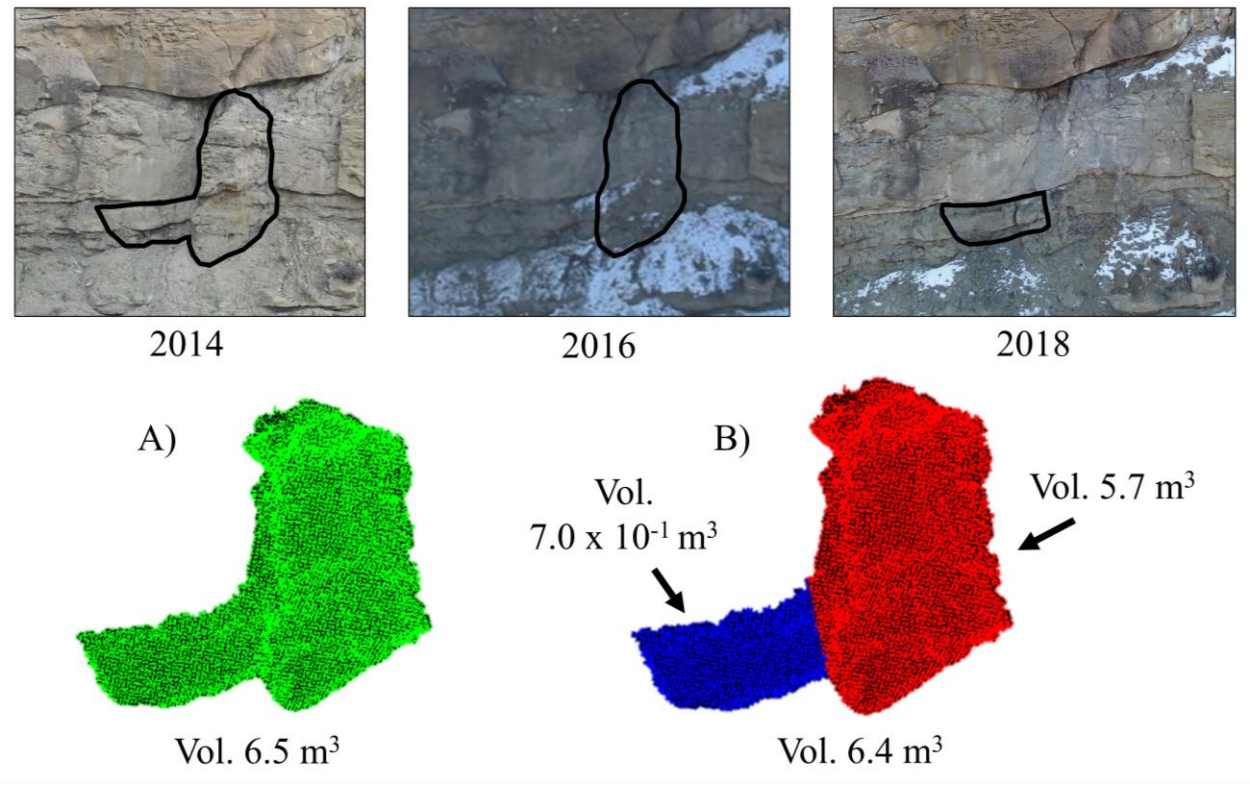

Figure 3.6 Effect of manual segmentation on the resulting volumes at case 3. A) The original cluster between 2014 and 2021. B) The segmented clusters based on the image datasets review.

3.3 Structural Mapping

Considering the extensive length of the sites and the consistent distribution of structures at each of the sites, comprehensive structural mapping was carried out on representative segments from the mapped sites. Structural mapping was conducted for one segment each at Sites 1 and 3. Site 2 was not considered for mapping because it consists primarily of massive sandstone with limited joints. Visual checking revealed that structural trends were generally similar throughout the entire sites. The selected segments at Sites 1 and 3, had the highest number of structures and represented all the joint sets in the slope. For each considered segment, all visible structures, including joints and bedding planes, were identified and documented. The orientation, spacing, and persistence of all structures were recorded. Manual mapping was used as opposed to an automated fracture extraction (e.g. Riquelme et al., 2014), as such algorithms typically rely on the ability to detect sharp changes in elevation or identify well-defined geological features to delineate structures effectively. However, our point cloud data lacks these clear topographical differences, making it challenging for automated algorithms to accurately identify and map the

geological structures. Ultimately, structural data was collected manually from the point cloud using the “Compass” tool in CloudCompare (Figure 3.7).

During the manual mapping process of structures from point cloud data, key visual criteria were employed to distinguish joints and bedding planes from intact rock and other edge-like features. These criteria involved observing color variations, smoothness of boundaries, and continuity and extent as follows:

- Color variations: Distinct color contrasts between sedimentary layers, such as shale and sandstone, were used as a basis for interpreting the presence of bedding planes and differentiating them from intact rock.
- Smoothness of boundaries: The smoothness of boundaries aided in differentiating joints and bedding planes from linear weathering features, which exhibited irregular edges.
- Continuity and extent: Structures that were continuous and extensive along the mapped sites were interpreted as bedding planes, while more localized and discontinuous features were interpreted to suggest smaller fractures or joints. This distinction assisted in separating joints and bedding from intact rock.

Two methods were employed to measure the orientations from the point cloud. The first involved directly measuring the orientation on visible joint surfaces using the "Plane" tool. This was carried out by selecting a group of points on the planar structure, fitting a plane to those points, and determining the plane's orientation. The second method involved using the "Trace" tool when the joint plane was not directly visible. In this approach, 3D points along the joint trace were connected using a polyline. To estimate the plane's orientation, a best-fit plane was calculated using the set of 3D points that formed the polyline. The "Trace" tool in CloudCompare assumes that the visible joint trace is representative of the overall joint plane orientation. It is important to note that this method might not be as accurate as directly measuring the orientation when the entire joint surface is visible. Both tools were used to identify orientation depending on how the target discontinuity presented in the outcrop.

The persistence and spacing of each joint relative to its nearest neighbor with a similar orientation were measured using the distance-measuring tool in the software. The spacing distributions at Sites 1 and 3 were visualized with spacing values binned to the nearest meter, but binning was not implemented for analysis/calculation purposes. The collected data were then

exported to DIPS software by RocScience (RocScience, 2020) for stereographic projection to identify the joint sets. Terzaghi weighting (Terzaghi, 1965) was applied to overcome orientation bias in the discontinuities that are sub-parallel to the mapping surface.

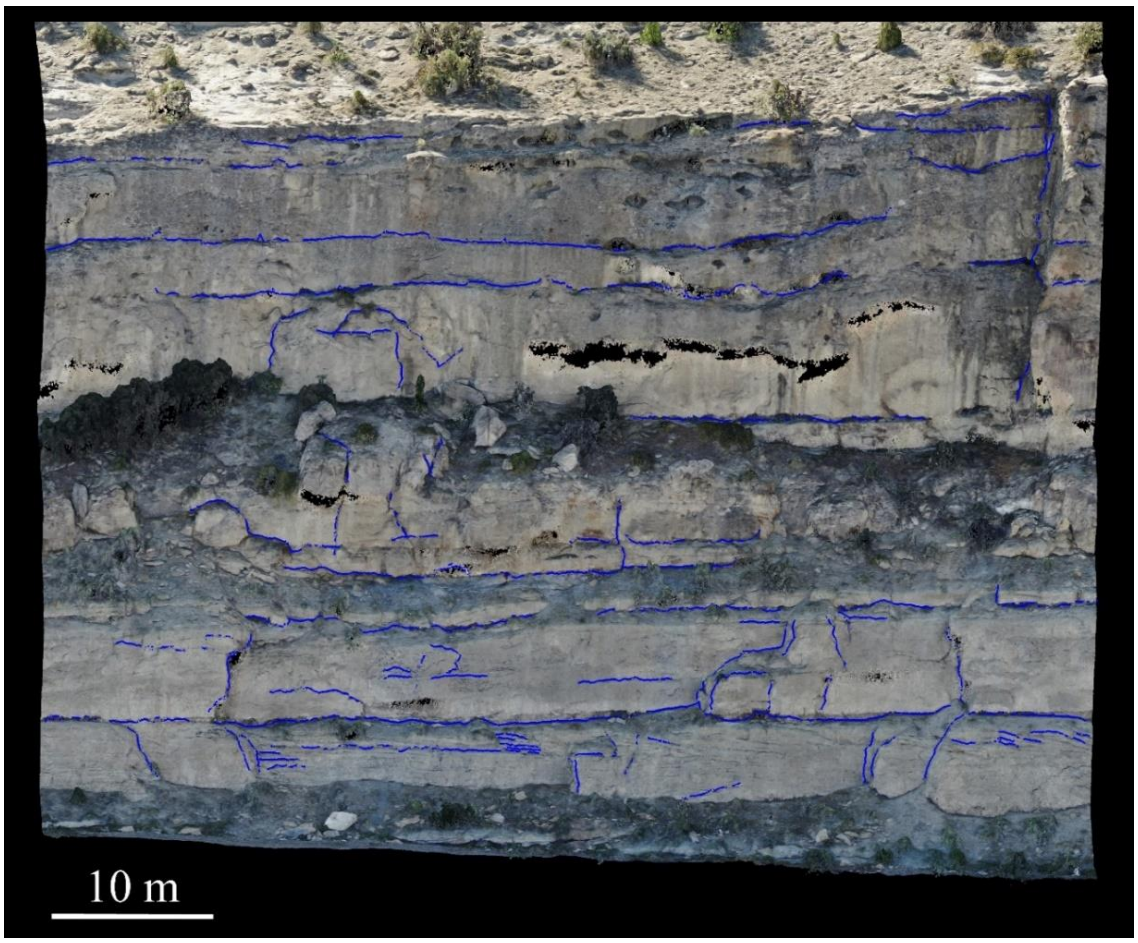

Figure 3.7 Example of the conducted structural mapping on the photogrammetric point cloud.

A comparison was carried out between the expected range of block volumes, based on the mapped structures, and the identified volumes through photogrammetry. Expected block volumes were calculated using the joint spacing (d), and the angle between joints (γ) using the following equation provided by Cai et al. (2004).

$$V = \frac{d_1 \times d_2 \times d_3}{\sin \gamma_1 \times \sin \gamma_2 \times \sin \gamma_3} \tag{3.1}$$

The Monte Carlo Simulation technique was used to apply equation (3-1). This involved randomly selecting a spacing value from the observed range for each joint set in every

simulation. The number of simulations was set to match the number of detected rockfalls at each site. The MCF curves obtained from the simulations were compared to those of the rockfall volumes derived from the change detection process.

3.4 Evaluation of Rockfall Volume and Shape Trends

The accuracy of the rockfall detection was evaluated by determining the minimum consistently detectable rockfall volume "cutoff" at the three sites. This was conducted using the MCF curves obtained from the data and power law distribution analysis. Specifically, the Maximum Likelihood Estimation (MLE) method was applied to detect the cutoff volume. This method iteratively estimates the cutoff volume that gives a minimum Kolmogorov-Smirnov statistic using the MATLAB code provided by Clauset et al. (2009). Rockfall volumes below this cutoff were eliminated and the remaining rockfalls were normalized per year and area to estimate the power law distribution. The full MCF curves for each site were normalized by the total slope area, while the curves for different source zones were normalized based on the exposed area of each individual source zone. The exposed areas for the slopes and each source zone were used as reported by Metashape based on the densified, georeferenced point clouds after being manually clipped to the area of interest.

Determination of rockfall shapes can be used to understand the structural controls of rockfall occurrences. In this research, rockfall shapes were identified according to Sneed & Folk's (1958) classification. This classification proposes ten rockfall shapes categorized based on the ratios between the longest, intermediate, and shortest axes (Figure 3.8). To identify rockfall shapes, Principal Component Analysis (PCA) was used to analyze the x, y, and z coordinates of each rockfall cluster. This helped determine the Principal Components, which correspond to the eigenvalues of the dataset. The ratios between these components were used as representative of ratios between the rockfall axis lengths.

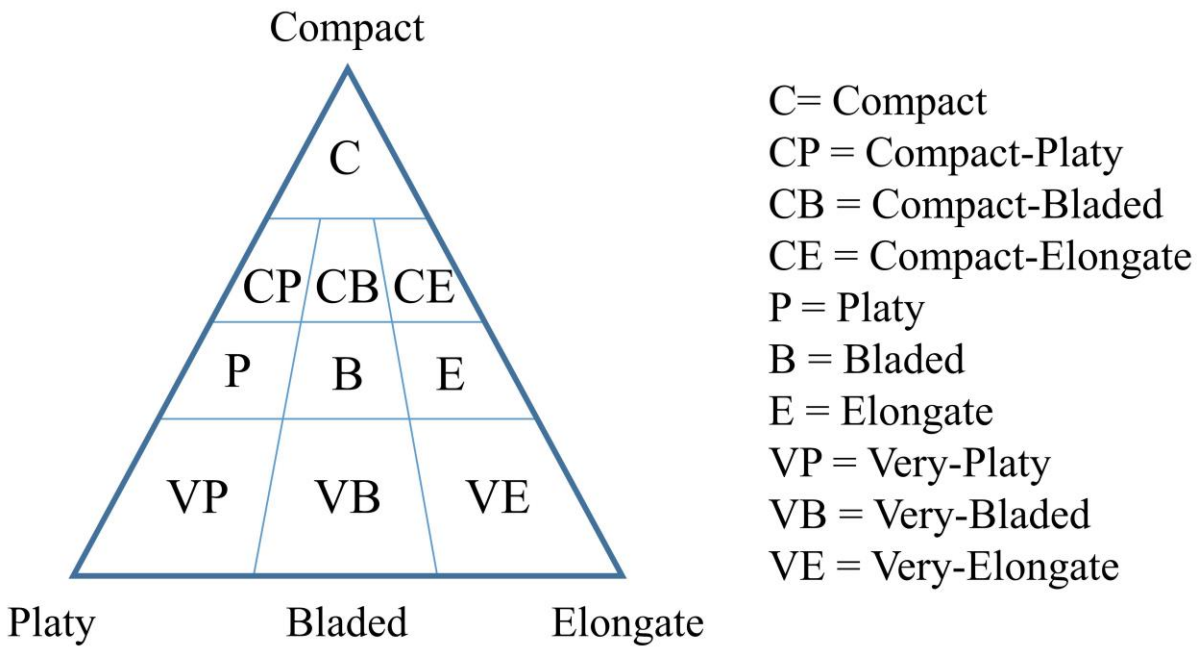

Figure 3.8 The Sneed & Folk's classification, adapted from DiFrancesco et al. (2020).

CHAPTER 4 RESULTS AND DISCUSSION

This chapter presents the results for each site followed by a discussion of their significance. The results include an assessment of the proposed workflow's accuracy. They also include the characterization of rockfall activity along the Canyon and an analysis of the structural impact on rockfalls at each site.

4.1 Site 1

An example photogrammetric model for Site 1 is shown in Figure 4.1, showing some differences in terms of density and point spacing. The densified point cloud of 2014 has 39,424,291 points, while the point cloud of 2021 has 288,842,277 points. The point spacing of the resulting point clouds has an average of 0.06 m.

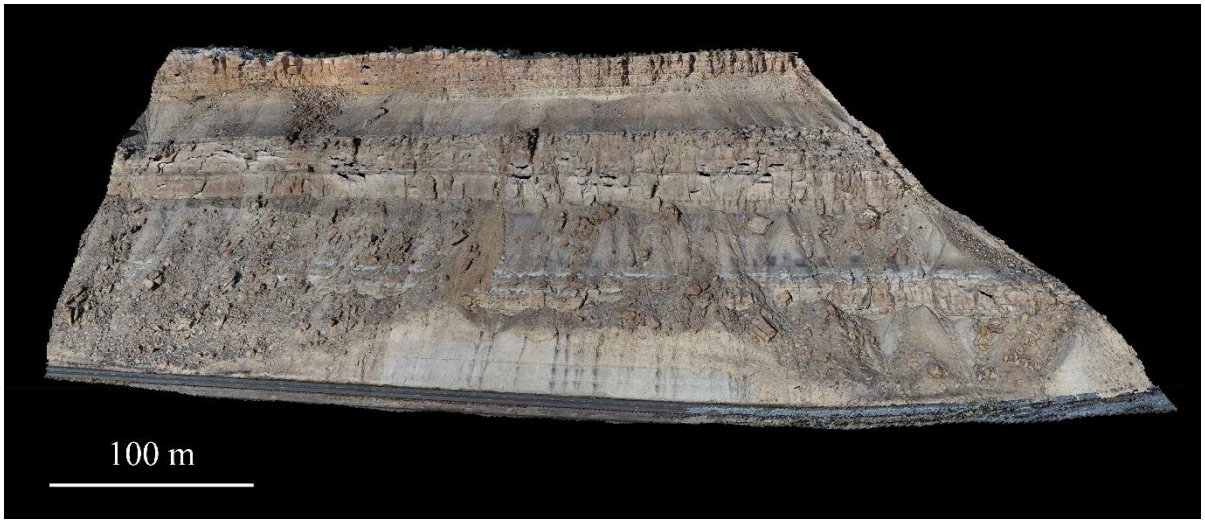

Figure 4.1 Example of the produced photogrammetric models (2021) at Site 1.

The accuracy of direct geo-referencing at Site 1 was evaluated by comparing the distribution of differences between three photogrammetric segments from the 2021 acquisition to the lidar scan. An example segment is shown in Figure 4.2. The resulting RMS difference metric, ranging from 0.059 to 0.063 m from the ICP algorithm, indicates that the point clouds are well-aligned. According to the M3C2 change map (Figure 4.2), it can be visually observed that there is a consistent variation between the lidar and photogrammetry point clouds. A vertical concavity “bowl-effect” associated with the photogrammetric model can be seen. This concavity caused a vertical variation of distances. The photogrammetric model is “in front of” the lidar point cloud at the top and the bottom of the slope and “behind” the lidar point cloud in the middle. This

concavity can be explained by several factors, including inaccurate estimation of the camera's internal parameters, image qualities, lighting conditions, and imaging angles and ranges. The 2021 acquisition was conducted using a fixed imaging angle and range along the whole slope. In order to reduce the "bowl-effect" in future models, the flight plan could be adjusted. Various imaging angles and ranges could be obtained, which would enhance reconstruction quality and reduce geometric distortion (Jaud et al., 2018).

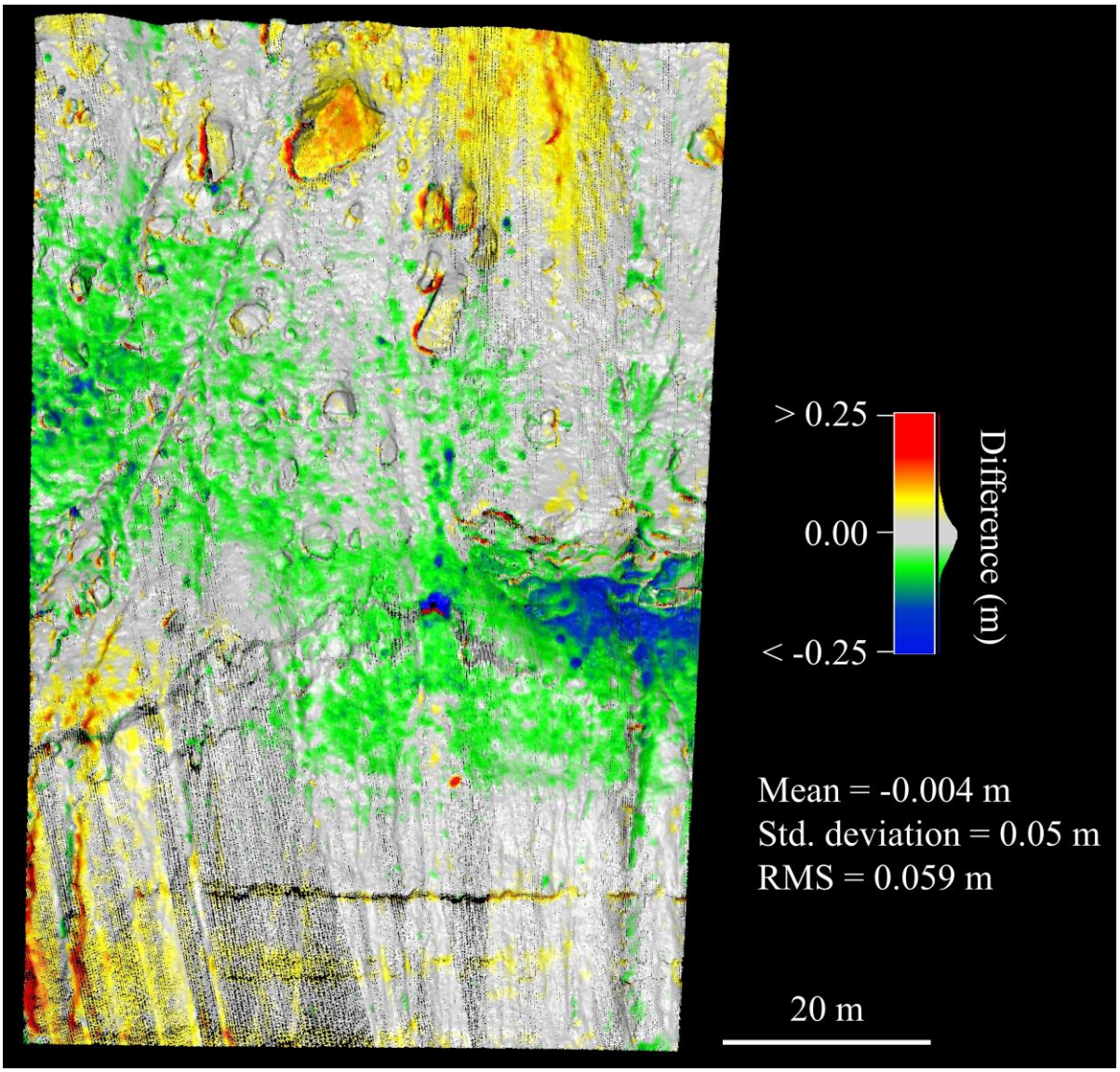

Figure 4.2 The M3C2 differences between a representative photogrammetric segment and a lidar survey at Site 1. Some change below the limit of detection is shown to more clearly illustrate the subtle distortion effects present.

To assess the precision of the change detection process, the LOD was computed to determine the minimum changes that can be detected through the process. The change detection result for a

representative segment at Site 1 is shown in Figure 4.3. This segment is 87 m long and 95 m high with a standard deviation of 0.08 m, corresponding to a LOD of ± 0.16 m.

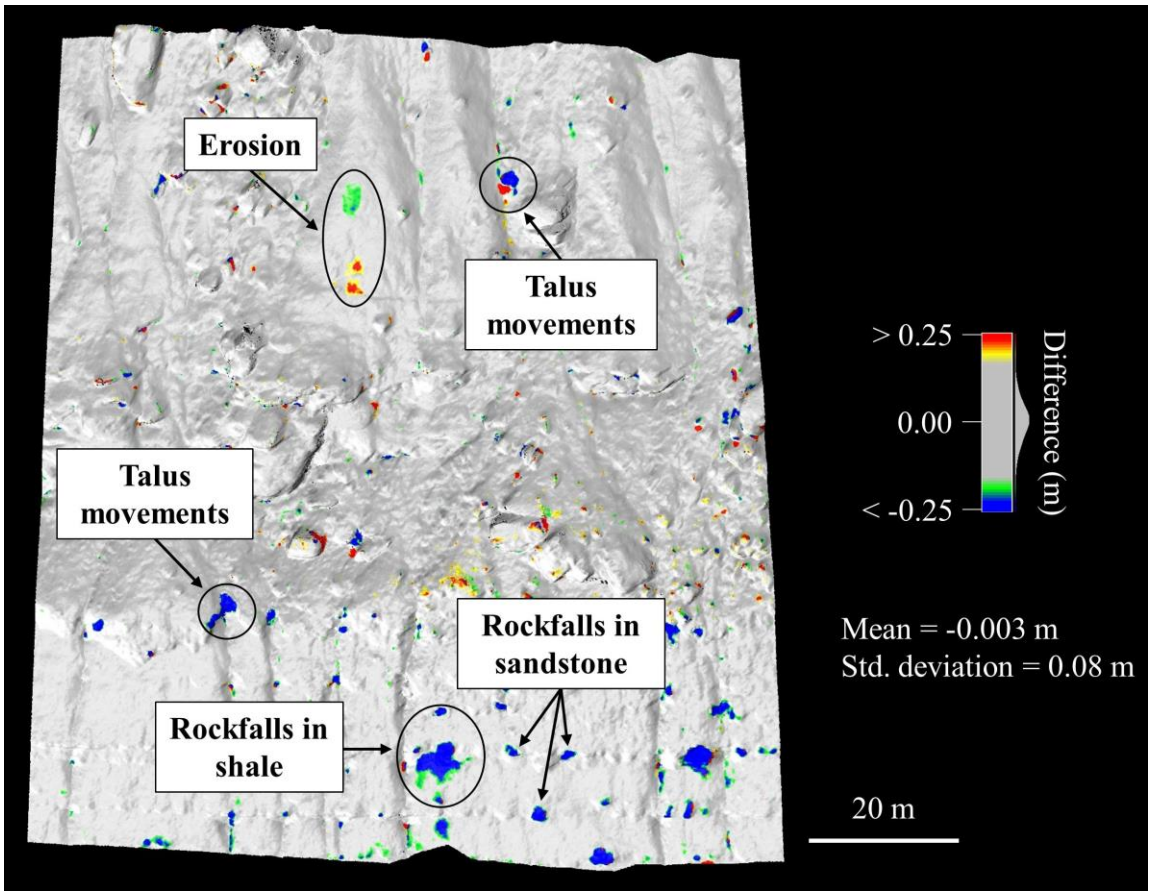

Figure 4.3 The M3C2 results for a representative segment at Site 1.

The change detection process revealed several types of changes at the site. These include detachment of rock fragments from the lower shale bed and the interbedded smaller sandstone beds. They also include movement of loose talus materials mixed with rock fragments that overlay the shale bed and erosion of surficial material. Changes are more concentrated along the lower part of the slope. This part is dominated by shale, thin sandstone layers, and talus material, compared to the upper part, which consists of thick sandstone beds. Notably, changes in shale layers are large with irregular boundaries, while in talus, they are slightly smaller. Changes in sandstone are much smaller, with well-defined boundaries according to the shape of the fallen rock.

The change detection at Site 1 between the first and last acquisition identified 119 rockfalls of varying sizes (Table 4.1). These rockfalls originated from the shale, talus, and sandstone layers.

The MCF curve (Figure 4.4A) demonstrates that the identified rockfall volumes span over three orders of magnitude from 1.0×10^{-2} m^3 to 7.8 m^3. The curve indicates that for volumes above a certain threshold, the data follow a power law distribution. This cutoff threshold, determined by the MLE method, is 2.1×10^{-1} m^3. Rockfall volumes below this cutoff were eliminated for further analysis, leaving 46 rockfalls, which are presented in the MCF curve in Figure 4.4B.

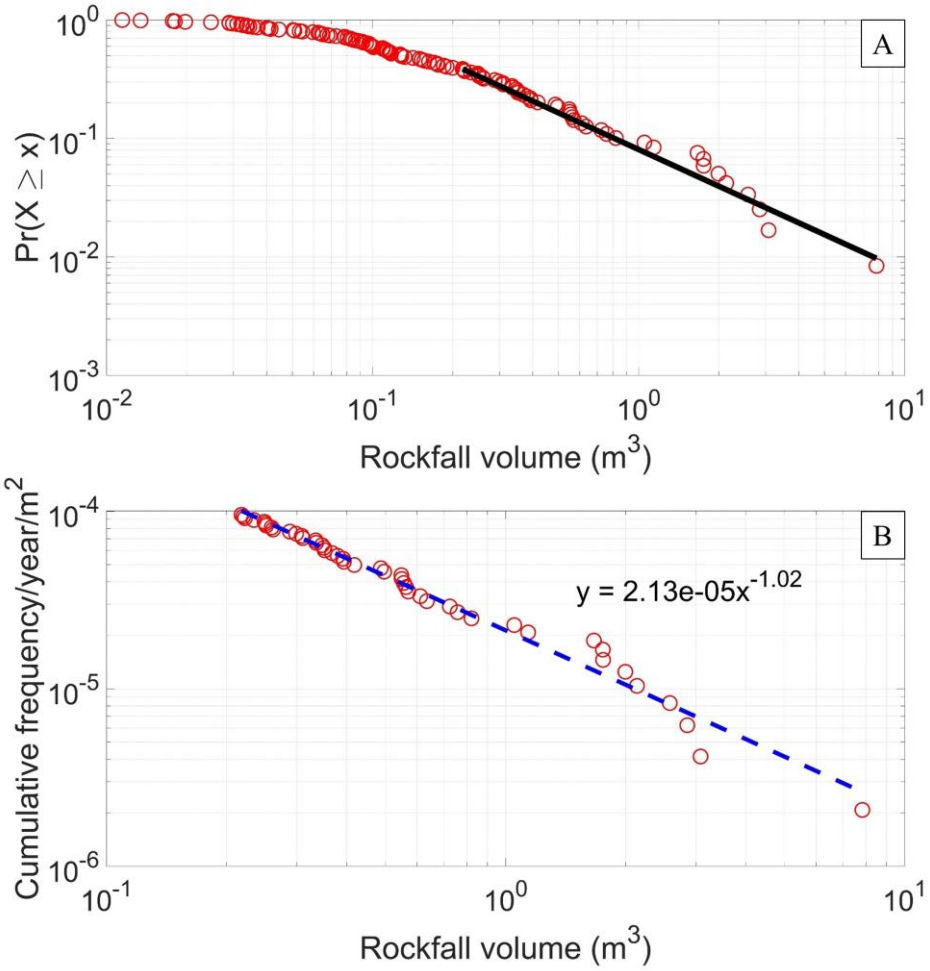

Figure 4.4 MCF curves for Site 1. A) Using MLE method to determine the cutoff volume. B) The MCF per year per m^2 for volumes > 2.1×10^{-1} m^3 at Site 1 using Ranking method and showing the power law fitting equation.

Table 4.1 Summary of the identified rockfalls at Site 1.

Rockfall source	Total rockfalls	Number of rockfalls > 2.1×10^{-1} m^3	Maximum volume (m^3)	Total volume (m^3) > 2.1×10^{-1} m^3
Shale	36	13	2.6	9.2
Talus	38	15	7.8	21.1
Sandstone	45	18	2.2	12.1

The spatial variability of rockfalls and associated volumes within Site 1 is highlighted in Figure 4.5. The variation in lithology at this site influences the occurrence of rockfalls and the distribution of volumes. Out of 46 rockfalls, 28 occurred in the lower portion of the slope. This portion is characterized by thick shale beds interbedded with thin competent sandstone beds (13 rockfalls) and covered by talus (15 rockfalls). The remaining 18 rockfalls were encountered in the upper jointed sandstone layer. Rockfalls in the lower part of the slope are primarily associated with various factors. These include detachments from the thin sandstone beds due to differential weathering, detachment of rockfalls from the weathered shale layer, and movement of talus material. Large rockfalls are concentrated at the boundary of rock-cut excavation. In the upper portion of the slope, rockfalls mainly originated from the detachment of blocks from sandstone beds.

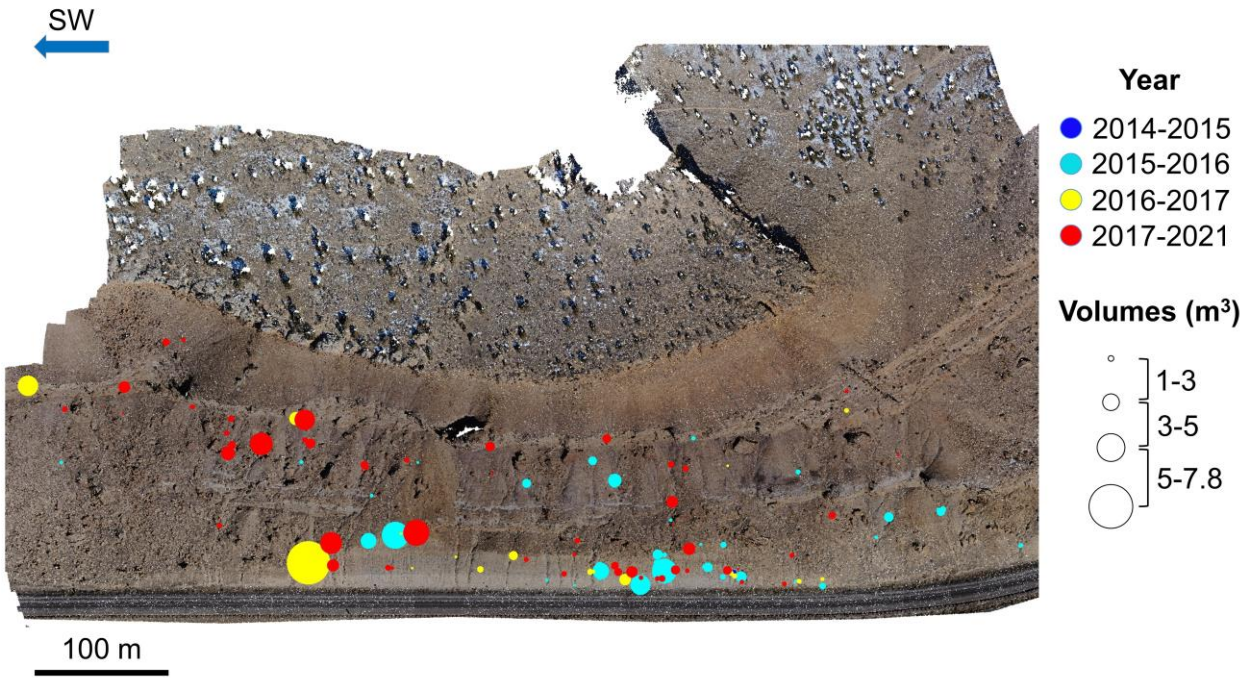

Figure 4.5 A top-down view of Site 1 showing the distribution of the 119 rockfalls. Circle sizes represent the relative rockfall volumes, while colors represent the acquisition year.

The maximum rockfall volumes observed in the shale layer, the talus, and in the upper sandstone are 2.6 m^3, 7.8 m^3, and 2.2 m^3, respectively. The total rockfall volumes are 9.2 m^3, 21.1 m^3, 12.1 m^3 in shale, talus, and sandstone, respectively. The largest rockfalls originated from the talus section, which is composed mainly of consolidated and compacted soil mixed with large rock fragments. On the other hand, rockfalls in sandstone were smaller and confined to dominant

of joints. The total volume of rockfall derived from talus is almost equivalent to the combined rockfall volumes in shale and sandstone. Initiation of rockfall along the lower section is attributed mainly to the excavation of cut-slopes along the road.

Figure 4.6 displays the MCF curves for three rockfall sources at Site 1 above the identified cutoff volume. It can be observed that the frequency of rockfalls in shale is higher than that of both sandstone and talus. Talus and sandstone exhibit similar frequencies for smaller rockfalls. However, as the volumes increase, the frequency of rockfalls in the sandstone section decreases compared to talus, with the largest volumes being observed in the talus.

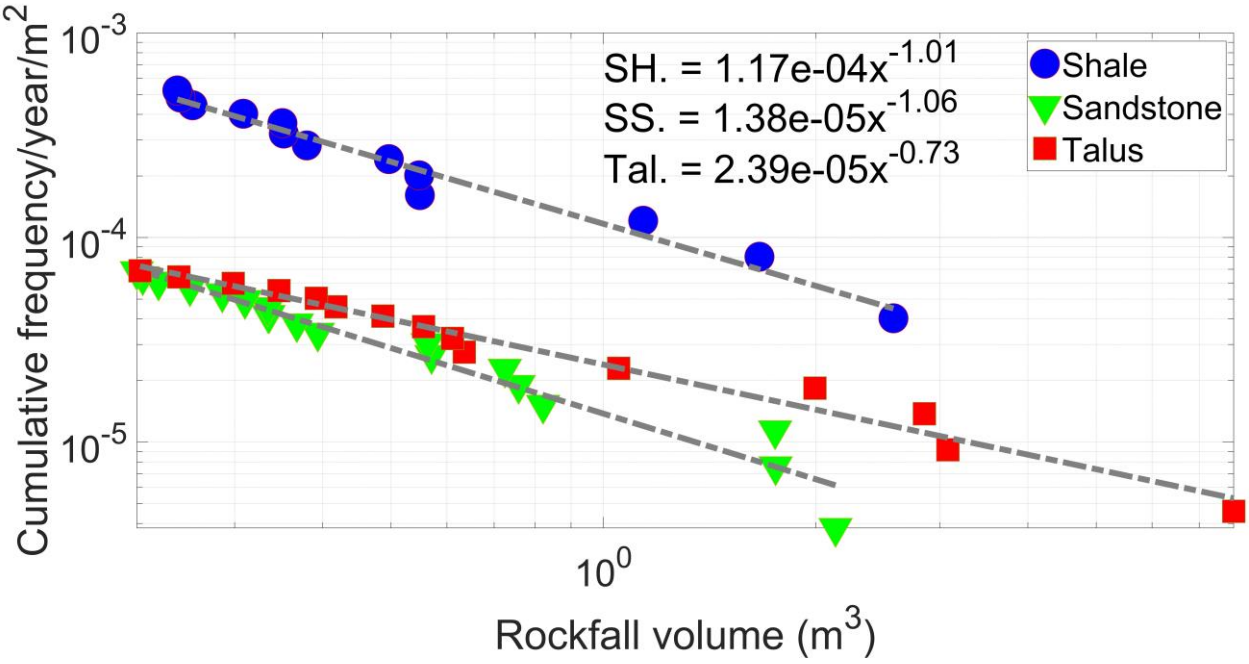

Figure 4.6 MCF curves for the rockfall sources at Site 1 for volumes > 2.1×10^{-1} m^3. Note that frequencies are normalized by the areas of each rockfall source (rather than the full slope area).

The structural mapping of 80 m long and 150 m high selected segment from Site 1 identified 76 discontinuities (Figure 4.7), classified as joints and bedding planes. The bedding planes are sub-horizontal and persistent, while the joint planes are less persistent, varying in dip from horizontal to near vertical. The stereographic projection of the obtained structural data revealed the existence of three joint sets along the sub-vertical slope face, which dips towards the south (83/178). The first joint set (J1, 73/178) strikes sub-parallel to the slope face with a steep dip angle. The second joint set (J2, 80/229) strikes oblique to the slope face with a sub-vertical dip angle. The third joint set (J3, 02/042) is sub-horizontal and dips toward the northeast.

Rock blocks that have detached along these three joint sets can be identified from the scars on the sandstone ledges (Figure 4.8). Erosion of the small shale layers, which are interbedded with the sandstone, has led to the formation of several overhanging blocks. These blocks can fall along the encountered joint sets and through intact rock failures (rock bridges). The sub-vertical joint set (J1) provides a potential release surface for sliding, while the oblique joint set (J2) forms potential lateral release surfaces for the detached blocks. The sub-horizontal joint set (J3) creates the upper release surface for the overhanging blocks. The distribution of joint spacing is shown in Figure 4.9.

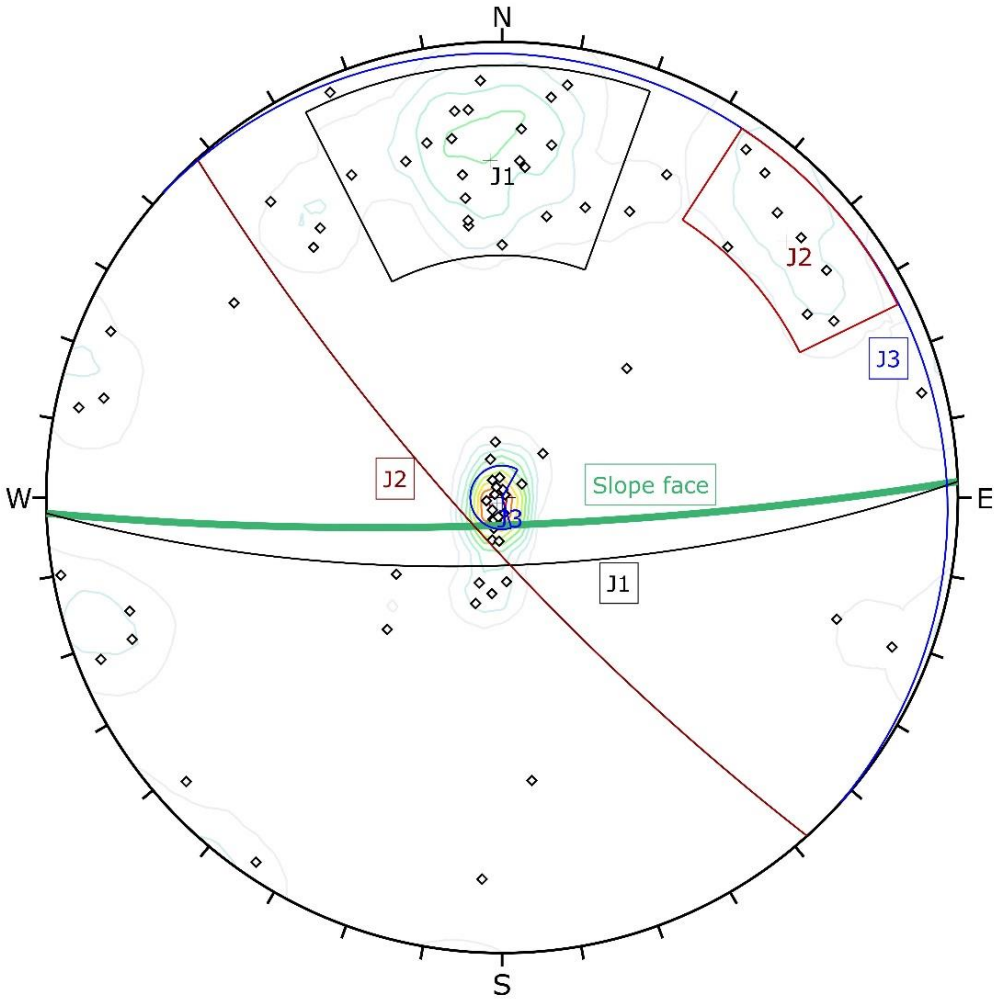

Figure 4.7 Stereographic projection for the mapped structures at Site 1.

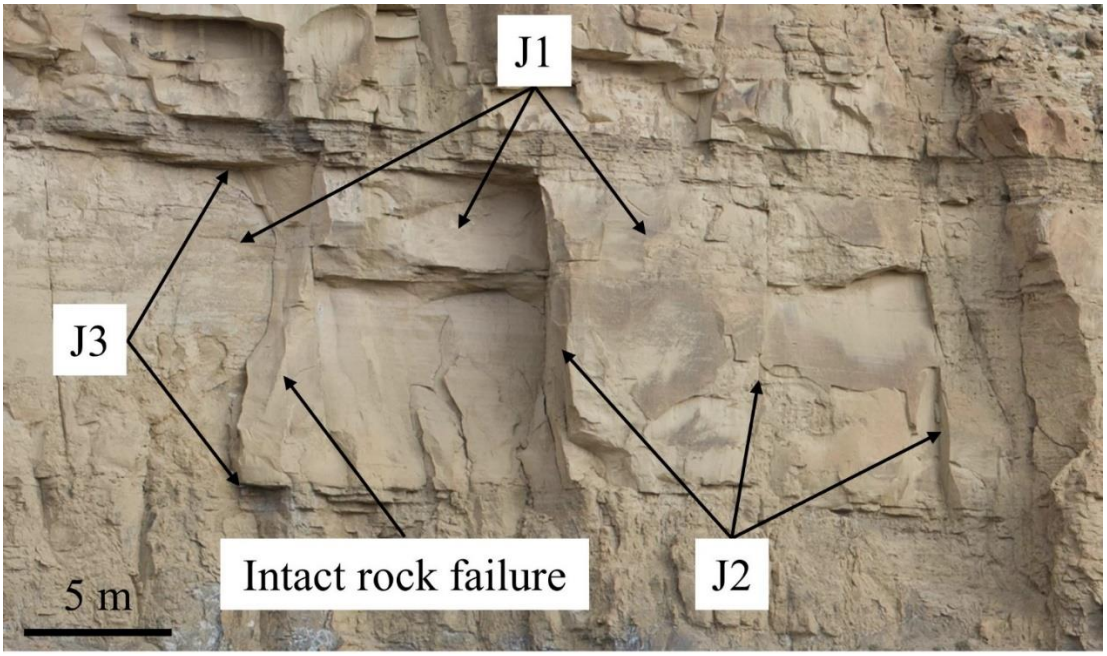

Figure 4.8 Detachment of blocks along the identified joint sets at Site 1.

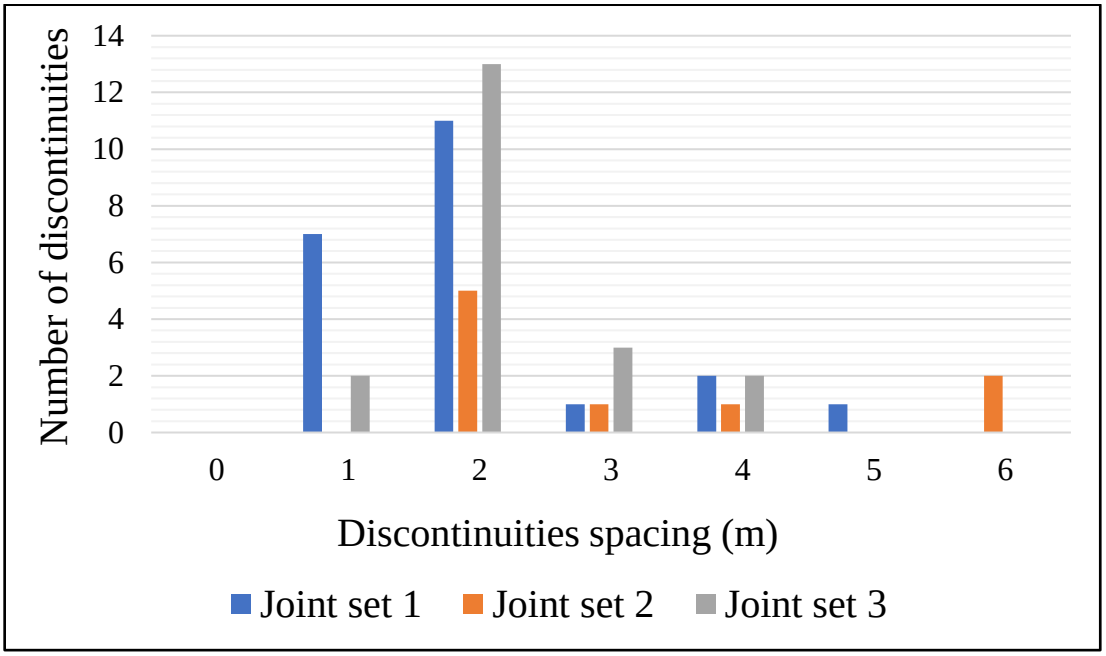

Figure 4.9 Distribution of discontinuity spacing by joint set at Site 1. The spacing values are binned to the nearest highest number.

Based on Monte Carlo simulation using the obtained spacing data, the expected range of block volumes is between 9.8×10^{-1} m^3 to 32.9 m^3. This is larger than the detected rockfall volumes in sandstone, which ranged from 1.1×10^{-2} m^3 to 2.2 m^3 (Figure 4.10). The difference

between the ranges of the expected block volumes and detected rockfall volumes could be attributed to the following:

1. Mapping structures from the point cloud relies on detecting clear traces of discontinuities to measure their orientation and spacing. The lower resolution of the point cloud can lead to relatively small and low aperture joints being missed during mapping, resulting in larger expected block volumes. This issue is evident in the mapping of J3. The smallest features shown in Figure 4.8 were not mapped in the point cloud, causing a larger apparent spacing of J3 compared to the actual spacing.
2. The predominant occurrence of intact rock failures along rock bridges in the sandstone likely contributes to the formation of rockfalls that are smaller than the joint-bounded block sizes.

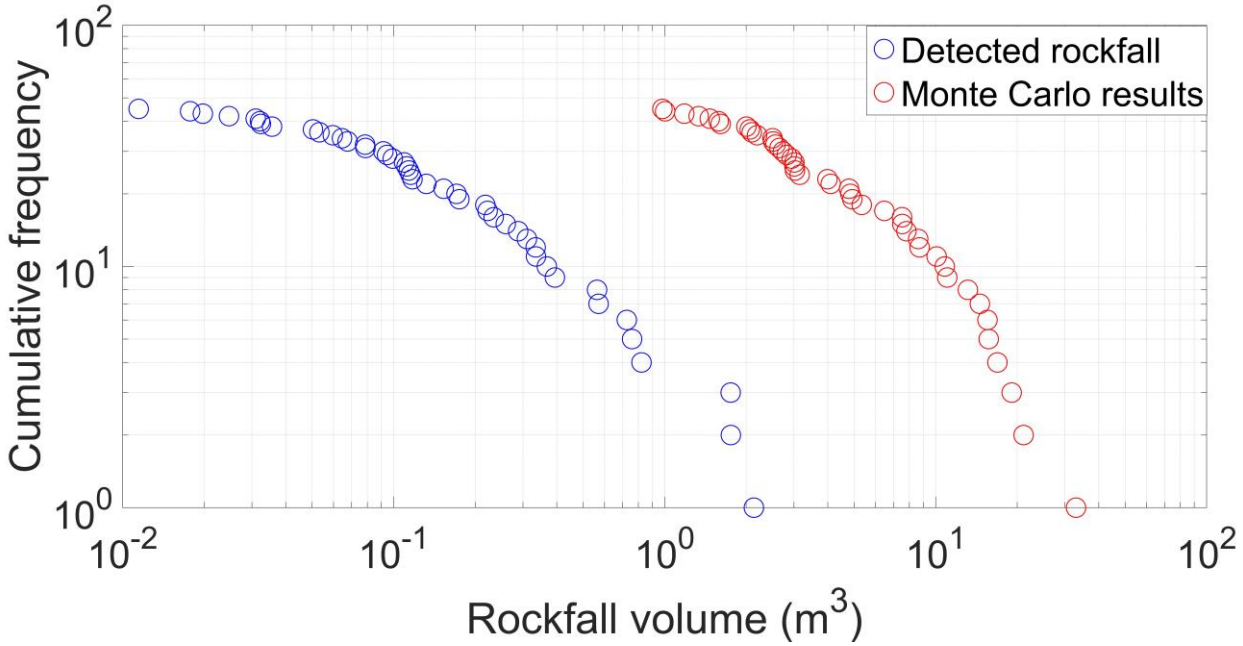

Figure 4.10 A comparison between the MCF curves of the identified rockfalls and the Monte Carlo fracture-bounded block size simulation results at Site 1.

The examination of rockfall shapes identified within the sandstone layers showed that they fall into three main shape categories: bladed, very bladed, and very elongate (Figure 4.11). The distribution of joint sets spacing has a noticeable impact on these shapes. The narrow spacing of J1 contributes to the bladed shapes of rockfalls. These shapes shift to very bladed when the J1 spacing decreases or very elongate when the J3 spacing decreases.

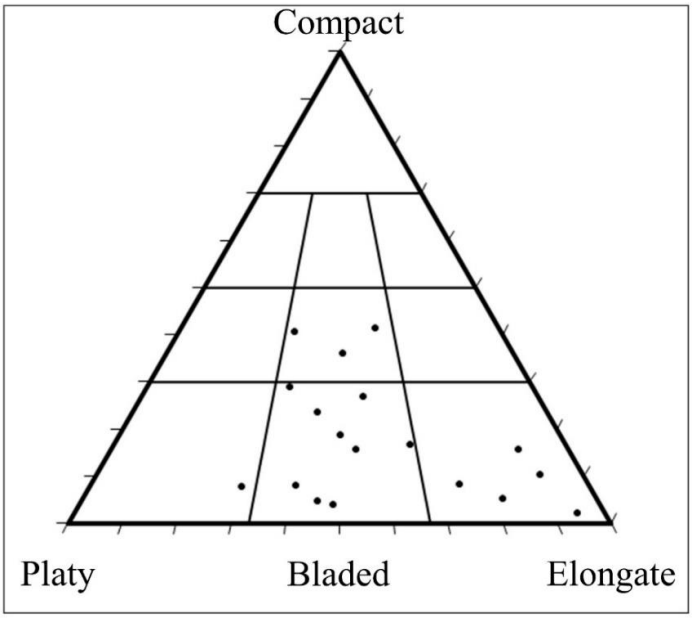

Figure 4.11 The identified rockfall shapes for the detected rockfalls in sandstone at Site 1 corresponding to volumes > 2.1×10^{-1} m^3.

4.2 Site 2

An example photogrammetric model for Site 2 is shown in Figure 4.12. The dense point cloud for 2014 has 69,209,033 points, while the 2021 cloud has 39,299,221 points. The point spacing along the slope segments has an average of 0.07 m. Figure 4.13 shows a representative M3C2 result for a 68 m long and 75 m high segment at Site 2. The standard deviation for this segment is 0.11 m, corresponding to a LOD of ± 0.22 m. Following a review of the M3C2 change results, it was determined that manual vegetation removal along this site was not optimal. This left some small unfiltered vegetated areas, which increased the standard deviation compared to Site 1.

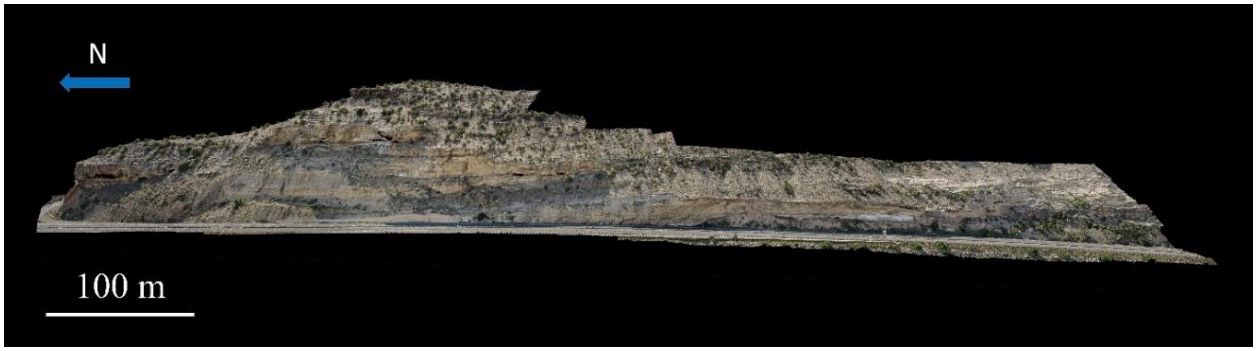

Figure 4.12 Example of the produced photogrammetric models (2021) for Site 2.

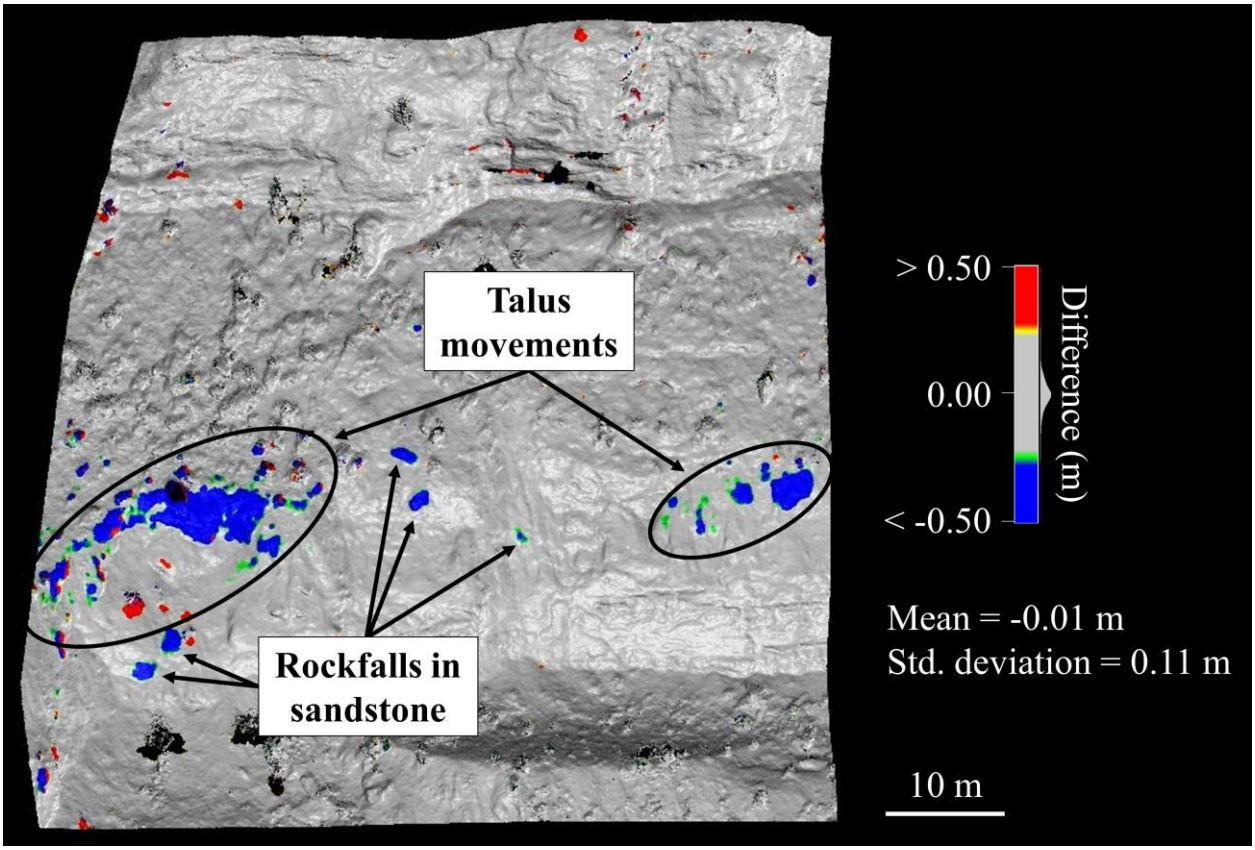

Figure 4.13 The M3C2 results for a representative segment at Site 2.

The change detection process revealed several types of changes at the slope. These changes include rock detachments from the sandstone beds, movements of talus, and erosion of surficial weathered material, in addition to changes related to unfiltered vegetation. Changes occurred mainly in two parts of the slope. These include the talus materials that overlay sandstone beds at the northern part and, to a lesser extent, the massive sandstone beds along the southern part of the slope. Changes in the talus materials exhibit irregular shapes, whereas in sandstone, the change regions tend to be smaller with well-developed sharp boundaries.

The change detection process at Site 2 between the 2014 and 2021 acquisition identified 126 rockfalls (Table 4.2). These rockfalls originated from the talus and sandstone layers. The identified rockfall volumes span six orders of magnitude from 3×10^{-4} m^3 to 13.5 m^3 (Figure 4.14A). The cutoff volume obtained using the MLE method is 2.0×10^{-2} m^3. The number of observed rockfalls larger than the cutoff volume is 89 rockfalls (Figure 4.14B).

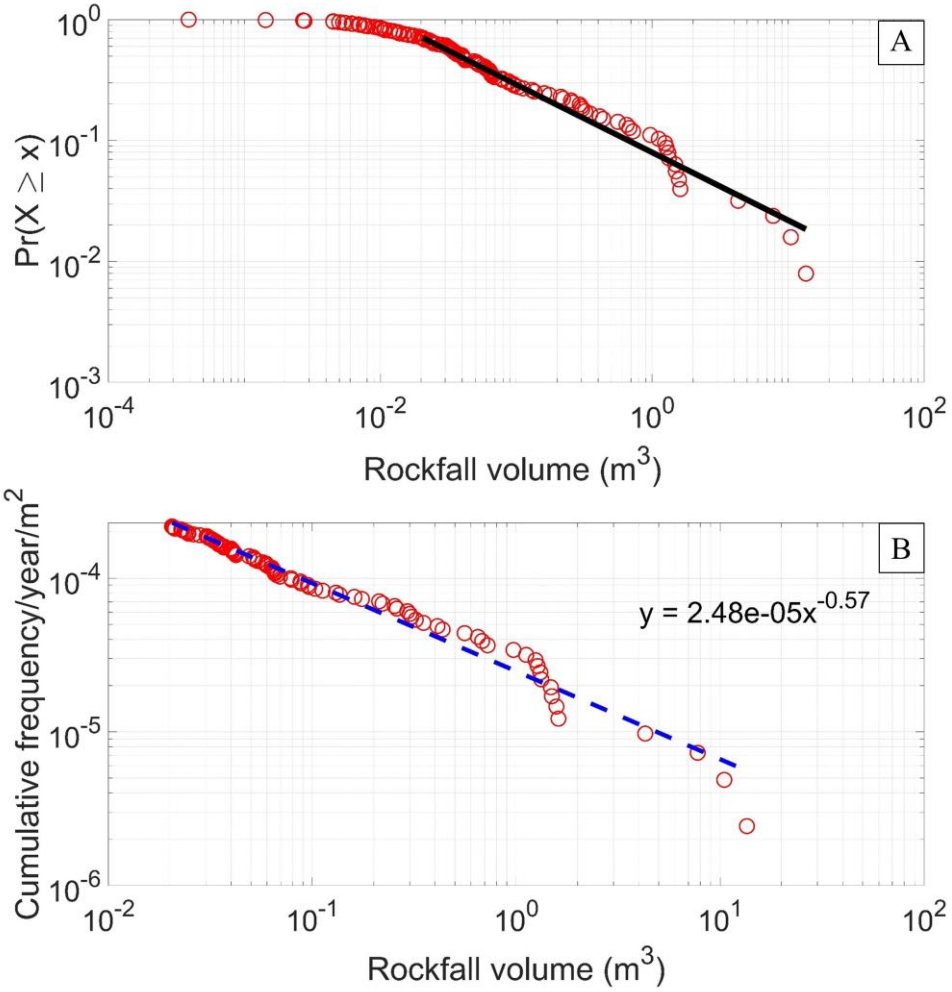

Figure 4.14 MCF curves for Site 2. A) Using the MLE method to determine the cutoff volume. B) The MCF per year per m^2 at Site 2 using the Ranking method and showing the power law fitting equation for volumes > 2.0×10^{-2} m^3.

Table 4.2 Summary of the identified rockfalls at Site 2.

Rockfall source	Total rockfalls	Number of rockfalls > 2.0×10^{-2} m^3	Maximum volume (m^3)	Total volume (m^3) > 2.0×10^{-2} m^3
Sandstone	52	41	13.5	46.4
Talus	74	48	4.3	12.4

The spatial variability of rockfalls and associated volumes within Site 2 is highlighted in Figure 4.15. The variation of exposed materials along the site has a notable impact on the rockfall occurrences and distribution of volumes. Out of 89 rockfalls, 41 occurred in the massive sandstone with a maximum volume of 13.5 m^3, distributed along the site. In the talus, 48

rockfalls were observed with a maximum volume of 4.3 m^3, concentrated in the high northern section of the slope. The presence of steep slip surface, resulting from the landslide in the northern section, also contributed to the initiation of numerous rockfalls. The total recorded rockfall volumes at Site 2 are 46.4 m^3 in the sandstone and 12.4 m^3 in the talus section. The majority of rockfalls in the talus sections are composed of equal-sized small boulders. The rockfalls in the massive sandstone are influenced mainly by two discontinuity sets. These are the horizontal bedding and the sub-vertical joints parallel to the slope face with large spacing, which form large overhanging blocks. (Figure 4.16).

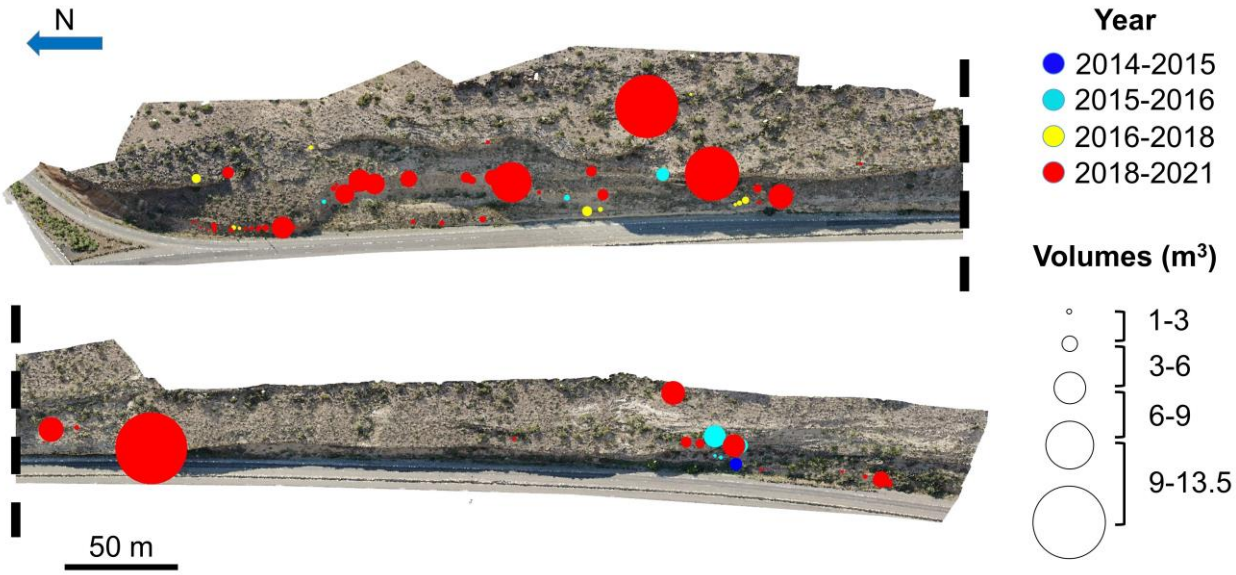

Figure 4.15 The spatial and temporal distribution of the detected 126 rockfalls at Site 2. Circle sizes represent the relative rockfall volumes, while colors represent the acquisition year.

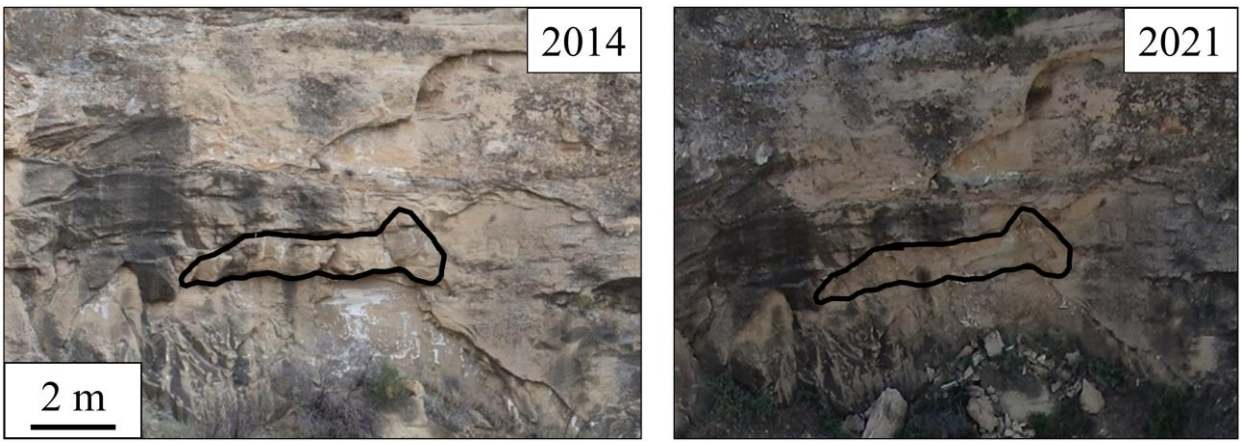

Figure 4.16 The exposed sandstone at the southern section of the slope forming large overhangs along the sub-vertical joints.

Figure 4.17 illustrates the MCF curves for rockfall sources (Talus and Sandstone) above the cutoff volume. The data indicates that rockfalls from Talus exhibit an overall higher frequency compared to those from sandstone. As the volume decreases, the frequency of rockfalls from talus progressively increases, and the difference in frequency between talus and sandstone becomes more pronounced for the smallest volumes. Moreover, the largest volumes are observed in sandstone.

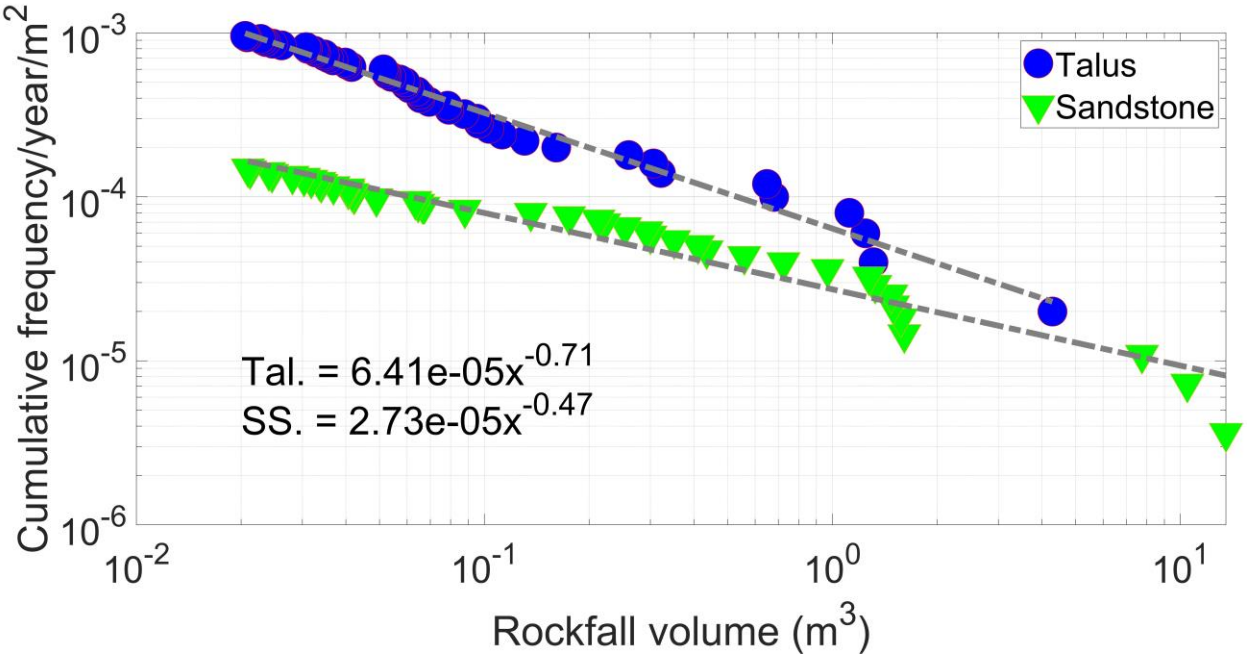

Figure 4.17 MCF curves for the rockfall sources at Site 2 for volumes > 2.0×10^{-2} m^3. Note that frequencies are normalized by the areas of each rockfall source (rather than the full slope area).

The analysis of rockfall shapes within the sandstone beds revealed a high degree of variability in their morphology, with a slight concentration in the very bladed shape category (Figure 4.18). These rockfalls span across nine of the ten categories defined by Sneed's classification, which indicates the wide variety of shapes present in this site. This diversity in rockfall shapes can be attributed to the prevailing massive sandstone. The sandstone exhibits a limited number of prominent pre-existing structural features, such as joints and bedding planes. The absence of well-defined structures contributes to the heterogeneity in the rockfall shapes observed along the slope.

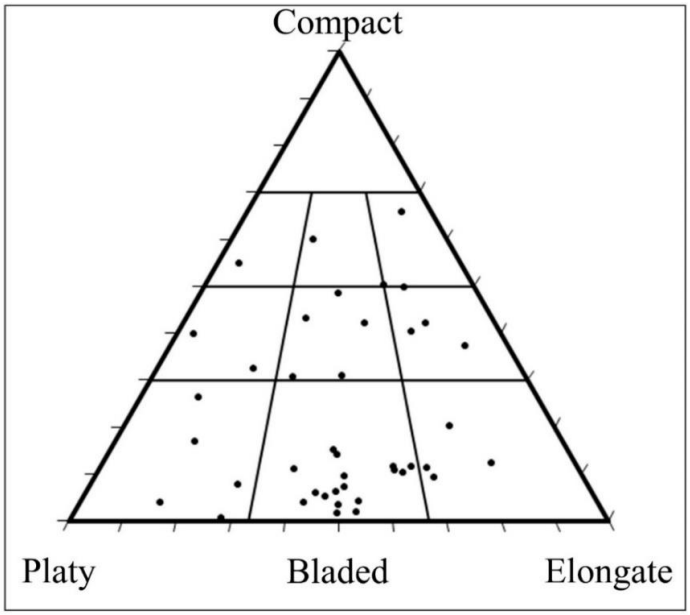

Figure 4.18 The identified rockfall shapes for the detected rockfalls in sandstone at Site 2 corresponding to volumes > 2.0×10^{-2} m^3.

4.3 Site 3

An example photogrammetric model for Site 3 is shown in Figure 4.19. The densified point cloud from 2014 acquisition has 149,681,036 points, while the 2021 cloud has 354,156,881 points. The point spacing for the models of this slope is similar to that of Site 2, with an average of 0.07 m. The precision of direct geo-referencing at Site 3 was assessed similar to Site 1, where three photogrammetric segments from the 2021 acquisition were compared to the lidar scan. An example segment is shown in Figure 4.20. The resulting RMS difference metric at this site was found to vary from 0.09 to 0.12 m. This indicates slightly poorer accuracy than what was obtained at Site 1. This increase could be attributed to the relatively poor quality of the lidar point cloud compared to Site 1, as seen in Figure 4.21. Additionally, it could be due to the presence of vegetation missed during manual filtering.

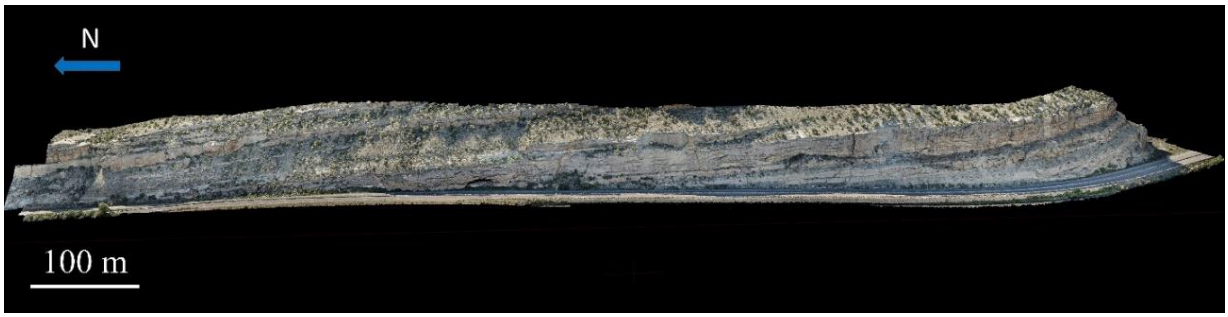

Figure 4.19 Example of the produced photogrammetric models (2021) at Site 3.

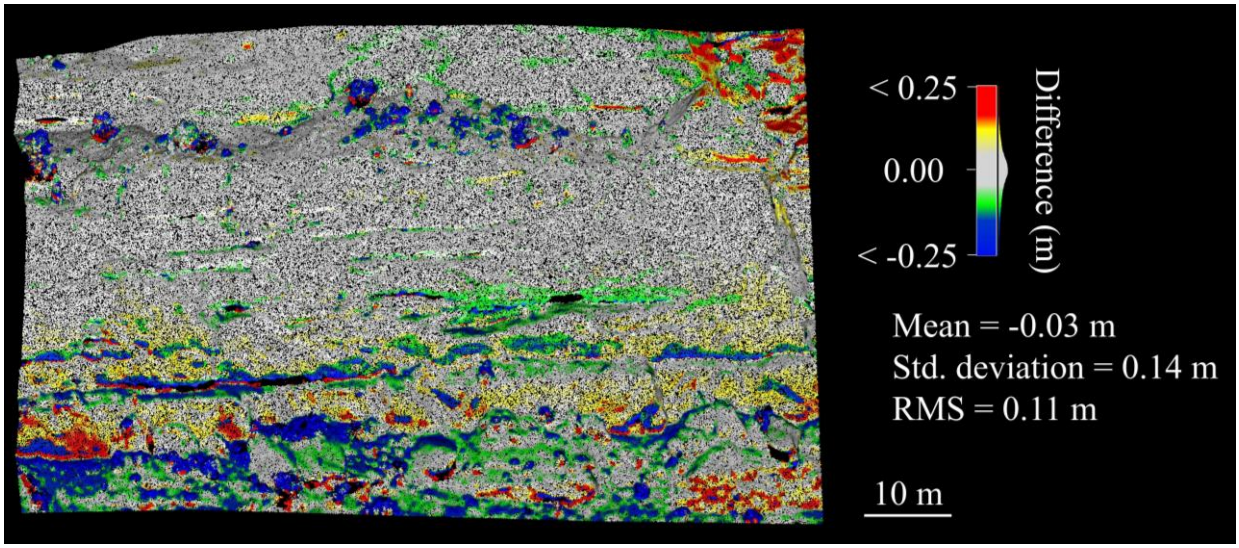

Figure 4.20 The M3C2 differences between a representative photogrammetric segment and a lidar survey at Site 3. Some change below the limit of detection is shown to more clearly illustrate the subtle distortion effects present.

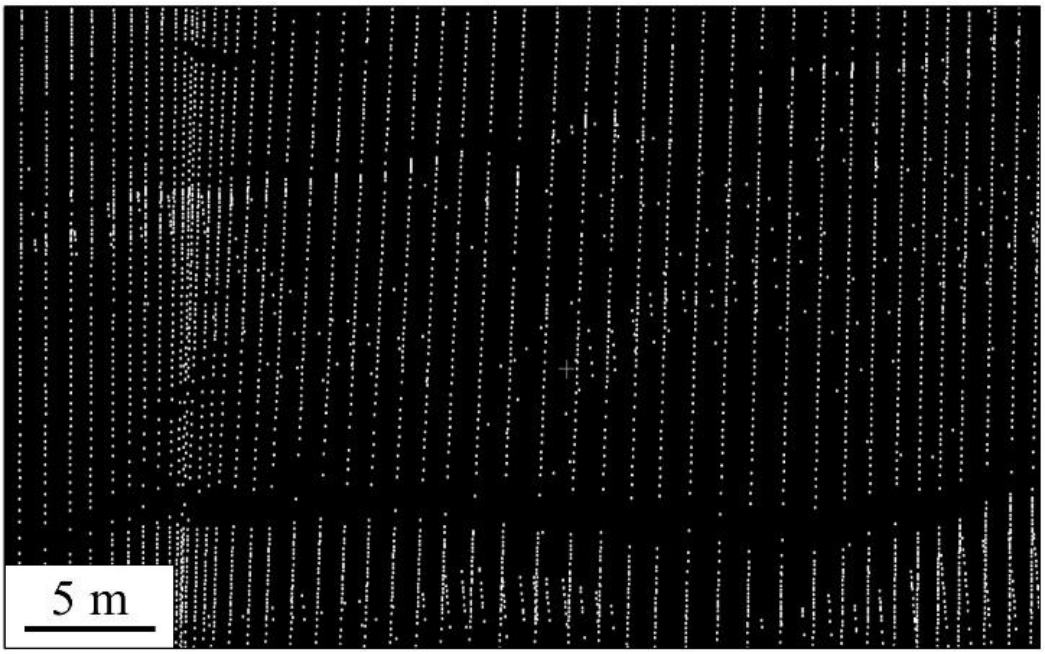

Figure 4.21 A) The poor quality of lidar point cloud due to up to 1.4 m gaps between vertically aligned points.

A representative change detection result for a 62 m long and 50 m high segment from Site 3 is shown in Figure 4.22. It has a standard deviation of 0.11 m, corresponding to a LOD of ± 0.22 m. As in the case of Site 2, manual vegetation removal at Site 3 was imperfect, which increased the

standard deviation. The observed changes on the rock slope were primarily associated with the prevailing sandstone beds.

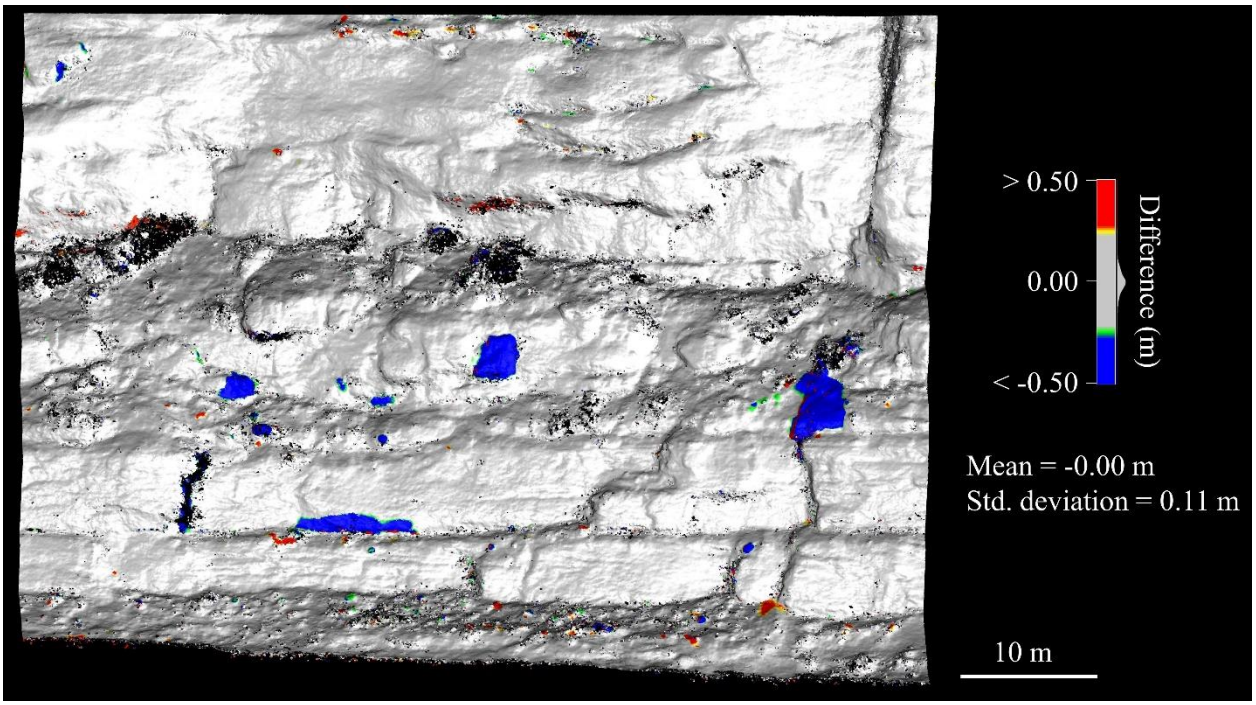

Figure 4.22 The M3C2 results for a representative segment at Site 3.

The change detection process between the first and last acquisition identified 210 rockfalls (Table 4.3). These rockfalls originated from the exposed sandstone beds. The identified rockfall volumes span over six orders of magnitudes from 4×10^{-4} m^3 to 23.1 m^3 (Figure 4.23A). The detected cutoff volume using the MLE method is 2.9×10^{-1} m^3 and the number of observed rockfalls larger than this threshold is 31 (Figure 4.23B).

Table 4.3 Summary of the identified rockfalls at Site 3.

Rockfall source	Total rockfalls	No. of rockfalls > 2.9×10^{-1} m^3	Maximum volume (m^3)	Total volume (m^3) > 2.9×10^{-1} m^3
Sandstone	210	31	23.1	75.1

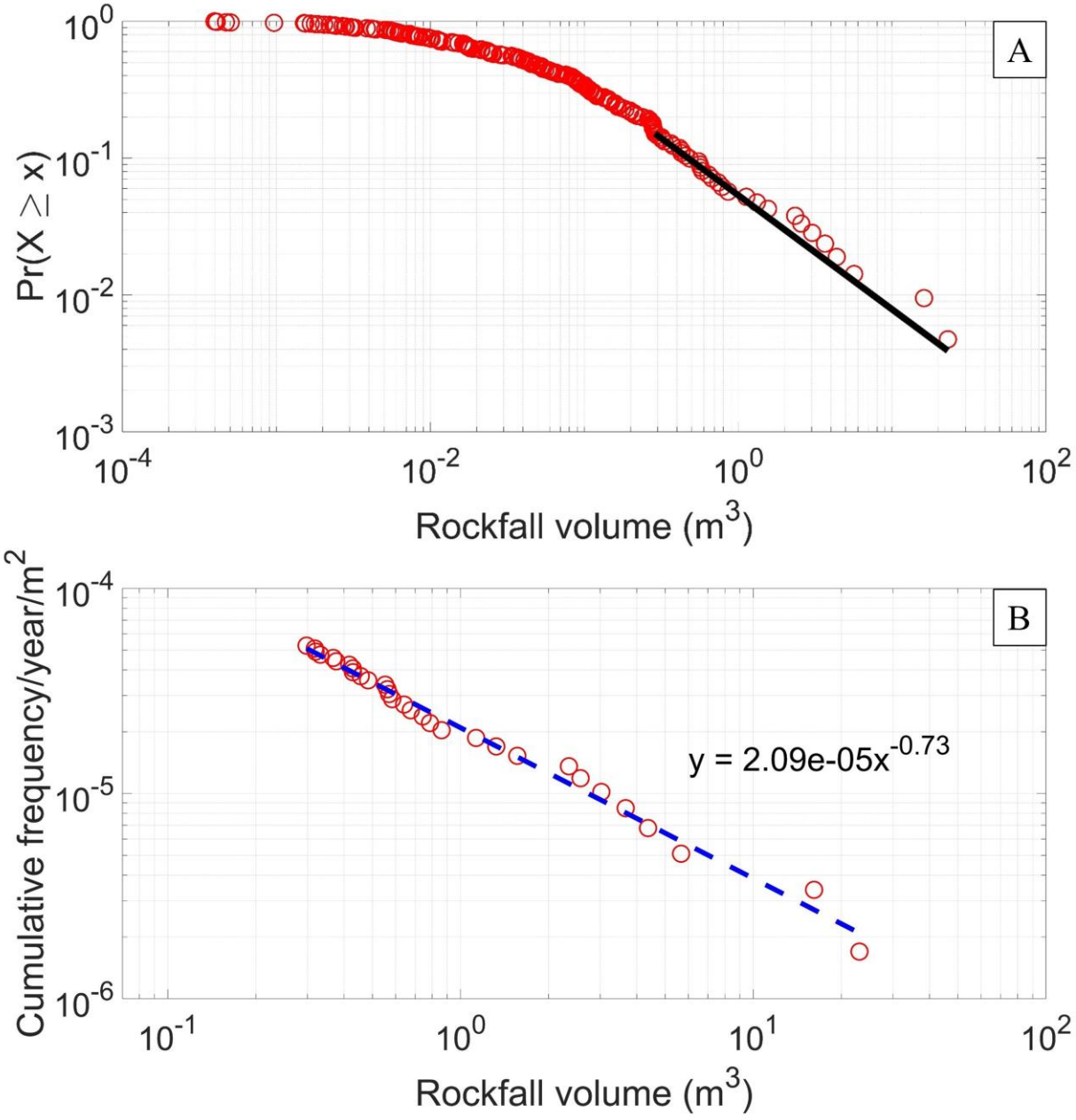

Figure 4.23 MCF curves for Site 3. A) Using the MLE method to determine the cutoff volume. B) The MCF per year per m^2 at Site 3 for volumes > 2.9×10^{-1} m^3 using Ranking method and showing the power law fitting equation.

The lithology variation at Site 3 is limited compared to the other sites. Sandstone beds are exposed along the whole site with limited occurrences of thin talus. However, the spatial distribution of rockfall volumes displayed in Figure 4.24 shows a concentration of the rockfalls along the southern section of the slope. This indicates that other factors control the rockfall occurrences along this site.

Figure 4.24 The spatial and temporal distribution of the detected 210 rockfalls at Site 3. Circle sizes represent the relative rockfall volumes, while colors represent the acquisition year.

The structural mapping of a 62 m long and 50 m high segment from Site 3 identified 86 discontinuities (Figure 4.25), classified as joints and bedding planes. The bedding planes are persistent and primarily horizontal, while the joint planes are less persistent and vary in dip from horizontal to near vertical. The distribution of joint spacing is shown in Figure 4.26. The stereographic projection of the obtained structural data revealed the existence of three joint sets along the sub-vertical slope face (79/312). The joint set (J1, 75/309) and (J2, 19/310) strikes sub-parallel to the slope face. Despite the similar strikes for J1 and J2, it was noted that J1 has a steeper dip angle. J2 is sub-parallel to the slope face with a gentle dip angle and different persistence, such that it was identified as a different joint set. The third joint set (J3, 76/360), strikes at a relatively oblique angle to the slope face. Detachment of overhanging rocks along steep joint surfaces and toppling along surfaces dipping into the rock face can be observed along the slope (Figure 4.27).

The slope angle along this site varies from 38° in the northern section to nearly vertical in the southern section (Figure 4.28). In the northern section, the slope angle is shallower (38°), which is less than the steep dip angle of J1 (75°), causing J1 to no longer be exposed. In contrast, in the southern section, where slope angle becomes steeper, J1 is exposed, resulting in an increase in rockfall rates towards the south.

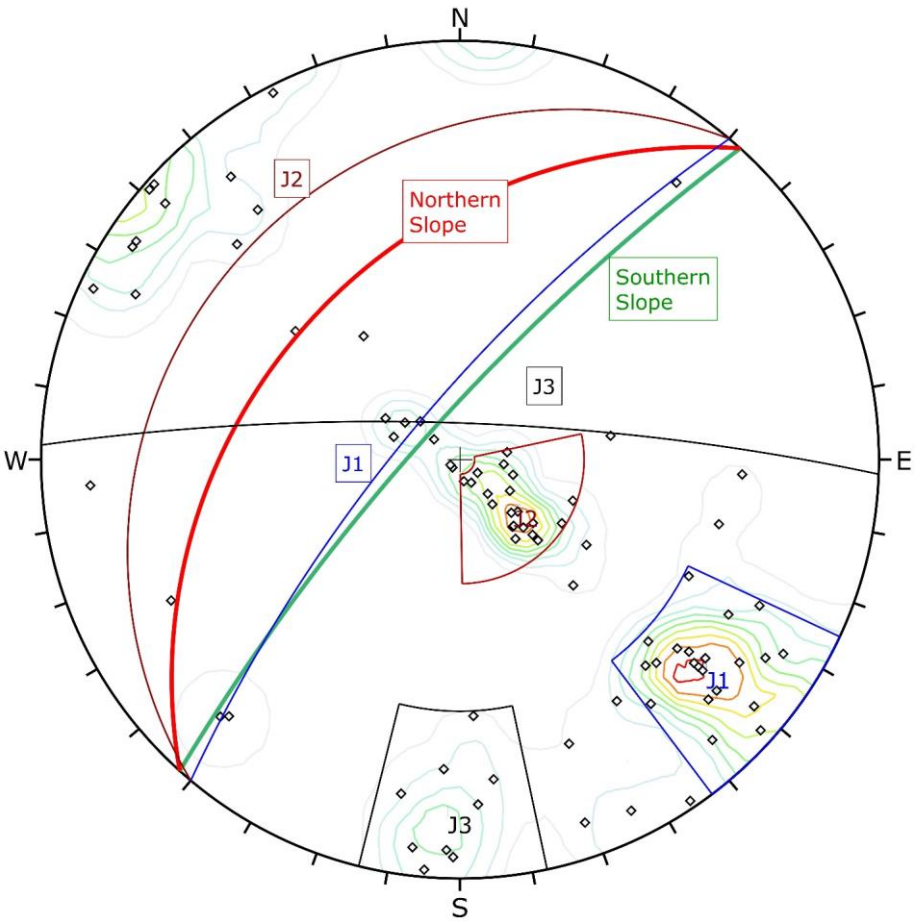

Figure 4.25 Stereographic Projection for the mapped structures at Site 3.

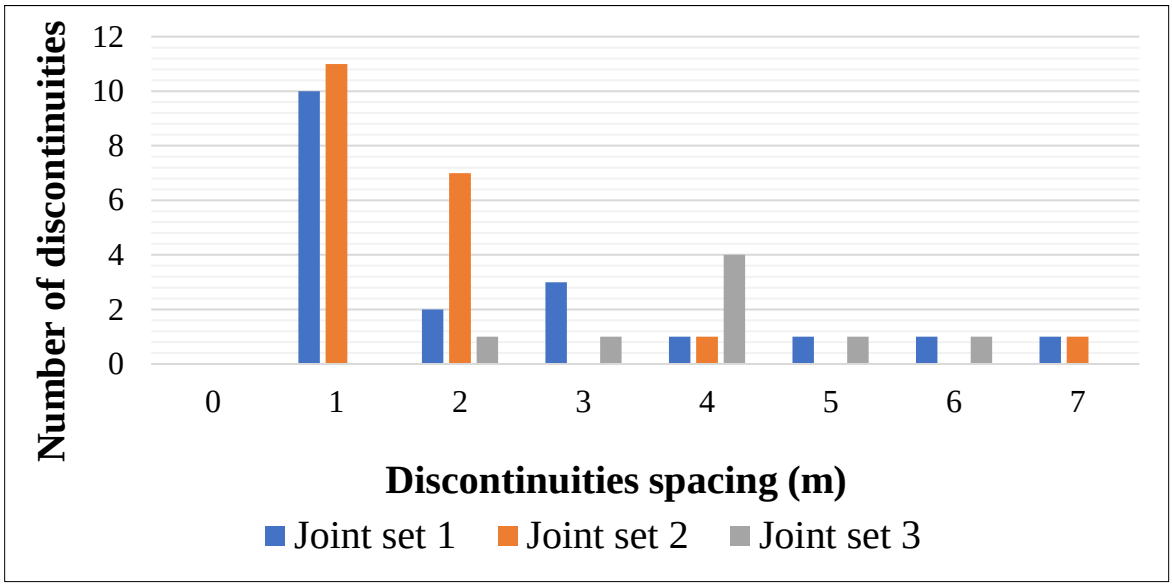

Figure 4.26 Distribution of discontinuity spacing by joint set at Site 3. The spacing values are binned to the nearest highest number.

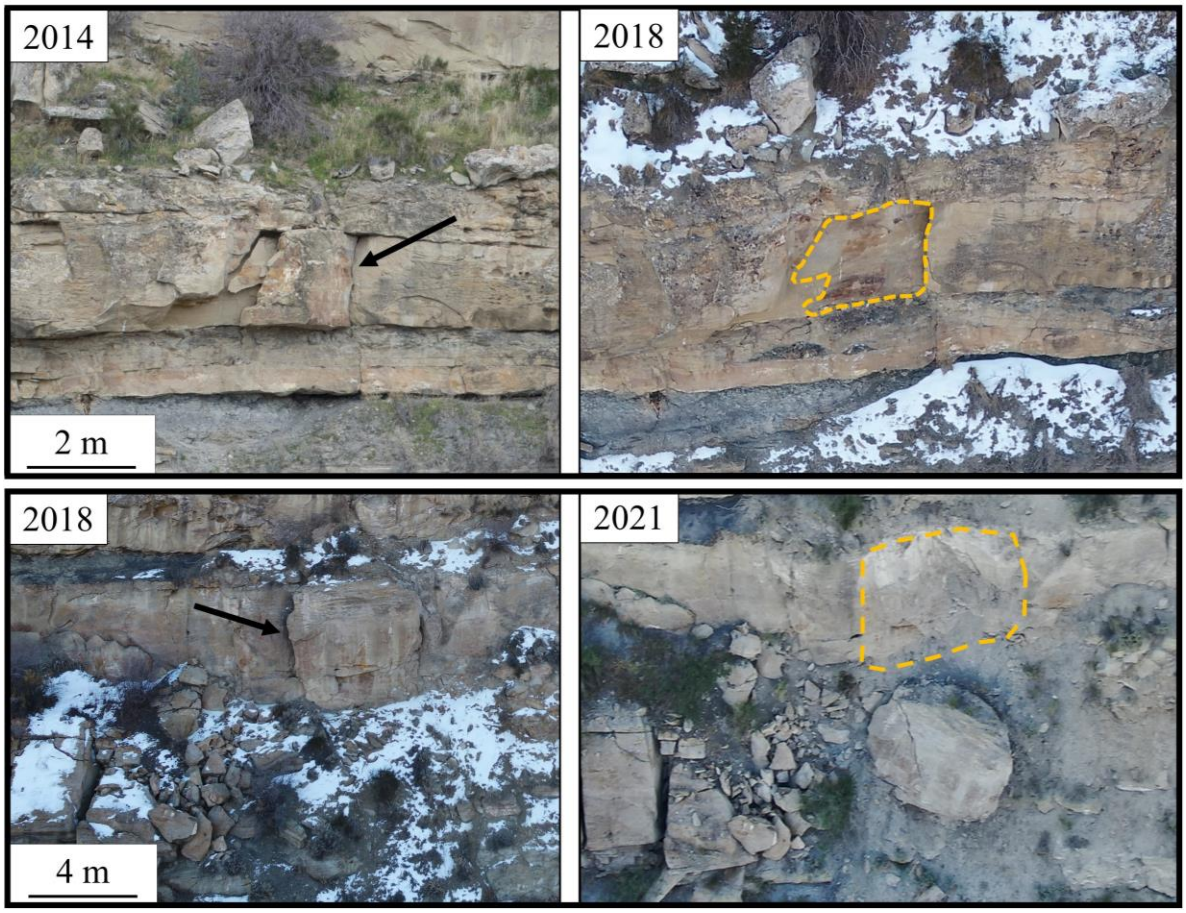

Figure 4.27 Example of detached hanging blocks (top) and toppling failure (bottom) at Site 3.

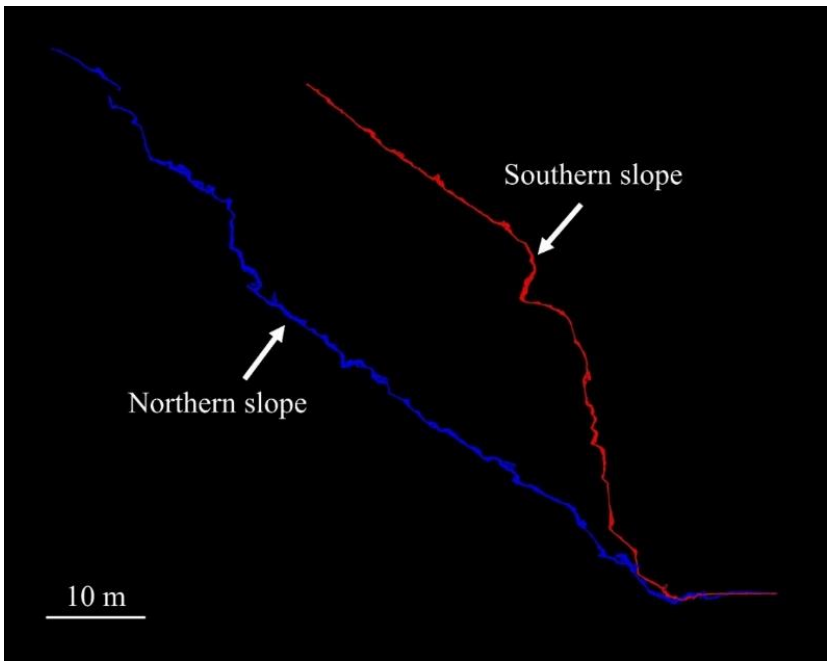

Figure 4.28 Comparison between two cross-sections from the northern and southern slope portions of Site 3.

Based on Monte Carlo simulation for the obtained spacing, the expected range of block volumes is between 4.9×10^{-1} m^3 to 173.2 m^3. This is larger than the observed rockfall volumes in sandstone that ranged from 4×10^{-4} m^3 to 23.1 m^3 (Figure 4.29). The factors influencing the difference between the expected block volumes and detected rockfall volumes are interpreted to be similar to those at Site 1. Additionally, the existence of rockfalls that were not necessarily fully bounded by joint sets might also contribute to these differences. The geometry of such rockfalls could be controlled by other factors, such as weathering or overhanging, rather than the presence of joints (Figure 4.30).

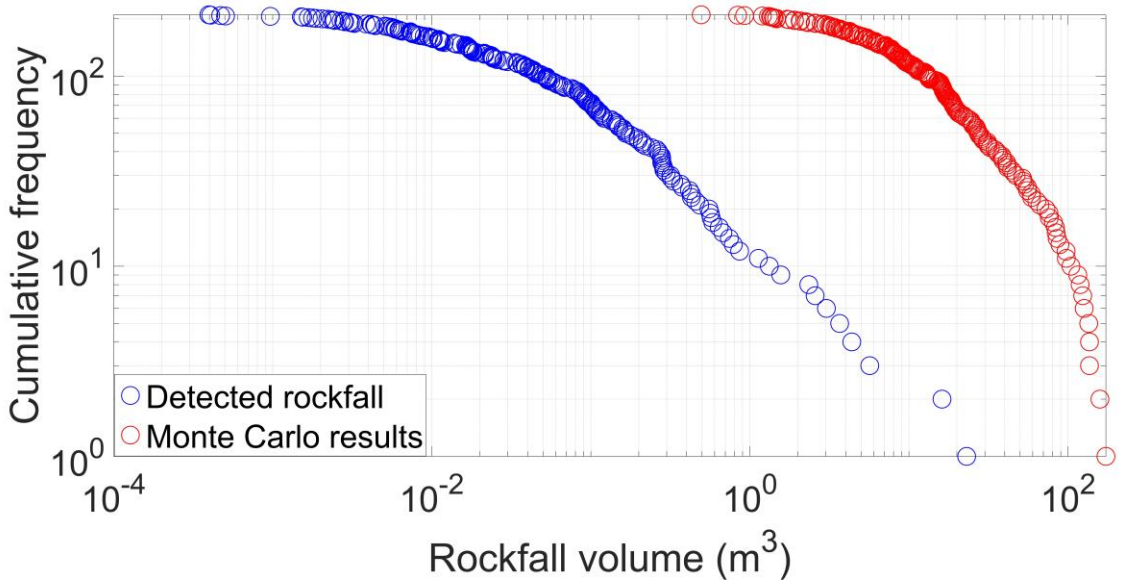

Figure 4.29 A comparison between the MCF curves of the identified rockfalls and the Monte Carlo fracture-bounded block size simulation results at Site 3.

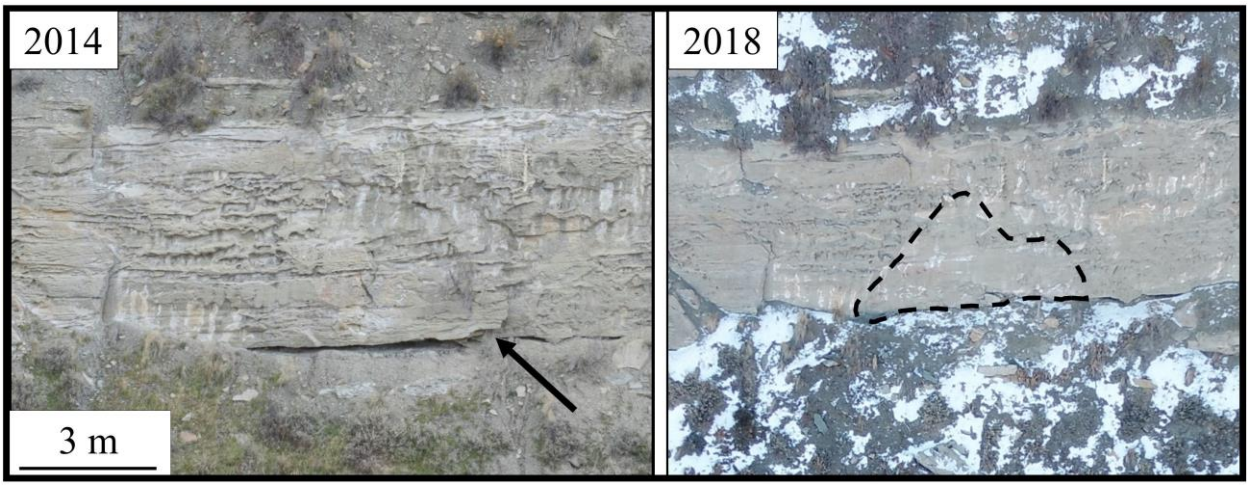

Figure 4.30 Example for a fallen rockfall that is not fully bounded by joint sets.

The examination of rockfall shapes along this site revealed similarities to those found at Site 1. The rockfall shapes are primarily concentrated in the very bladed and very elongate categories, with limited rockfalls having bladed, platy, and very platy shapes (Figure 4.31). The distribution of rockfall shapes is affected by the joint sets spacing. The narrow spacing of J1 contributes to the bladed and very bladed shapes of rockfalls, which can shift to very elongate shapes when J2 spacing decreases locally.

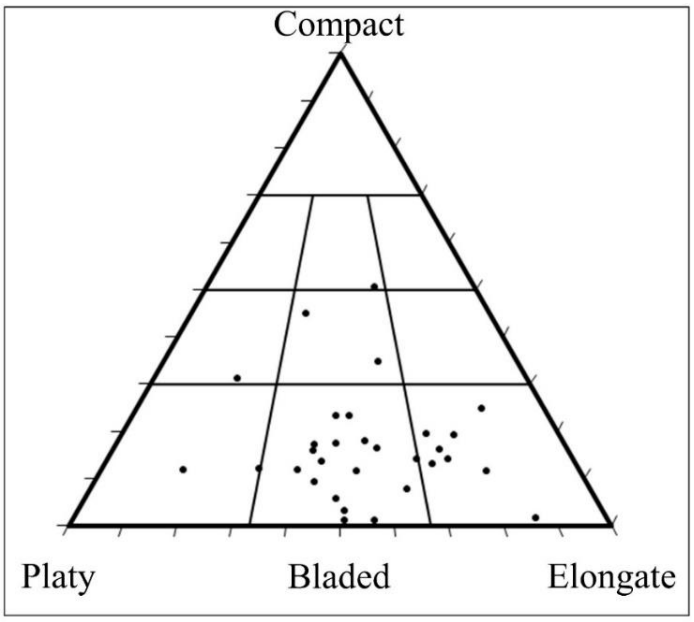

Figure 4.31 The identified rockfall shapes for the detected rockfalls in the sandstone layer at Site 3 corresponding to volumes > 2.9×10^{-1} m^3.

4.4 Comparisons between Sites

The detected rockfall volumes were normalized per unit of time and unit slope area to compare the rockfall rates between the three sites. A consistent threshold volume of 2.9×10^{-1} m^3 was used when evaluating rockfall count. This corresponds to the highest detected cutoff volume across the three sites. Table 4.4 displays the number of detected rockfalls above the unified cutoff volume per year per area for each site. The comprehensive rockfall inventory is shown in Appendix A.

Table 4.4 Geometry and detected rockfalls at every site.

Site	Total length (m)	Maximum height (m)	Area of the slope (m^2)	Monitoring period (month)	No. of rockfalls > 2.9×10^{-1} m^3	Rate of rockfalls /year/m^2 > 2.9×10^{-1} m^3
1	575	163	78,200	74	37	7.67×10^{-5}
2	771	101	62,400	79	25	6.08×10^{-5}
3	1,220	79	89,600	79	31	5.25×10^{-5}

4.4.1 Rockfall Rates

Variations in rockmass conditions and lithology, and the presence of oversteepened areas at the study sites had considerable impacts on rockfall activity, leading to differing rockfall rates. The presence of shale, in particular, played a significant role in these variations. Moreover, the presence of weaker talus materials with considerable thickness also contributed to the differences in rockfall activity. At Site 1, rockfalls originated from three sources: sandstone, thick weathered shale, and loose talus material. However, at Site 2, rockfalls were observed in sandstone and talus material, while at Site 3, rockfalls were limited to the predominant sandstone beds. The total rate of rockfall activity increases as weaker geological units, such as shale, and loose surficial deposits, like talus, become more prevalent on the slope. At Site 1, the increase in rockfall rates is correlated to the increasing thickness of shale beds, which can reach up to 24 meters, and the presence of loose talus. Additionally, the higher rockfall rates at Site 2 compared to Site 3 can be attributed to the presence of thick talus material.

The presence of a steep, excavated slope in the rock-cut at Site 1 and the steep slip surface of the historical landslide at Site 2 also likely contributed to triggering more rockfalls. This is in comparison to the lower rockfall rates at the natural slopes at Site 3. The exposed steep surfaces can disturb the natural equilibrium of rockmass, weakening the slope and increasing its vulnerability to weathering and erosion (Fookes, 1997; Graber & Santi, 2022b). These factors increase the potential for rockfalls to occur.

Figure 4.32 illustrates the variations in rockfall rates for volumes greater than 2.9×10^{-1} m^3 throughout the monitoring period at each site. The primary observation from these rates is the relatively consistent trends in rockfall rates between the sites. A positive correlation was found when comparing these trends to the climate data from the Altenbern Meteorological Station. This station is located 22 km northwest of DeBeque city, with coordinates of 39.5008º latitude and -108.3794º longitude. Specifically, a correlation was found between increased rockfall rates and

years with a higher number of days experiencing a snowfall thickness exceeding 1 inch per day. Increased snow thickness affects the rockmass strength through the combined impact of ice formation and melting processes (freeze-thaw cycles). Numerous studies have confirmed the correlation between the frequency of freeze-thaw cycles and rockfall activity (e.g. Strunden et al., 2015; D'Amato et al, 2016; Pratt et al., 2019; Bajni et al., 2021).

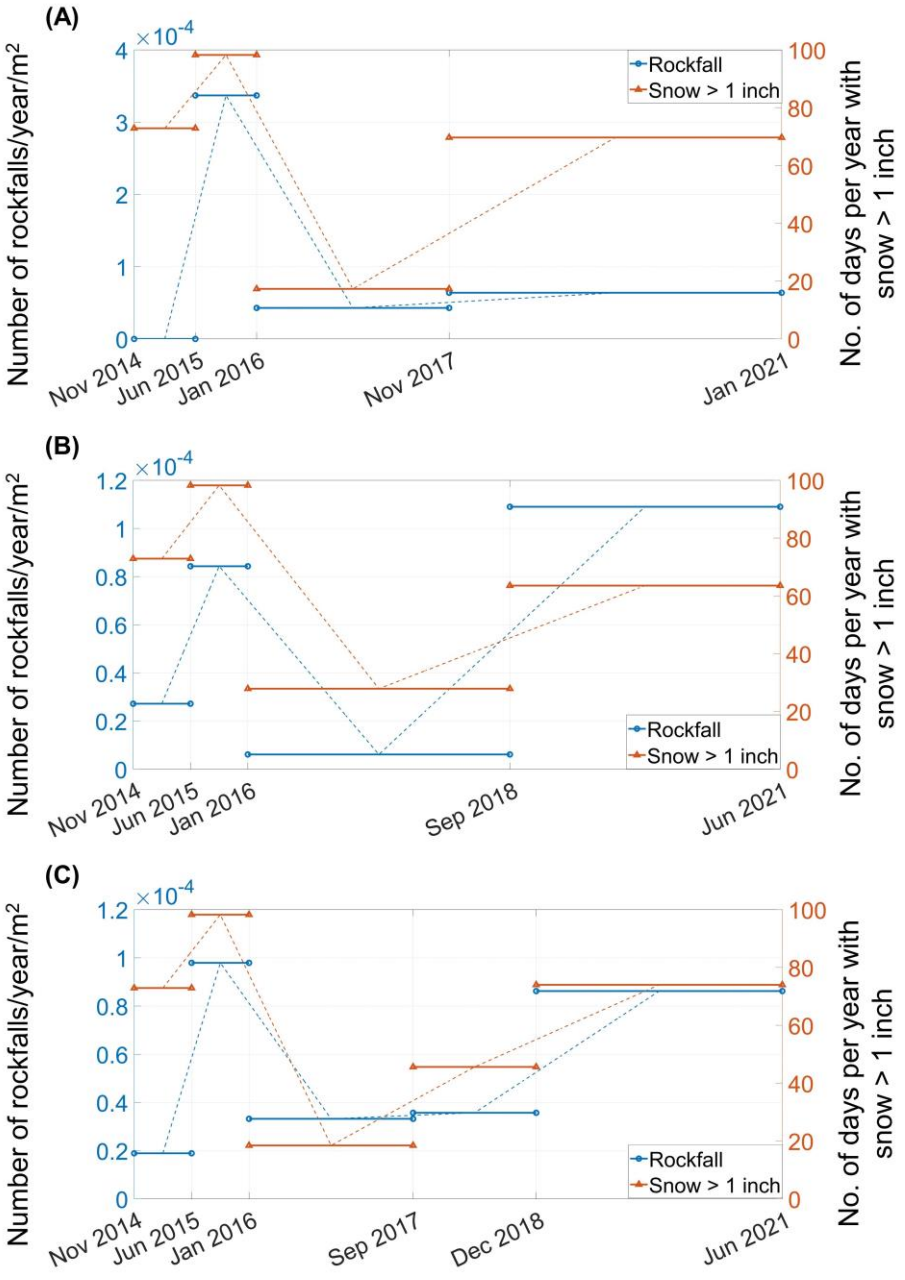

Figure 4.32 Fluctuation of rockfall rates throughout the monitoring period along the three sites for volumes > 2.9×10^{-1} m^3. Panels A, B, and C display the relationship between rockfall rates and the number of days with snow thickness exceeding 1 inch during each monitoring period at Site 1, Site 2, and Site 3, respectively. The vertical axes are not uniform across the three panels due to the differences in rockfall rates at each site.

4.4.2 Magnitude-Cumulative Frequency (MCF) Curves

MCF curves for landslides generally follow a power law distribution for several orders of magnitude above the rollover threshold. The rollover feature is common in the landslide curves and aids in identifying the minimum consistently detectable rockfall volume (Hungr et al., 1999; Strunden et al., 2015). It can vary based on the data collection methods. Stark and Hovius (2001) demonstrated that the under-sampling of small events is controlled by the resolution of the datasets. Accordingly, in this case, the primary reason for the observed rollover in the current datasets is interpreted to be due to variations in the resolution of the captured images during different acquisitions. The 2014 acquisition employed three scan lines and captured images from a considerable distance, while the 2021 acquisition utilized eight scan lines and close-range imaging (Figure 4.33). As a result, the distant-range images from 2014 limited the ability of change detection process to detect all the smaller rockfalls. This discrepancy prevented the consistent representation of smaller rockfalls.

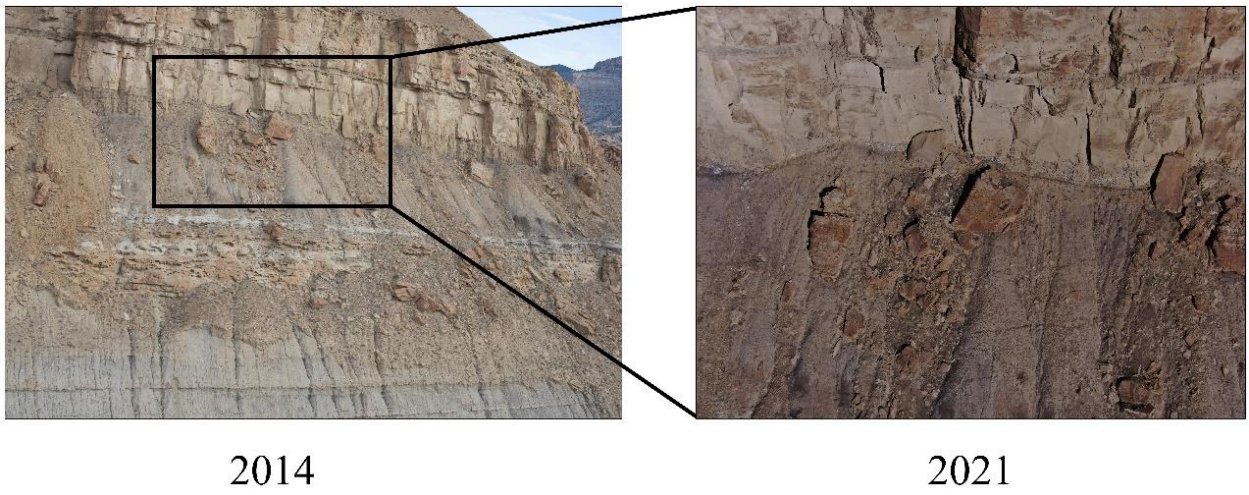

Figure 4.33 Difference between the distant-range images of the 2014 acquisition and the close-range images captured in the 2021 acquisition.

Comparison of the MCF curves for the three different sites (Figure 4.34) showed that Site 2 has the smallest cutoff volume of 2.0×10^{-2} m^3, while Site 3 has the largest (2.9×10^{-1} m^3). However, Site 3 has the highest tie point density of all three sites. This indicates that model quality factors other than resolution, which are not captured by tie point density, must be influencing the rockfall detection threshold.

The power-law equations of the three sites in Figure 4.34 also exhibit different scaling exponents, with the highest scaling exponent at Site 1 and the lowest at Site 2. It is interpreted that variations in lithologies and rockmass properties (degree of fracturing) represent the primary influences on these differences. As discussed in Section 4.4.1, the relatively large number of smaller rockfalls at Site 1 can be explained by the relative prevalence of weak shale beds.

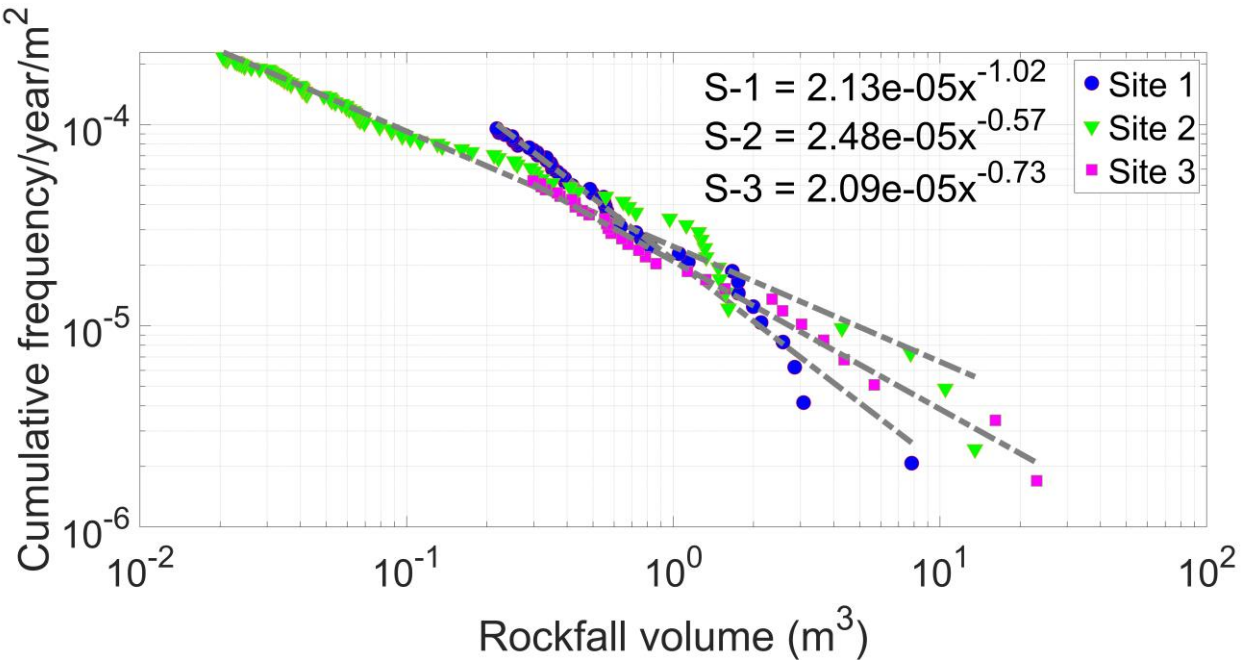

Figure 4.34 MCF curves above the detected cutoff volume corresponding to each site.

To isolate the influence of degree of fracturing and eliminate the potential influence of variable lithologies between sites on the scaling exponent, MCF curves were generated for the sandstone across the three sites (Figure 4.35). These MCF curves revealed similar variations in scaling exponent between the sites, with the lowest scaling exponent at Site 2 (0.47). Both Site 1 and Site 3 exhibit relatively lower overall frequencies and smaller rockfall sizes compared to Site 2. Effectively, the lower degree of fracturing at Site 2 is interpreted to lead to incerased occurrence of larger rockfalls. Based on the manual fracture mapping (described in Section 3.3), the degree of fracturing for the sandstone units was quantified using total discontinuity trace length per area (P21) for a representative sandstone exposure at each site (Table 4.5). Based on fracture intensity (P21), Site 2, which consists of massive sandstone beds, exhibits the lowest degree of fracturing. This is interpreted to explain, in large part, sandstone at Site 2 having the

lowest scaling exponent of 0.47, as Hungr et al. (1999) previously suggested fracture density acts as a major control on scaling exponents.

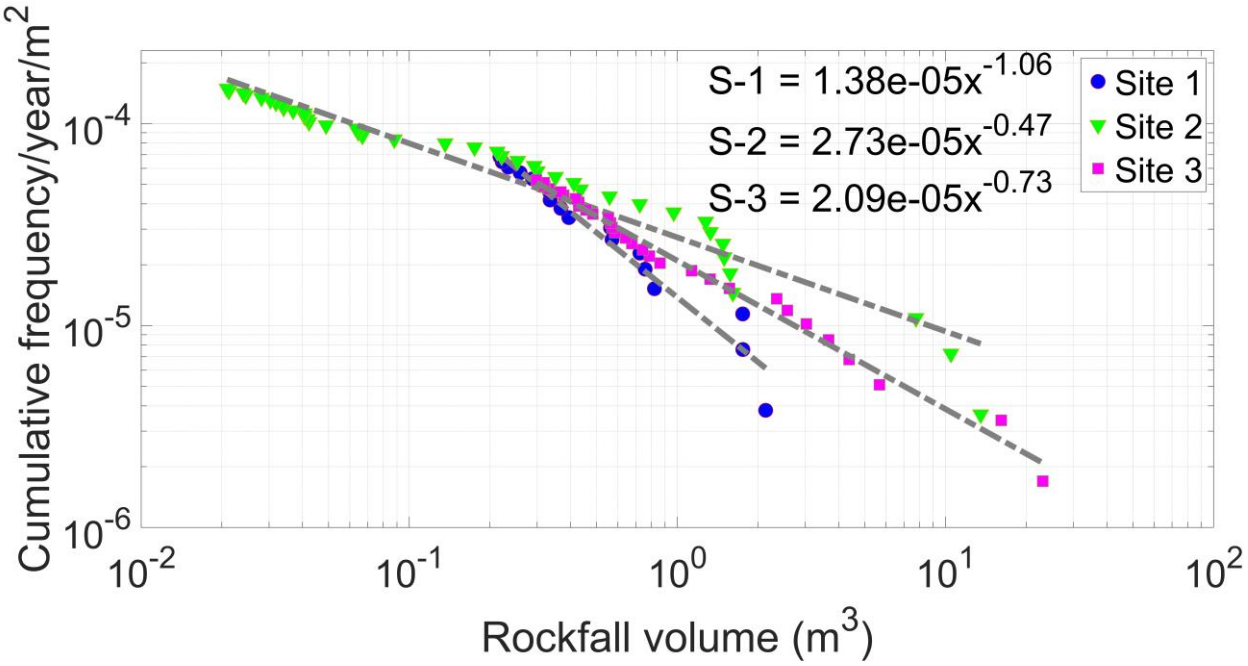

Figure 4.35 MCF curves above the detected cutoff volume corresponding to sandstone at the three sites. Note that frequencies are normalized by the area of exposed sandstone at each site (rather than the full slope area).

Table 4.5 Calculated fracture intensity for the sandstone at the three sites.

Site #	Length of segment (m)	Width of segment (m)	Area (m^2)	Sum of fracture lengths (m)	Fracture intensity (P21)
1	59	38	2242	650	0.29
2	58	40	2320	205	0.09
3	60	44	2640	672	0.25

The small difference in P21 between Sites 1 and 3 is not sufficient to explain the large difference in scaling exponents for sandstone-source rockfalls between Site 1 and Site 3 (1.06 & 0.73, respectively). While the cause of this difference is unknown, one potential explaination could be differences in slope aspect. The slope aspect influences rockfall rates through factors such as temperature fluctuations (Mazzoccola and Hudson, 1996; Watters, 1998) and varying vegetation cover (Branson, 1990). Site 1, a south-facing slope, experiences greater temperature variations, and therefore potentially more freeze-thaw cycles than Sites 2 and 3, which are north-

facing slopes. While one might expect this to cause an increase in rockfall activity, the results in Figure 4.35 show that the sandstone at Site 1 exhibits an increase rate of rockfall for the smallest volumes, but a reduced occurrence of larger rockfalls. This could potentially relate to the increased sunlight on the rock slope at Site 1 limiting the length of the average freezing period and therefore minimizing the depth of freezing, but further investigation is required to evaluate this hypothesized mechanism.

Variations in data collection frequency have also been shown to affect observed MCF curves, with scaling exponents tending to increase with increased scanning intervals due to superposition of multiple events into one change cluster (Van Veen, 2017; Williams et al., 2019). However, the extent of such an effect as documented in these previous studies is minimal compared to the observed variations between sites in this thesis.

As noted above, the results presented are generally consistent with Hungr et al. (1999), who showed that rocks with greater fracturing exhibit higher scaling exponents than those composed of massive rock. However, our results are not consistent with the findings of Westoby et al. (2020) and the meta-analysis of 32 rockfall inventories conducted by Graber & Santi (2022b). These two studies concluded that weaker rockmasses exhibit lower scaling factors compared to competent rockmasses. The discrepancy between our findings and those of Westoby et al. (2020) and Graber & Santi (2022b) can be attributed to the distinct variables and factors considered in each study. Westoby et al. (2020) analyzed changes in rock mineralization, finding that more dolomitized rock exhibited higher scaling factors than brecciated rock. Similarly, in their choice of rockmass criteria, Graber & Santi (2022b) took into account both the degree of fracturing and the degree of weathering when evaluating variations in scaling exponents, finding that slopes with “poor” rockmass condition had lower scaling exponents compared to those with “good” rockmass condition. In our study, the primary difference in the exposed sandstones across the three sites is the degree of fracturing (independent of weathering/alteration). The presented findings are therefore most directly comparable with those of Hungr et al. (1999), who also explicitly considered fracture density. However, while their study accounted for both the degree of fracturing and changes in rock type, the results in Figure 4.35 are strictly for sandstone, effectively isolating the effects of degree of fracturing (and slope aspect).

As previously mentioned, Benjamin et al. (2020) recommended monitoring a combined total length of 2.5 km slopes. This is necessary for acquiring a stable estimate of the relative

occurrence of large and small rockfall volumes along large-scale slopes. The combined length of the selected study sites exceeds this 2.5 km threshold. Consequently, the total MCF curve for DeBeque Canyon was estimated and is presented in Figure 4.36. This summary curve can be used for high-level decision making relevant to hazard assessment, risk management, and maintenance budgeting. In other words, this data can support CDOT in making well-informed decisions about resource allocation.

However, it should be noted that Benjamin et al.'s (2020) research focused on rockfall activities along a coastal strip where the rockfall activities were consistent across the entire length of the large-scale study site. In contrast, the present study observed diverse rockfall activities and multiple rockfall sources from the southern to the northern section of DeBeque Canyon. As a result, the derived MCF curve may not adequately represent the overall activity throughout the entire Canyon.

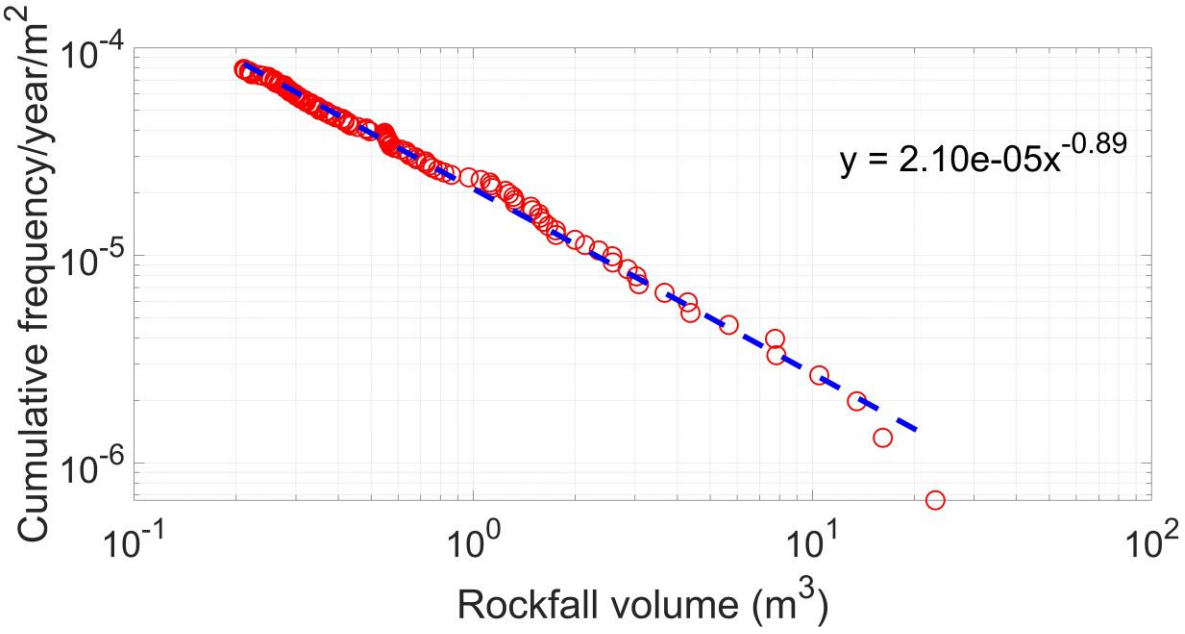

Figure 4.36 MCF for the rockfalls along DeBeque Canyon.

CHAPTER 5 CONCLUSIONS

The photogrammetric datasets acquired in DeBeque Canyon provided an excellent opportunity to examine rockfall activities on a large scale. It also helped to assess the effectiveness of implementing a suitable approach for handling large datasets. The following sub-sections summarize the conclusions of this research with respect to each of the research questions posed.

5.1 Effectiveness of Direct Geo-referencing

This study has demonstrated the effectiveness of the direct geo-referencing approach. This approach serves as an alternative to traditional methods using ground control points (GCPs), especially for large-scale, high, and steep rock slopes. This approach has reduced the time and effort of geo-referencing by directly utilizing the camera coordinates recorded during image acquisition. The case studies presented in this research involved the comparison of photogrammetric point clouds generated using direct geo-referencing with lidar surveys for Sites 1 and 3. This offered a quantitative assessment of the method's accuracy. Results showed that Site 1 had well-aligned point clouds, with a RMS difference metric ranging from 0.059 to 0.063 m, while Site 3 had a RMS ranging from 0.09 to 0.12 m. The higher RMS value for Site 3 was attributed to the lower quality of the lidar data.

A geometric distortion "bowl-effect" was observed in the photogrammetric models when compared to lidar. This was due to inaccurate estimation of the camera's internal parameters because of fixed imaging angles and ranges. To enhance the reconstruction quality and reduce the geometric distortion of photogrammetric models, varying imaging angles and different ranges of scan lines should be considered (Jaud et al., 2018). To address the "bowl-effect" observed in large models, the models were divided into smaller 50-90 m long segments. This approach minimized the amount of geometric distortion within each segment used for analysis and decreased the processing time needed to handle large models.

5.2 Identification of Rockfalls in Multi-epoch Acquisitions

Large-scale multi-epoch models present distinct challenges compared to small-scale models in terms of the time needed for model construction and subsequent processing for change detection. In this study, the selected sites had lengths ranging from 575 to 1,220 m, necessitating an

approach that is time-efficient in constructing models and identifying rockfalls. The proposed approach involved constructing photogrammetric models for only the first and last acquisition dates. Using these models, rockfalls occurring during the monitoring period were identified and recorded. The identification of rockfall occurrences between intermediate acquisitions was carried out by manually reviewing the corresponding image datasets. This method avoided the time required for building photogrammetric models for intermediate years. Knowing the spatial occurrence of every rockfall reduced the number of images to review, which facilitated the identification of each rockfall's temporal occurrence. The manual segmentation of rockfalls based on their temporal occurrence provided a reasonable approximation of the actual rockfall volumes.

5.3 Spatial Variability of Rockfalls along DeBeque Canyon

The conducted study demonstrated that rockfall rates vary along the Canyon. The highest rate was observed at Site 1 in the southern section (7.67 x 10^{-5} rockfalls/year/m²), followed by Site 2 (6.08 x 10^{-5} rockfalls/year/m²). The lowest rate was observed at Site 3 in the northern section (5.25 x 10^{-5} rockfalls/year/m²). The detected rockfall volume ranges also exhibited variation across the sites: Site 1 (1.0×10^{-2} m^3 to 7.8 m^3), Site 2 (3×10^{-4} m^3 to 13.5 m^3), and Site 3 (4×10^{-4} m^3 to 23.1 m^3).

The MCF curves at the three sites followed a power-law distribution after exceeding site-specific threshold volumes. Site 2 exhibited the smallest cutoff volume of 2.0×10^{-2} m^3, while Site 1 and Site 3 exhibited cutoff volumes of 2.1×10^{-1} m^3 and 2.9×10^{-1} m^3, respectively. The scaling factor of the power-law equations also varies among the three sites, from 1.02 at Site 1 to 0.73 at Site 2 and 0.57 at Site 3. The analysis of rockfall shapes above the cutoff volume at each site revealed similarities between Sites 1 and 3. Rockfall shapes were mostly bladed, very bladed, and very elongate. In contrast, Site 2 has a wide variety of rockfall shapes spanning nine of the ten categories defined by Sneed and Folk's (1958) classification.

At Site 1, most rockfalls are concentrated in the steep rock-cut excavation portion. This portion consists of a thick shale layer interbedded with thin sandstone beds and covered by talus. The primary triggers of rockfalls in this section are the weathering of the shale layer, differential weathering of the thin sandstone beds, and the movement of talus material. Similarly, at Site 2, the majority of rockfalls are concentrated at the steep slip surface of the historical landslide that consists of weathered sandstone covered by thick loose talus. At Site 3, the spatial distribution of

rockfalls is affected by variations in slope angles throughout the site. Steeper slopes expose critical joints, leading to increased rockfall formation compared to gentler slopes.

Variations of rockfall rates across the three sites were influenced by several factors. These include differences in lithologies, degree of fracturing, and the occurrence of oversteepened surfaces. The overall rate of rockfall activity rises when weaker geological formations, such as the thick shale at Site 1, are more widespread on the slope. The presence of a steep, excavated slope in the rock-cut at Site 1 and the steep slip surface of the historical landslide at Site 2 also likely contributed to triggering more rockfalls. Rocks with greater fracturing such as the sandstones at Sites 1 and 3 exhibit higher scaling exponents than those composed of massive rock such as the sandstone at Site 2.

The fluctuations in rockfall rates over the monitoring period at each site were observed to be correlated to the prevailing climatic conditions. A positive correlation was observed between the temporal variation of rockfall rates and years with a higher number of days with snow thickness exceeding 1 inch. The increase in snow thickness influences rockmass strength through the combined effects of ice formation and melting processes, such as freeze-thaw cycles.

5.4 Structural Controls on Rockfall Occurrence

The influence of pre-existing rockmass structures on rockfalls was observed in the failure mechanisms, the rockfall shapes, and the scaling exponent of the power-law equation for each site. Pre-existing structures are prominent in Sites 1 and 3, while Site 2 consists of massive sandstone with few structures. At Sites 1 and 3, the failed rock blocks are largely delineated by the mapped joint sets. The steepness of the semi-orthogonal joint sets provides potential sliding surfaces for rockfalls. The impact of the prevailing structures is also evident in the rockfall shapes at Sites 1 and 3. Distinctive shapes form according to the orientation and spacing between joints. In contrast, Site 2 lacks distinctive rockfall shapes due to the absence of prominent structures. The scaling exponent of the power-law equation was correlated to the degree of fracturing at Site 2. This site has the lowest fracture intensity in comparison to the other locations, which is reflected in its minimal scaling exponent of 0.47.

The expected range of block volumes was considerably larger than the actual rockfall volumes at Sites 1 and 3. These differences are influenced by the model resolution and the presence of other factors that trigger smaller rockfalls. The lower resolution of the point cloud

led to smaller joints being missed during mapping, resulting in larger expected block sizes. Other factors, such as intact rock failures or rockfalls not bounded by joints also contributed to block sizes being smaller than those typically estimated based on structural mapping data.

5.5 Future Research Directions

The conducted research in this thesis has revealed two main potential areas for future work that can be summarized as follows:

1. One could conduct a more comprehensive study on the relationship between geology and rockfall characteristics along the Canyon. This could be done by developing additional photogrammetric models to fill the gaps between the models used in the current research. This approach could enable the identification of specific geological factors contributing to rockfall susceptibility, such as rock type, weathering processes, faults, and slope angles. Filling the gaps between the studied sites would provide better spatial coverage and allow for evaluation of variations throughout the entire Canyon.
2. Another interesting approach could also explore the application of machine learning techniques for the identification of rockfalls. Machine learning algorithms can be employed to automatically detect rockfall events from change maps derived from point cloud data, differentiating between rockfalls and other features, such as change clusters associated with vegetation. This approach would significantly reduce the time required for manual verification of rockfalls.

REFERENCES

Abellan, A., Derron, M.-H., & Jaboyedoff, M. (2016). Use of 3D point clouds in geohazards special issue: current challenges and future trends. *Remote Sensing*, 8, 130. https://doi.org/10.3390/rs8020130

Agisoft (2023) Metashape Professional Edition Version 2.0, User Manual https://www.agisoft.com/pdf/metashape-pro_2_0_en.pdf.

Agüera-Vega, F., Carvajal-Ramírez, F., & Martínez-Carricondo, P. (2017). Assessment of photogrammetric mapping accuracy based on variation ground control points number using unmanned aerial vehicle. *Measurement*, *98*, 221-227. https://doi.org/10.1016/j.measurement.2016.12.002

Allen, S., & Huggel, C. (2013). Extremely warm temperatures as a potential cause of recent high mountain rockfall. *Global and Planetary Change, 107*, 59-69. https://doi.org/10.1016/j.gloplacha.2013.04.007

Arya, S., Mount, D. M., Netanyahu, N. S., Silverman, R., & Wu, A. Y. (1998). An optimal algorithm for approximate nearest neighbor searching fixed dimensions. *Journal of the ACM (JACM)*, *45*(6), 891-923.

Baily, B., & Nowell, D. (1996). Techniques for monitoring coastal change: a review and case study. *Ocean & coastal management*, *32*(2), 85-95.

Bajni, G., Camera, C. A., & Apuani, T. (2021). Deciphering meteorological influencing factors for Alpine rockfalls: a case study in Aosta Valley. *Landslides*, *18*(10), 3279-3298. https://doi.org/10.1007/s10346-021-01697-3

Benjamin, J., Rosser, N. J., & Brain, M. J. (2020). Emergent characteristics of rockfall inventories captured at a regional scale. *Earth Surface Processes and Landforms*, *45*(12), 2773-2787. https://doi.org/10.1002/esp.4929

Besl, P. J., & McKay, N. D. (1992). Method for registration of 3-D shapes. *In Sensor fusion IV: control paradigms and data structures*, 1611, 586-606. https://doi.org/10.1117/12.57955

Brach, M., Chan, J.-W., & Szymanski, P. (2019). Accuracy assessment of different photogrammetric software for processing data from low-cost UAV platforms in forest conditions. *iForest-Biogeosciences and Forestry*, *12*(5), 435-441. https://doi.org/10.3832/ifor2986-012

Branson, F. A., & Shown, L. M. (1990). Contrasts of vegetation, soils, microclimates, and geomorphic processes between north-and south-facing slopes on Green Mountain near Denver, Colorado (Vol. 89, No. 4094). *Department of the Interior, US Geological Survey*.

Brawner, C., & Wyllie, D. (1976). Rock slope stability on railway projects. *Area Bulletin, 77*(Bulletin 656).

Brown, M., & Lowe, D. G. (2005). Unsupervised 3D object recognition and reconstruction in unordered datasets. Fifth International Conference on 3-D Digital Imaging and Modeling (3DIM'05), 56-63. doi: 10.1109/3DIM.2005.81

Budetta, P., & Santo, A. (1994). Morphostructural evolution and related kinematics of rockfalls in Campania (southern Italy): A case study. *Engineering Geology*, *36*(3-4), 197-210. https://doi.org/10.1016/0013-7952(94)90004-3

Bunce, C., Cruden, D., & Morgenstern, N. (1997). Assessment of the hazard from rock fall on a highway. *Canadian Geotechnical Journal*, *34*(3), 344-356. https://doi.org/10.1139/t97-009

Cai, M., Kaiser, P., Uno, H., Tasaka, Y., & Minami, M. (2004). Estimation of rock mass deformation modulus and strength of jointed hard rock masses using the GSI system. *International Journal of Rock Mechanics and Mining Sciences*, *41*(1), 3-19. https://doi.org/10.1016/S1365-1609(03)00025-X

Cashion, W. B. (1973). *Geologic and structure map of the Grand Junction quadrangle, Colorado and Utah*. *U.S. Geological Survey*. https://doi.org/10.3133/i736

Clauset, A., Shalizi, C. R., & Newman, M. E. (2009). Power-law distributions in empirical data. *SIAM review*, *51*(4), 661-703. https://doi.org/10.1137/070710111

CloudCompare (2021) cloudcompare.org, Version 2.12, Open Source Project

Costa, S., Delahaye, D., Freiré-Diaz, S., Di Nocera, L., Davidson, R., & Plessis, E. (2004). Quantification of the Normandy and Picardy chalk cliff retreat by photogrammetric analysis. *Geological Society, London, Engineering Geology Special Publications*, *20*(1), 139-148. https://doi.org/10.1144/GSL.ENG.2004.020.01.11

Cruden, D., & Varnes, D. (1996). Landslide Types and Processes. Chapter 3 in Landslides: Investigation and Mitigation. *Washington, DC: National Research Council*. *Transportation Research Board*, Special Report, 247, 36-75.

D'Amato, J., Hantz, D., Guerin, A., Jaboyedoff, M., Baillet, L., & Mariscal, A. (2016). Influence of meteorological factors on rockfall occurrence in a middle mountain limestone cliff. *Natural Hazards and Earth System Sciences*, *16*(3), 719-735. https://doi.org/10.5194/nhess-16-719-2016

de Vilder, S. J., Rosser, N. J., & Brain, M. J. (2017). Forensic analysis of rockfall scars. *Geomorphology*, *295*, 202-214. https://doi.org/10.1016/j.geomorph.2017.07.005

Delonca, A., Gunzburger, Y., & Verdel, T. (2014). Statistical correlation between meteorological and rockfall databases. *Natural Hazards and Earth System Sciences*, *14*(8), 1953-1964. https://doi.org/10.5194/nhess-14-1953-2014

DiFrancesco, P.-M., Bonneau, D., & Hutchinson, D. J. (2020). The implications of M3C2 projection diameter on 3D semi-automated rockfall extraction from sequential terrestrial laser scanning point clouds. *Remote Sensing*, *12*(11), 1885. https://doi.org/10.3390/rs12111885

DiFrancesco, P.-M., Bonneau, D. A., & Hutchinson, D. J. (2021). Computational geometry-based surface reconstruction for volume estimation: a case study on magnitude-frequency relations for a LiDAR-derived rockfall inventory. *ISPRS International Journal of Geo-Information*, *10*(3), 157. https://doi.org/10.3390/ijgi10030157

Donnell, J. R. (1961), Tertiary geology and oil-shale resources of the Piceance Creek Basin between the Colorado and White Rivers, northwestern Colorado. *U.S. Geological Survey,* Bulletin 1082-L, 835 – 891.

Dorren, L. K. (2003). A review of rockfall mechanics and modelling approaches. *Progress in Physical Geography*, *27*(1), 69-87. https://doi.org/10.1191/0309133303pp359ra

d'Oleire-Oltmanns, S., Marzolff, I., Peter, K. D., & Ries, J. B. (2012). Unmanned aerial vehicle (UAV) for monitoring soil erosion in Morocco. *Remote Sensing*, *4*(11), 3390-3416. https://doi.org/10.3390/rs4113390

Ellis, M. S., & Gabaldo, V. (1989). Geologic map and cross sections of parts of the Grand Junction and Delta 30'x 60'quadrangles, west-central Colorado. *U.S. Geological Survey.* https://doi.org/10.3133/coal124

Eltner, A., Kaiser, A., Castillo, C., Rock, G., Neugirg, F., & Abellán, A. (2016). Image-based surface reconstruction in geomorphometry–merits, limits and developments. *Earth Surface Dynamics*, *4*(2), 359-389. https://doi.org/10.5194/esurf-4-359-2016

Eltner, A., & Schneider, D. (2015). Analysis of different methods for 3D reconstruction of natural surfaces from parallel-axes UAV images. *The Photogrammetric Record*, *30*(151), 279-299. https://doi.org/10.1111/phor.12115

Erdmann, C. E. (1934). The Book Cliffs Coal Field in Garfield and Mesa Counties, Colorado. *U.S. Geological Survey,* Bulletin 851, 150 p.

Ester, M., Kriegel, H.-P., Sander, J., & Xu, X. (1996). A density-based algorithm for discovering clusters in large spatial databases with noise. *kdd*, 226–231.

Ferrero, A. M., & Umili, G. (2011). Comparison of methods for estimating fracture size and intensity applied to Aiguille Marbrée (Mont Blanc). *International Journal of Rock Mechanics and Mining Sciences*, *48*(8), 1262-1270. https://doi.org/10.1016/j.ijrmms.2011.09.011

Fonstad, M. A., Dietrich, J. T., Courville, B. C., Jensen, J. L., & Carbonneau, P. E. (2013). Topographic structure from motion: a new development in photogrammetric measurement. *Earth surface processes and Landforms*, *38*(4), 421-430. https://doi.org/10.1002/esp.3366

Fookes, P. (1997). Geology for engineers: the geological model, prediction and performance. *Quarterly Journal of Engineering Geology and Hydrogeology*, *30*(4), 293-424. https://doi.org/10.1144/GSL.QJEG.1997.030.P4.02

Fuhrmann, S., Langguth, F., & Goesele, M. (2014). Mve-a multi-view reconstruction environment. *GCH*, 11-18. http://dx.doi.org/10.2312/gch.20141299

Furukawa, Y., & Hernández, C. (2015). Multi-view stereo: A tutorial. *Foundations and Trends® in Computer Graphics and Vision*, *9*(1-2), 1-148. http://dx.doi.org/10.1561/0600000052

Gabrlik, P. (2015). The use of direct georeferencing in aerial photogrammetry with micro UAV. *IFAC-PapersOnLine*, *48*(4), 380-385. https://doi.org/10.1016/j.ifacol.2015.07.064

Gallo, I. G., Martínez-Corbella, M., Sarro, R., Iovine, G., López-Vinielles, J., Hérnandez, M., . . . García-Davalillo, J. C. (2021). An Integration of UAV-Based Photogrammetry and 3D Modelling for Rockfall Hazard Assessment: The Cárcavos Case in 2018 (Spain). *Remote Sensing*, *13*(17), 3450. https://doi.org/10.3390/rs13173450

Giacomini, A., Thoeni, K., Santise, M., Diotri, F., Booth, S., Fityus, S., & Roncella, R. (2020). Temporal-spatial frequency rockfall data from open-pit highwalls using a low-cost monitoring system. *Remote Sensing*, *12*(15), 2459. https://doi.org/10.3390/rs12152459

Gigli, G., Lombardi, L., Carla, T., Beni, T., & Casagli, N. (2022). A method for full three-dimensional kinematic analysis of steep rock walls based on high-resolution point cloud data. *International Journal of Rock Mechanics and Mining Sciences*, *157*, 105178. https://doi.org/10.1016/j.ijrmms.2022.105178

Giordan, D., Manconi, A., Facello, A., Baldo, M., Allasia, P., & Dutto, F. (2015). Brief Communication: The use of an unmanned aerial vehicle in a rockfall emergency scenario. *Natural Hazards and Earth System Sciences*, *15*(1), 163-169. https://doi.org/10.5194/nhess-15-163-2015

Glueer, F., Loew, S., Seifert, R., Aaron, J., Grämiger, L., Conzett, S., . . . Manconi, A. (2021). Robotic total station monitoring in high alpine paraglacial environments: Challenges and solutions from the Great Aletsch region (Valais, Switzerland). *Geosciences*, *11*(11), 471. https://doi.org/10.3390/geosciences11110471

Graber, A., & Santi, P. (2022a). UAV-photogrammetry rockfall monitoring of natural slopes in Glenwood Canyon, CO, USA: background activity and post-wildfire impacts. *Landslides*, 20, 229–248. https://doi.org/10.1007/s10346-022-01974-9

Graber, A., & Santi, P. (2022b). Power law models for rockfall frequency-magnitude distributions: review and identification of factors that influence the scaling exponent. *Geomorphology*, 418, 108463. https://doi.org/10.1016/j.geomorph.2022.108463

Guerin, A., Stock, G. M., Radue, M. J., Jaboyedoff, M., Collins, B. D., Matasci, B., . . . Derron, M.-H. (2020). Quantifying 40 years of rockfall activity in Yosemite Valley with historical Structure-from-Motion photogrammetry and terrestrial laser scanning. *Geomorphology, 356*, 107069. https://doi.org/10.1016/j.geomorph.2020.107069

Gómez-Gutiérrez, Á., & Gonçalves, G. R. (2020). Surveying coastal cliffs using two UAV platforms (multirotor and fixed-wing) and three different approaches for the estimation of volumetric changes. *International Journal of Remote Sensing*, *41*(21), 8143-8175. https://doi.org/10.1080/01431161.2020.1752950

Hale, A. J., Calder, E. S., Loughlin, S., Wadge, G., & Ryan, G. A. (2009). Modelling the lava dome extruded at Soufrière Hills Volcano, Montserrat, August 2005–May 2006: Part II: Rockfall activity and talus deformation. *Journal of volcanology and geothermal research, 187*(1-2), 69-84. https://doi.org/10.1016/j.jvolgeores.2009.08.014

Haneberg, W. C. (2008). Using close range terrestrial digital photogrammetry for 3-D rock slope modeling and discontinuity mapping in the United States. *Bulletin of Engineering Geology and the Environment*, *67*(4), 457-469. https://doi.org/10.1007/s10064-008-0157-y

Hantz, D., Corominas, J., Crosta, G. B., & Jaboyedoff, M. (2021). Definitions and concepts for quantitative rockfall hazard and risk analysis. *Geosciences*, *11*(4), 158. https://doi.org/10.3390/geosciences11040158

Hartley, R., & Zisserman, A. (2003). Multiple view geometry in computer vision. *Cambridge university press.*

Harwin, S., Lucieer, A., & Osborn, J. (2015). The impact of the calibration method on the accuracy of point clouds derived using unmanned aerial vehicle multi-view stereopsis. *Remote Sensing*, *7*(9), 11933-11953. https://doi.org/10.3390/rs70911933

Hayakawa, Y. S., & Obanawa, H. (2020). Volumetric change detection in bedrock coastal cliffs using terrestrial laser scanning and uas-based SFM. *Sensors*, *20*(12), 3403. https://doi.org/10.3390/s20123403

Hugenholtz, C., Brown, O., Walker, J., Barchyn, T., Nesbit, P., Kucharczyk, M., & Myshak, S. (2016). Spatial accuracy of UAV-derived orthoimagery and topography: Comparing photogrammetric models processed with direct geo-referencing and ground control points. *Geomatica*, *70*(1), 21-30. https://doi.org/10.5623/cig2016-102

Hungr, O., Evans, S., & Hazzard, J. (1999). Magnitude and frequency of rock falls and rock slides along the main transportation corridors of southwestern British Columbia. *Canadian Geotechnical Journal*, *36*(2), 224-238. https://doi.org/10.1139/t98-106

Hungr, O., Fell, R., Couture, R., & Eberhardt, E. (2005). Landslide risk management. *CRC Press*.

Ikkala, L., Ronkanen, A.-K., Ilmonen, J., Similä, M., Rehell, S., Kumpula, T., . . . Marttila, H. (2022). Unmanned Aircraft System (UAS) Structure-From-Motion (SfM) for Monitoring the Changed Flow Paths and Wetness in Minerotrophic Peatland Restoration. *Remote Sensing*, *14*(13), 3169. https://doi.org/10.3390/rs14133169

James, M. R., & Robson, S. (2012). Straightforward reconstruction of 3D surfaces and topography with a camera: Accuracy and geoscience application. *Journal of Geophysical Research: Earth Surface*, *117*, 1-17. https://doi.org/10.1029/2011JF002289

James, M. R., & Robson, S. (2014). Mitigating systematic error in topographic models derived from UAV and ground-based image networks. *Earth Surface Processes and Landforms*, *39*(10), 1413-1420. https://doi.org/10.1002/esp.3609

Jaud, M., Passot, S., Allemand, P., Le Dantec, N., Grandjean, P., & Delacourt, C. (2018). Suggestions to limit geometric distortions in the reconstruction of linear coastal landforms by SfM photogrammetry with PhotoScan® and MicMac® for UAV surveys with restricted GCPs pattern. *Drones*, *3*(1), 2. https://doi.org/10.3390/drones3010002

Keefer, D. K. (1984). Landslides caused by earthquakes. *Geological Society of America Bulletin*, *95*(4), 406-421. https://doi.org/10.1130/0016-7606(1984)95<406:LCBE>2.0.CO;2

Kolzenburg, S., Favalli, M., Fornaciai, A., Isola, I., Harris, A., Nannipieri, L., & Giordano, D. (2016). Rapid updating and improvement of airborne LIDAR DEMs through ground-based SfM 3-D modeling of volcanic features. *IEEE Transactions on Geoscience and Remote Sensing*, *54*(11), 6687-6699. https://doi.org/10.1109/TGRS.2016.2587798

Kromer, R., Walton, G., Gray, B., Lato, M., & Group, R. (2019). Development and Optimization of an Automated Fixed-Location Time Lapse Photogrammetric Rock Slope Monitoring System. *Remote Sensing*, *11*(16), 1890. https://doi.org/https://doi.org/10.3390/rs11161890

Lague, D., Brodu, N., & Leroux, J. (2013). Accurate 3D comparison of complex topography with terrestrial laser scanner: Application to the Rangitikei canyon (NZ). *ISPRS journal of photogrammetry and remote sensing*, *82*, 10-26. https://doi.org/10.1016/j.isprsjprs.2013.04.009

Lambert, C., Thoeni, K., Giacomini, A., Casagrande, D., & Sloan, S. (2012). Rockfall hazard analysis from discrete fracture network modelling with finite persistence discontinuities. *Rock mechanics and rock engineering*, *45*, 871-884. https://doi.org/10.1007/s00603-012-0250-1

Lato, M., Diederichs, M. S., Hutchinson, D. J., & Harrap, R. (2009). Optimization of LiDAR scanning and processing for automated structural evaluation of discontinuities in rockmasses. *International Journal of Rock Mechanics and Mining Sciences*, *46*(1), 194-199. https://doi.org/10.1016/j.ijrmms.2008.04.007

Lato, M. J., Hutchinson, D. J., Gauthier, D., Edwards, T., & Ondercin, M. (2015). Comparison of airborne laser scanning, terrestrial laser scanning, and terrestrial photogrammetry for mapping differential slope change in mountainous terrain. *Canadian Geotechnical Journal*, *52*(2), 129-140. https://doi.org/10.1139/cgj-2014-0051

Lim, M., Petley, D. N., Rosser, N. J., Allison, R. J., Long, A. J., & Pybus, D. (2005). Combined digital photogrammetry and time-of-flight laser scanning for monitoring cliff evolution. *The Photogrammetric Record*, *20*(110), 109-129. https://doi.org/10.1111/j.1477-9730.2005.00315.x

Lowe, D. G. (2004). Distinctive image features from scale-invariant keypoints. *International journal of computer vision*, *60*(2), 91-110. https://doi.org/10.1023/B:VISI.0000029664.99615.94

Loye, A., Jaboyedoff, M., & Pedrazzini, A. (2009). Identification of potential rockfall source areas at a regional scale using a DEM-based geomorphometric analysis. *Natural Hazards and Earth System Sciences*, *9*(5), 1643-1653. https://doi.org/10.5194/nhess-9-1643-2009

Mauldon, M., Dunne, W., & Rohrbaugh Jr, M. (2001). Circular scanlines and circular windows: new tools for characterizing the geometry of fracture traces. *Journal of structural geology*, *23*(2-3), 247-258. https://doi.org/10.1016/S0191-8141(00)00094-8

Mazzoccola, D., & Hudson, J. (1996). A comprehensive method of rock mass characterization for indicating natural slope instability. *Quarterly Journal of Engineering Geology*, *29*(1), 37-56. https://doi.org/10.1144/GSL.QJEGH.1996.029.P1.03

Mineo, S., Caliò, D., & Pappalardo, G. (2022). UAV-based photogrammetry and infrared thermography applied to rock mass survey for geomechanical purposes. *Remote Sensing*, *14*(3), 473. https://doi.org/10.3390/rs14030473

Moore, L. J., & Griggs, G. B. (2002). Long-term cliff retreat and erosion hotspots along the central shores of the Monterey Bay National Marine Sanctuary. *Marine Geology*, *181*(1-3), 265-283. https://doi.org/10.1016/S0025-3227(01)00271-7

Nadal-Romero, E., Revuelto, J., Errea, P., & López-Moreno, J. (2015). The application of terrestrial laser scanner and SfM photogrammetry in measuring erosion and deposition processes in two opposite slopes in a humid badlands area (central Spanish Pyrenees). *Soil*, *1*(2), 561-573. https://doi.org/10.5194/soil-1-561-2015

Nesbit, P. R., Hubbard, S. M., & Hugenholtz, C. H. (2022). Direct georeferencing UAV-SfM in high-relief topography: Accuracy assessment and alternative ground control strategies along steep inaccessible rock slopes. *Remote Sensing*, *14*(3), 490. https://doi.org/10.3390/rs14030490

Nguyen, T., Park, E., Han, J., Park, D.-C., & Min, S.-Y. (2014). Object detection using scale invariant feature transform. In *Genetic and evolutionary computing. Springer*, 65-72. https://doi.org/10.1007/978-3-319-01796-9_7

Papathanassiou, G., Riquelme, A., Tzevelekis, T., & Evaggelou, E. (2020). Rock Mass Characterization of Karstified Marbles and Evaluation of Rockfall Potential Based on Traditional and SfM-Based Methods; Case Study of Nestos, Greece. *Geosciences*, *10*(10), 389. https://doi.org/10.3390/geosciences10100389

Paronuzzi, P., & Serafini, W. (2009). Stress state analysis of a collapsed overhanging rock slab: a case study. *Engineering Geology*, *108*(1-2), 65-75. https://doi.org/10.1016/j.enggeo.2009.06.019

Peppa, M. V., Mills, J. P., Moore, P., Miller, P. E., & Chambers, J. E. (2019). Automated co-registration and calibration in SfM photogrammetry for landslide change detection. *Earth Surface Processes and Landforms*, *44*(1), 287-303. https://doi.org/10.1002/esp.4502

Piermattei, L., Carturan, L., de Blasi, F., Tarolli, P., Dalla Fontana, G., Vettore, A., & Pfeifer, N. (2016). Suitability of ground-based SfM–MVS for monitoring glacial and periglacial processes. *Earth Surface Dynamics*, *4*(2), 425-443. https://doi.org/10.5194/esurf-4-425-2016

Pikelj, K., Ilić, S., James, M. R., & Kordić, B. (2015). Application of SfM photogrammetry for morphological changes on gravel beaches: Dugi Rat case study (Croatia). *Proceedings of the 3rd Coastal and Maritime Mediterranean Conference, Ferrara, Italia*, 25-27. http://dx.doi.org/10.5150/cmcm.2015.014

Porter, S. C., & Orombelli, G. (1981). Alpine Rockfall Hazards: Recognition and dating of rockfall deposits in the western Italian Alps lead to an understanding of the potential hazards of giant rockfalls in mountainous regions. *American Scientist*, *69*(1), 67-75.

Pratt, C., Macciotta, R., & Hendry, M. (2019). Quantitative relationship between weather seasonality and rock fall occurrences north of Hope, BC, Canada. *Bulletin of Engineering Geology and the Environment*, *78*(5), 3239-3251. https://doi.org/10.1007/s10064-018-1358-7

Priest, S. D., & Hudson, J. (1976). Discontinuity spacings in rock. *International Journal of Rock Mechanics and Mining Sciences & Geomechanics Abstracts*, 13(5), 135-148. https://doi.org/10.1016/0148-9062(76)90818-4

Rabah, M., Basiouny, M., Ghanem, E., & Elhadary, A. (2018). Using RTK and VRS in direct geo-referencing of the UAV imagery. *Nriag journal of astronomy and geophysics*, *7*(2), 220-226. https://doi.org/10.1016/j.nrjag.2018.05.003

Radoane, M. & Dumitriu, D. & Ichim, I. (2020). Geomorfologie - Relieful structural. *Geomorfologie*, I, 135-154.

Riquelme, A. J., Abellán, A., Tomás, R., & Jaboyedoff, M. (2014). A new approach for semi-automatic rock mass joints recognition from 3D point clouds. *Computers & Geosciences*, *68*, 38-52. https://doi.org/10.1016/j.cageo.2014.03.014

Rocscience (2020) Dips 8.0 Graphical and statistical analysis of orientation data. Version 8.004. *Rocscience Inc. Toronto.*

Rodgers, M., Deng, F., Dixon, T. H., Glennie, C. L., James, M. R., Malservisi, R., . . . Xie, S. (2022). Geodetic Applications to Geomorphology. *Treatise on Geomorphology, 2nd ed.; Shroder*. *Academic Press: Oxford, UK*, 34–55. https://doi.org/10.1016/B978-0-12-818234-5.00084-5

Rose, J. C., Paulus, S., & Kuhlmann, H. (2015). Accuracy analysis of a multi-view stereo approach for phenotyping of tomato plants at the organ level. *Sensors*, *15*(5), 9651-9665. https://doi.org/10.3390/s150509651

Rosser, N., & Massey, C. (2022). Rockfall hazard and risk. *Landslide Hazards, Risks, and Disasters*, 581-622. https://doi.org/10.1016/B978-0-12-818464-6.00013-5

Rossi, M., Sarro, R., Reichenbach, P., & Mateos, R. M. (2021). Probabilistic identification of rockfall source areas at regional scale in El Hierro (Canary Islands, Spain). *Geomorphology*, *381*, 107661. https://doi.org/10.1016/j.geomorph.2021.107661

Rott, H., Nagler, T., Rocca, F., Prati, C., Mazzotti, A., Keusen, H., . . . Tarchi, D. (2002). InSAR techniques and applications for monitoring landslides and subsidence. *Geoinformation for Europeanwide integration, Proceedings of the 22nd EARSeL Symposium, Prague*, 25-31.

Ryan, J. C., Hubbard, A. L., Box, J. E., Todd, J., Christoffersen, P., Carr, J. R., . . . Snooke, N. (2015). UAV photogrammetry and structure from motion to assess calving dynamics at Store Glacier, a large outlet draining the Greenland ice sheet. *The Cryosphere*, *9*(1), 1-11. https://doi.org/10.5194/tc-9-1-2015

Santi, P. M., Russell, C. P., Higgins, J. D., & Spriet, J. I. (2009). Modification and statistical analysis of the Colorado rockfall hazard rating system. *Engineering Geology*, *104*(1-2), 55-65. https://doi.org/10.1016/j.enggeo.2008.08.009

Sanz-Ablanedo, E., Chandler, J. H., Rodríguez-Pérez, J. R., & Ordóñez, C. (2018). Accuracy of unmanned aerial vehicle (UAV) and SfM photogrammetry survey as a function of the number and location of ground control points used. *Remote Sensing*, *10*(10), 1606. https://doi.org/10.3390/rs10101606

Saroglou, C., Asteriou, P., Zekkos, D., Tsiambaos, G., Clark, M., & Manousakis, J. (2018). UAV-based mapping, back analysis and trajectory modeling of a coseismic rockfall in Lefkada island, Greece. *Natural Hazards and Earth System Sciences*, *18*(1), 321-333. https://doi.org/10.5194/nhess-18-321-2018

Sarro, R., Riquelme, A., García-Davalillo, J. C., Mateos, R. M., Tomás, R., Pastor, J. L., . . . Herrera, G. (2018). Rockfall simulation based on UAV photogrammetry data obtained during an emergency declaration: Application at a cultural heritage site. *Remote Sensing*, *10*(12), 1923. https://doi.org/10.3390/rs10121923

Schenk, T. (2005). Introduction to photogrammetry. *The Ohio State University, Columbus*, *106*.

Schovanec, H., Walton, G., Kromer, R., & Malsam, A. (2021). Development of Improved Semi-Automated Processing Algorithms for the Creation of Rockfall Databases. *Remote Sensing*, *13*(8), 1479. https://doi.org/https://doi.org/10.3390/rs13081479

Schwind, M. (2016). Comparing and characterizing three-dimensional point clouds derived by structure from motion photogrammetry. *Ph.D. thesis, Texas A&M University Corpus Christi*.

Seitz, S. M., Curless, B., Diebel, J., Scharstein, D., & Szeliski, R. (2006). A comparison and evaluation of multi-view stereo reconstruction algorithms. *IEEE computer society conference on computer vision and pattern recognition (CVPR'06)*, 1, 519-528. https://doi.org/10.1109/CVPR.2006.19

Smith, M. W., & Vericat, D. (2015). From experimental plots to experimental landscapes: topography, erosion and deposition in sub-humid badlands from structure-from-motion photogrammetry. *Earth Surface Processes and Landforms*, *40*(12), 1656-1671. https://doi.org/10.1002/esp.3747

Snavely, N., Seitz, S. M., & Szeliski, R. (2008). Modeling the world from internet photo collections. *International journal of computer vision*, *80*(2), 189-210. https://doi.org/10.1007/s11263-007-0107-3

Sneed, E. D., & Folk, R. L. (1958). Pebbles in the lower Colorado River, Texas a study in particle morphogenesis. *The Journal of Geology*, *66*(2), 114-150. https://doi.org/10.1086/626490

Stark, C. P., & Hovius, N. (2001). The characterization of landslide size distributions. *Geophysical research letters*, *28*(6), 1091-1094. https://doi.org/10.1029/2000GL008527

Stead, D., & Coggan, J. (2012). 13 Numerical modeling of rock-slope instability. *Landslides: Types, mechanisms and modeling*, 144.

Strunden, J., Ehlers, T. A., Brehm, D., & Nettesheim, M. (2015). Spatial and temporal variations in rockfall determined from TLS measurements in a deglaciated valley, Switzerland. *Journal of Geophysical Research: Earth Surface*, *120*(7), 1251-1273. https://doi.org/10.1002/2014JF003274

Stumpf, A., Malet, J.-P., Allemand, P., Pierrot-Deseilligny, M., & Skupinski, G. (2015). Ground-based multi-view photogrammetry for the monitoring of landslide deformation and erosion. *Geomorphology*, *231*, 130-145. https://doi.org/10.1016/j.geomorph.2014.10.039

Sturzenegger, M., & Stead, D. (2009). Close-range terrestrial digital photogrammetry and terrestrial laser scanning for discontinuity characterization on rock cuts. *Engineering Geology*, *106*(3-4), 163-182. http://dx.doi.org/10.1016/j.enggeo.2009.03.004

Sturzenegger, M., & Stead, D. (2012). The Palliser Rockslide, Canadian Rocky Mountains: characterization and modeling of a stepped failure surface. *Geomorphology, 138*(1), 145-161. http://dx.doi.org/10.1016/j.geomorph.2011.09.001

Sturzenegger, M., Stead, D., & Elmo, D. (2011). Terrestrial remote sensing-based estimation of mean trace length, trace intensity and block size/shape. *Engineering Geology*, *119*(3-4), 96-111. http://dx.doi.org/10.1016/j.enggeo.2011.02.005

Teppati Losè, L., Chiabrando, F., & Giulio Tonolo, F. (2020). Are measured ground control points still required in UAV based large scale mapping? assessing the positional accuracy of an RTK multi-rotor platform. *International Archives of the Photogrammetry, Remote Sensing & Spatial Information Sciences*.

Terzaghi, R. D. (1965). Sources of error in joint surveys. *Geotechnique, 15*(3), 287-304. https://doi.org/10.1680/geot.1965.15.3.287

Teza, G., Marcato, G., Pasuto, A., & Galgaro, A. (2015). Integration of laser scanning and thermal imaging in monitoring optimization and assessment of rockfall hazard: a case history in the Carnic Alps (Northeastern Italy). *Natural Hazards*, *76*(3), 1535-1549. https://doi.org/10.1007/s11069-014-1545-1

Tonini, M., & Abellan, A. (2014). Rockfall detection from terrestrial LiDAR point clouds: A clustering approach using R. *Journal of Spatial Information Science,* (8), 95-110. http://dx.doi.org/10.5311/JOSIS.2014.8.123

Tweto, O. (1979). Geologic map of Colorado: U.S. Geological Survey, scale 1:500,000. *U.S. Geological Survey.*

Török, Á., Barsi, Á., Bögöly, G., Lovas, T., Somogyi, Á., & Görög, P. (2018). Slope stability and rockfall assessment of volcanic tuffs using RPAS with 2-D FEM slope modelling. *Natural Hazards and Earth System Sciences*, *18*(2), 583-597. https://doi.org/10.5194/nhess-18-583-2018

Ullman, S. (1979). Interpretation visual motion. *Massachusetts Inst of Technology Pr. Cambridge.*

United Nations Department of Economic and Social Affairs, P. D. (2022). World Population Prospects 2022 Summary of Results. Vol. UN DESA/POP/2022/TR/NO. 3. Available online: https://www.un.org/development/desa/pd/sites/www.un.org.development.desa.pd/files/wpp2022_summary_of_results.pdf

van Veen, M., Hutchinson, D. J., Kromer, R., Lato, M., & Edwards, T. (2017). Effects of sampling interval on the frequency-magnitude relationship of rockfalls detected from terrestrial laser scanning using semi-automated methods. *Landslides*, *14*(5), 1579-1592. https://doi.org/10.1007/s10346-017-0801-3

Vandewater, C. J., Dunne, W. M., Mauldon, M., Drumm, E. C., & Bateman, V. (2005). Classifying and assessing the geologic contribution to rockfall hazard. *Environmental & Engineering Geoscience*, *11*(2), 141-154. https://doi.org/10.2113/11.2.141

Varnes, D. J. (1978). Slope movement types and processes. *Special report*, *176*, 11-33.

Vollgger, S. A., & Cruden, A. R. (2016). Mapping folds and fractures in basement and cover rocks using UAV photogrammetry, Cape Liptrap and Cape Paterson, Victoria, Australia. *Journal of Structural Geology*, *85*, 168-187. http://dx.doi.org/10.1016/j.jsg.2016.02.012

Wang, W., Zhao, W., Chai, B., Du, J., Tang, L., & Yi, X. (2022). Discontinuity interpretation and identification of potential rockfalls for high-steep slopes based on UAV nap-of-the-object photogrammetry. *Computers & Geosciences*, *166*, 105191. https://doi.org/10.1016/j.cageo.2022.105191

Warrick, J. A., Ritchie, A. C., Schmidt, K. M., Reid, M. E., & Logan, J. (2019). Characterizing the catastrophic 2017 Mud Creek landslide, California, using repeat structure-from-motion (SfM) photogrammetry. *Landslides*, *16*(6), 1201-1219. https://doi.org/10.1007/s10346-019-01160-4

Watters, R. (1998). Modification to the Rockfall Hazard Rating System for successful mitigation in mountainous terrain as a result of climate and slope aspect considerations. *Association of Engineering Geologists 41st Annual Meeting, Programs with Abstracts*, 41, 134.

Weidner, L., & Walton, G. (2021). Monitoring the Effects of Slope Hazard Mitigation and Weather on Rockfall along a Colorado Highway Using Terrestrial Laser Scanning. *Remote Sensing*, *13*(22), 4584. https://doi.org/10.3390/rs13224584

Werner, C., Strozzi, T., Wiesmann, A., & Wegmuller, U. (2008). A real-aperture radar for ground-based differential interferometry. *Proceedings of the International Geoscience and Remote Sensing Symposium (IGARSS)*, 3, III210–III213. https://doi.org/10.1109/IGARSS.2008.4779320

Westoby, M., Lim, M., Hogg, M., Dunlop, L., Pound, M., Strzelecki, M., & Woodward, J. (2020). Decoding complex erosion responses for the mitigation of coastal rockfall hazards using repeat terrestrial lidar. *Remote Sensing*, *12*(16), 2620. https://doi.org/10.3390/rs12162620

Westoby, M. J., Brasington, J., Glasser, N. F., Hambrey, M. J., & Reynolds, J. M. (2012). 'Structure-from-Motion'photogrammetry: A low-cost, effective tool for geoscience applications. *Geomorphology*, *179*, 300-314. http://dx.doi.org/10.3390/rs11121443

Williams, J. G., Rosser, N. J., Hardy, R. J., & Brain, M. J. (2019). The importance of monitoring interval for rockfall magnitude-frequency estimation. *Journal of Geophysical Research: Earth Surface*, *124*(12), 2841-2853. https://doi.org/10.1029/2019JF005225

Wöhler, C. (2012). 3D Computer Vision: Efficient Methods and Applications. *Springer Verlag London Limited*.

Zhang, J., Boutin, M., & Aliaga, D. G. (2006). Robust bundle adjustment for structure from motion. *International Conference on Image Processing*, 2185–2188. http://dx.doi.org/10.1109/ICIP.2006.312973

Zhang, Q., Wang, J., Lin, P., & Hou, L. (2018). Application of an improved DPCA algorithm in rock-fall monitoring based on synthetic aperture radar. *Natural Hazards*, *94*(3), 1043-1055. https://link.springer.com/article/10.1007/s11069-018-3454-1

APPENDIX A ROCKFALL DATABASES

A.1 Site 1

Year	Volume (m^3)	Year	Volume (m^3)	Year	Volume (m^3)	Year	Volume (m^3)
14-15	2.9×10^{-2}	15-16	3.8×10^{-1}	17-21	1.7×10^{-1}	17-21	9.8×10^{-2}
14-15	8.7×10^{-2}	15-16	9.2×10^{-2}	17-21	9.9×10^{-2}	17-21	8.4×10^{-2}
15-16	9.2×10^{-2}	15-16	4.9×10^{-1}	17-21	1.1×10^{-1}	17-21	9.7×10^{-2}
15-16	5.3×10^{-2}	15-16	3.1	17-21	3.9×10^{-1}	17-21	5.7×10^{-1}
15-16	2.3×10^{-1}	15-16	4.1×10^{-2}	17-21	1.8	17-21	2.9
15-16	6.4×10^{-2}	15-16	1.1	17-21	2.2×10^{-1}	17-21	6.2×10^{-2}
15-16	2.5×10^{-1}	15-16	7.6×10^{-1}	17-21	7.8×10^{-2}	17-21	1.7×10^{-1}
15-16	6.0×10^{-2}	15-16	2.2×10^{-1}	17-21	6.1×10^{-1}	17-21	1.5×10^{-1}
15-16	3.2×10^{-2}	15-16	4.0×10^{-2}	17-21	1.4×10^{-1}	17-21	8.3×10^{-2}
15-16	4.1×10^{-2}	15-16	1.9×10^{-1}	17-21	5.1×10^{-2}	17-21	8.9×10^{-2}
15-16	2.9×10^{-2}	15-16	3.9×10^{-1}	17-21	1.3×10^{-2}	17-21	1.2×10^{-1}
15-16	5.0×10^{-2}	15-16	4.4×10^{-2}	17-21	2.0	17-21	2.9×10^{-1}
15-16	3.4×10^{-1}	16-17	1.8	17-21	1.8×10^{-2}	17-21	2.2×10^{-1}
15-16	1.3×10^{-1}	16-17	7.3×10^{-1}	17-21	1.2×10^{-1}	17-21	2.5×10^{-1}
15-16	7.3×10^{-2}	16-17	7.8	17-21	2.6×10^{-1}	17-21	2.5×10^{-2}
15-16	3.7×10^{-2}	16-17	2.9×10^{-2}	17-21	1.1×10^{-1}	17-21	1.1×10^{-2}
15-16	1.6×10^{-1}	16-17	3.4×10^{-2}	17-21	8.3×10^{-2}	17-21	5.6×10^{-1}
15-16	3.0×10^{-1}	16-17	1.5×10^{-1}	17-21	3.1×10^{-1}		
15-16	1.6×10^{-1}	16-17	1.2×10^{-1}	17-21	1.8×10^{-2}		
15-16	5.4×10^{-2}	16-17	1.0×10^{-1}	17-21	6.3×10^{-1}		
15-16	1.1×10^{-1}	16-17	3.2×10^{-2}	17-21	6.3×10^{-2}		
15-16	7.9×10^{-2}	16-17	9.5×10^{-2}	17-21	2.0×10^{-2}		
15-16	1.7	16-17	5.5×10^{-1}	17-21	1.0×10^{-1}		
15-16	3.5×10^{-1}	16-17	3.5×10^{-1}	17-21	3.6×10^{-2}		
15-16	1.1	16-17	1.8×10^{-1}	17-21	3.1×10^{-2}		
15-16	2.6	16-17	6.5×10^{-2}	17-21	3.7×10^{-1}		
15-16	2.0×10^{-1}	16-17	1.1×10^{-1}	17-21	3.3×10^{-1}		
15-16	8.1×10^{-2}	16-17	5.6×10^{-1}	17-21	6.8×10^{-2}		
15-16	3.1×10^{-1}	16-17	3.4×10^{-2}	17-21	1.3×10^{-1}		
15-16	2.5×10^{-1}	16-17	6.9×10^{-2}	17-21	1.3×10^{-1}		
15-16	3.4×10^{-2}	17-21	1.3×10^{-1}	17-21	2.6×10^{-1}		
15-16	9.7×10^{-2}	17-21	1.1×10^{-1}	17-21	5.5×10^{-1}		
15-16	4.2×10^{-1}	17-21	8.2×10^{-1}	17-21	3.5×10^{-1}		
15-16	5.0×10^{-1}	17-21	2.1	17-21	1.9×10^{-1}		

A.2 Site 2

Year	Volume (m^3)	Year	Volume (m^3)	Year	Volume (m^3)	Year	Volume (m^3)
14-15	4.1×10^{-1}	18-21	6.5×10^{-1}	18-21	1.4×10^{-2}	18-21	3.6×10^{-2}
15-16	5.2×10^{-2}	18-21	5.1×10^{-2}	18-21	6.9×10^{-2}	18-21	1.3×10^{-2}
15-16	8.8×10^{-2}	18-21	6.6×10^{-2}	18-21	3.5×10^{-1}	18-21	1.6×10^{-2}
15-16	4.4×10^{-1}	18-21	1.0×10^{-1}	18-21	3.5×10^{-2}	18-21	6.1×10^{-2}
15-16	1×10^{-3}	18-21	4.2×10^{-2}	18-21	1.3	18-21	2.0×10^{-2}
15-16	5.6×10^{-1}	18-21	3.2×10^{-1}	18-21	3.3×10^{-2}	18-21	4.0×10^{-2}
15-16	4.2×10^{-2}	18-21	2.5×10^{-2}	18-21	7.8×10^{-2}	18-21	7.9×10^{-2}
15-16	3.2×10^{-2}	18-21	3.7×10^{-2}	18-21	4.3	18-21	4.2×10^{-2}
15-16	1.3	18-21	1.8×10^{-1}	18-21	10.5	18-21	8.8×10^{-2}
15-16	4×10^{-4}	18-21	2.1×10^{-2}	18-21	7.8	18-21	7×10^{-3}
15-16	2.1×10^{-2}	18-21	5×10^{-3}	18-21	2.8×10^{-2}	18-21	1.2×10^{-2}
16-18	8×10^{-3}	18-21	3×10^{-3}	18-21	1.6	18-21	1.0×10^{-2}
16-18	3.4×10^{-2}	18-21	1.1×10^{-2}	18-21	3×10^{-3}	18-21	9×10^{-3}
16-18	2.2×10^{-1}	18-21	6.5×10^{-2}	18-21	1.6	18-21	8×10^{-3}
16-18	4.9×10^{-2}	18-21	3.4×10^{-2}	18-21	13.5	18-21	1.0×10^{-2}
16-18	6.5×10^{-2}	18-21	4.1×10^{-2}	18-21	1.5	18-21	1.5×10^{-2}
16-18	1.4×10^{-1}	18-21	2.5×10^{-1}	18-21	6.3×10^{-2}	18-21	1.8×10^{-2}
16-18	2.4×10^{-2}	18-21	4.1×10^{-2}	18-21	3.0×10^{-1}	18-21	8×10^{-3}
16-18	3.1×10^{-2}	18-21	1.3	18-21	2.1×10^{-1}	18-21	2.1×10^{-2}
16-18	5×10^{-3}	18-21	5×10^{-3}	18-21	1.5	18-21	10×10^{-3}
16-18	5.9×10^{-2}	18-21	1.4×10^{-2}	18-21	3.0×10^{-2}	18-21	1.7×10^{-2}
16-18	2.6×10^{-1}	18-21	2.4×10^{-2}	18-21	2.5×10^{-2}	18-21	1.3×10^{-1}
16-18	6.7×10^{-2}	18-21	9.6×10^{-2}	18-21	5.9×10^{-2}	18-21	5×10^{-3}
16-18	2.1×10^{-2}	18-21	1.9×10^{-2}	18-21	6.8×10^{-1}	18-21	9×10^{-3}
18-21	6.4×10^{-2}	18-21	1.4×10^{-2}	18-21	4.0×10^{-2}		
18-21	2.3×10^{-2}	18-21	1.6×10^{-2}	18-21	1.1×10^{-2}		
18-21	1.1×10^{-1}	18-21	1.3×10^{-2}	18-21	3.5×10^{-2}		
18-21	6×10^{-3}	18-21	9.5×10^{-2}	18-21	6×10^{-3}		
18-21	2.9×10^{-1}	18-21	5.4×10^{-2}	18-21	3.1×10^{-2}		
18-21	9.7×10^{-1}	18-21	5.2×10^{-2}	18-21	2.3×10^{-2}		
18-21	1.1	18-21	1.1×10^{-2}	18-21	5×10^{-3}		
18-21	7.2×10^{-1}	18-21	3.2×10^{-2}	18-21	2.6×10^{-2}		
18-21	1.6×10^{-1}	18-21	1.2	18-21	3.7×10^{-2}		
18-21	3.1×10^{-1}	18-21	7×10^{-3}	18-21	5.7×10^{-2}		

A.3 Site 3

Year	Volume (m^3)	Year	Volume (m^3)	Year	Volume (m^3)	Year	Volume (m^3)
14-15	2.4×10^{-2}	15-16	5.7	16-17	1.0×10^{-1}	18-21	1.6×10^{-1}
14-15	1.1×10^{-2}	15-16	2.6	16-17	3.9×10^{-2}	18-21	6.7×10^{-2}
14-15	2.4×10^{-2}	15-16	9.6×10^{-2}	16-17	5.5×10^{-1}	18-21	1.0×10^{-2}
14-15	1.6×10^{-1}	15-16	3.7	16-17	1.0×10^{-2}	18-21	4×10^{-3}
14-15	8.6×10^{-1}	15-16	1.9×10^{-2}	16-17	2×10^{-3}	18-21	3×10^{-3}
15-16	2×10^{-3}	15-16	7.6×10^{-2}	16-17	1.8×10^{-2}	18-21	7.8×10^{-2}
15-16	2.6×10^{-1}	15-16	8.9×10^{-2}	16-17	3.5×10^{-2}	18-21	9.4×10^{-2}
15-16	7×10^{-3}	15-16	1.7×10^{-2}	16-17	2.8×10^{-1}	18-21	2.4×10^{-2}
15-16	5×10^{-4}	15-16	5.3×10^{-2}	16-17	2.7×10^{-1}	18-21	4×10^{-3}
15-16	1.7×10^{-2}	15-16	2.2×10^{-2}	16-17	3.2×10^{-1}	18-21	4.2×10^{-1}
15-16	1.2×10^{-1}	15-16	3×10^{-3}	16-17	1.7×10^{-2}	18-21	6.1×10^{-2}
15-16	1.8×10^{-2}	15-16	8×10^{-3}	17-18	8×10^{-3}	18-21	5.3×10^{-2}
15-16	4.8×10^{-2}	15-16	1.1×10^{-1}	17-18	1.4×10^{-2}	18-21	1.8×10^{-1}
15-16	2×10^{-3}	15-16	3×10^{-3}	17-18	6×10^{-3}	18-21	3×10^{-3}
15-16	2.4×10^{-1}	15-16	2×10^{-3}	17-18	4.8×10^{-1}	18-21	1.4×10^{-2}
15-16	1.9×10^{-1}	15-16	2×10^{-3}	17-18	1.4×10^{-1}	18-21	1.4×10^{-2}
15-16	3.0×10^{-1}	15-16	1×10^{-3}	17-18	3×10^{-3}	18-21	2.8×10^{-1}
15-16	2.8×10^{-2}	15-16	2×10^{-3}	17-18	2.4×10^{-2}	18-21	4.5×10^{-2}
15-16	5×10^{-3}	15-16	5×10^{-4}	17-18	7.4×10^{-1}	18-21	5.8×10^{-2}
15-16	6×10^{-3}	16-17	6.8×10^{-1}	17-18	3.3×10^{-1}	18-21	1.0×10^{-2}
15-16	1.5×10^{-2}	16-17	4×10^{-4}	17-18	8.5×10^{-2}	18-21	6×10^{-3}
15-16	2.1×10^{-2}	16-17	3×10^{-3}	17-18	4.4	18-21	2.1×10^{-2}
15-16	6.3×10^{-2}	16-17	1.7×10^{-2}	17-18	1.0×10^{-1}	18-21	3×10^{-3}
15-16	3.0×10^{-2}	16-17	2×10^{-3}	17-18	1.5×10^{-1}	18-21	8×10^{-3}
15-16	4.1×10^{-2}	16-17	2×10^{-3}	17-18	4.5×10^{-2}	18-21	5×10^{-3}
15-16	5.6×10^{-2}	16-17	1.1×10^{-2}	18-21	4.3×10^{-1}	18-21	9.2×10^{-2}
15-16	1.1×10^{-2}	16-17	1.6×10^{-2}	18-21	4×10^{-3}	18-21	2.5×10^{-2}
15-16	4×10^{-3}	16-17	1.6×10^{-1}	18-21	1.0×10^{-2}	18-21	3.4×10^{-2}
15-16	1.7×10^{-2}	16-17	5×10^{-3}	18-21	8.7×10^{-2}	18-21	1.0×10^{-1}
15-16	2.1×10^{-1}	16-17	7×10^{-3}	18-21	2×10^{-3}	18-21	8×10^{-3}
15-16	5.3×10^{-2}	16-17	3.7×10^{-2}	18-21	1.7×10^{-2}	18-21	1.7×10^{-2}
15-16	1.1	16-17	4.9×10^{-2}	18-21	8.0×10^{-2}	18-21	1.1×10^{-1}
15-16	2.1×10^{-1}	16-17	3.0	18-21	1.3	18-21	6.0×10^{-2}
15-16	2.0×10^{-1}	16-17	2.9×10^{-1}	18-21	6×10^{-3}	18-21	1.0×10^{-2}

Year	Volume (m^3)		Year	Volume (m^3)		Year	Volume (m^3)
18-21	2×10^{-3}		18-21	4.3×10^{-1}		18-21	3.7×10^{-1}
18-21	7×10^{-3}		18-21	3.4×10^{-2}		18-21	4.5×10^{-2}
18-21	2.0×10^{-1}		18-21	6.4×10^{-1}		18-21	1.4×10^{-1}
18-21	6×10^{-3}		18-21	1.1×10^{-1}		18-21	4×10^{-4}
18-21	1.1×10^{-2}		18-21	2.3		18-21	1.2×10^{-2}
18-21	2.3×10^{-2}		18-21	2.8×10^{-1}		18-21	2.2×10^{-1}
18-21	5.0×10^{-2}		18-21	1.0×10^{-1}			
18-21	7×10^{-3}		18-21	16.1			
18-21	2.8×10^{-2}		18-21	6.6×10^{-2}			
18-21	3.8×10^{-2}		18-21	1.6			
18-21	1.2×10^{-1}		18-21	2.8×10^{-1}			
18-21	6×10^{-3}		18-21	1.5×10^{-1}			
18-21	1.8×10^{-2}		18-21	5.6×10^{-1}			
18-21	8.4×10^{-2}		18-21	2.4 x 10-2			
18-21	7×10^{-3}		18-21	4.1×10^{-2}			
18-21	8.3×10^{-2}		18-21	4.4×10^{-2}			
18-21	1.2×10^{-2}		18-21	1.2×10^{-1}			
18-21	8.7×10^{-2}		18-21	7.9×10^{-1}			
18-21	2.7×10^{-1}		18-21	3.7×10^{-2}			
18-21	4×10^{-3}		18-21	5.3×10^{-2}			
18-21	5.8×10^{-1}		18-21	4.4×10^{-2}			
18-21	3.9×10^{-2}		18-21	1.1×10^{-2}			
18-21	8×10^{-3}		18-21	5.4×10^{-2}			
18-21	1.1×10^{-1}		18-21	1.0×10^{-1}			
18-21	23.1		18-21	9.0×10^{-2}			
18-21	1.7×10^{-1}		18-21	1.3×10^{-1}			
18-21	6×10^{-3}		18-21	6.8×10^{-2}			
18-21	4.3×10^{-2}		18-21	1.8×10^{-2}			
18-21	1.2×10^{-1}		18-21	2.6×10^{-2}			
18-21	1.5×10^{-1}		18-21	3.8×10^{-1}			
18-21	9.3×10^{-2}		18-21	3.2×10^{-1}			
18-21	4.6×10^{-1}		18-21	9×10^{-3}			
18-21	5.7×10^{-1}		18-21	6×10^{-3}			
18-21	2.9×10^{-1}		18-21	2.8×10^{-1}			